

# The gravitational capture of compact objects by massive black holes

Pau Amaro Seoane \*

**Abstract** The gravitational capture of a stellar-mass compact object (CO) by a supermassive black hole is a unique probe of gravity in the strong field regime. Because of the large mass ratio, we call these sources extreme-mass ratio inspirals (EMRIs). In a similar manner, COs can be captured by intermediate-mass black holes in globular clusters or dwarf galaxies. The mass ratio in this case is lower, and hence we refer to the system as an intermediate-mass ratio inspiral (IMRI). Also, sub-stellar objects such as a brown dwarf, with masses much lighter than our Sun, can inspiral into supermassive black holes such as Sgr A\* at our Galactic centre. In this case, the mass ratio is extremely large and, hence, we call this system ab extremely-large mass ratio inspirals (XMRI). All of these sources of gravitational waves will provide us with a collection of snapshots of spacetime around a supermassive black hole that will allow us to do a direct mapping of warped spacetime around the supermassive black hole, a live cartography of gravity in this extreme gravity regime. E/I/XMRIs will be detected by the future space-borne observatories like LISA. There has not been any other probe conceived, planned or even thought of ever that can do the science that we can do with these inspirals. We will discuss them from a viewpoint of relativistic astrophysics.

---

Pau Amaro Seoane  
Universitat Politècnica de València, IGIC, Spain  
DESY Zeuthen, Germany  
Kavli Institute for Astronomy and Astrophysics, Beijing, China  
Institute of Applied Mathematics, Academy of Mathematics and Systems Science, CAS, Beijing, China  
Zentrum für Astronomie und Astrophysik, TU Berlin, Berlin, Germany  
e-mail: [amaro@upv.es](mailto:amaro@upv.es)

\* PAS acknowledges support from the Ramón y Cajal Programme of the Ministry of Economy, Industry and Competitiveness of Spain, as well as the COST Action GWverse CA16104. This work was supported by the National Key R&D Program of China (2016YFA0400702) and the National Science Foundation of China (11721303). He is indebted with Marta Masini for her support during the lockdown, without which this work would not have been possible.

## Keywords

gravitational captures, supermassive black holes, stellar dynamics, LISA, tests of general relativity

## Introduction - Why is this important?

For many years we have known that at the centre of most nearby bright galaxies a very massive, compact and dark object must be lurking [e.g., 108, 76, 109]. Recently, the Event Horizon Telescope finally delivered the result that we were expecting; the “shadow” of one of these dark objects at the centre of the galaxy M87, with a mass of  $6.5 \times 10^7 M_\odot$  [68]. In Fig. (1) we show their result with the position of Voyager1 and Pluto if our Sun was located at the centre of the image. This is exceptionally *to scale*, Note though, as the author of the comic told us, that the blurring makes the dark shadow look smaller than it is. But the diameter of the brightest part of the ring should be  $\sim 640$  AU.

In 2020, the Nobel prize went to Roger Penrose, Reinhard Genzel and Andrea Ghez. The two latter have devoted a significant part of their careers to study an interesting phenomenon happening at our own Galactic Centre: A cluster of young stars revolving around a point of small size, a radio source, on observable timescales. After analysing the orbits, Genzel’s and Ghez’ groups came to the conclusion that these stars, which are called the S- or SO-stars, are orbiting a point mass of about  $4 \times 10^6 M_\odot$  enclosed in a volume as small as 1/3 the distance between the Earth and the Sun. We call this “point” mass Sgr A\* (see for a review Genzel et al. 76, and references therein). The properties of these stars are interesting. For instance, S4714 moves at about 8% the speed of light, and S62 is as close as 16 AU from SgrA\* [140]. The team of Genzel presented this year the detection of the Schwarzschild precession in the orbit of S2 after its second periapsis passage. According to their measurements, the predictions of general relativity (GR) and the observations are in agreement by 17% [87].

Therefore, even if we still cannot yet completely exclude other exotic possibilities that nature might have come up with, it looks like SgrA\* and the dark object located at the centre of M87 are supermassive black holes, and this is what we will assume in this chapter. In that case, the Event Horizon Telescope has measured the event horizon to be of about 0.0013 pc [68]. We will however have a stronger evidence when we detect the gravitational waves (GWs) from a system involving a supermassive black hole (SMBH), in particular an E/I/XMRI.

In this chapter we focus on this particular source of GWs. In the literature, the most studied inspiral has so far been the gravitational capture of a stellar-mass compact object (i.e. a stellar-mass black hole, a neutron star or a white dwarf) by a SMBH. Because in their orbits and in a matter of a few years, these sources significantly shrink their semi-major axes, precess and if the SMBH is Kerr (and that is the most likely situation in nature, see e.g. [161]), the plane of the orbit changes, so

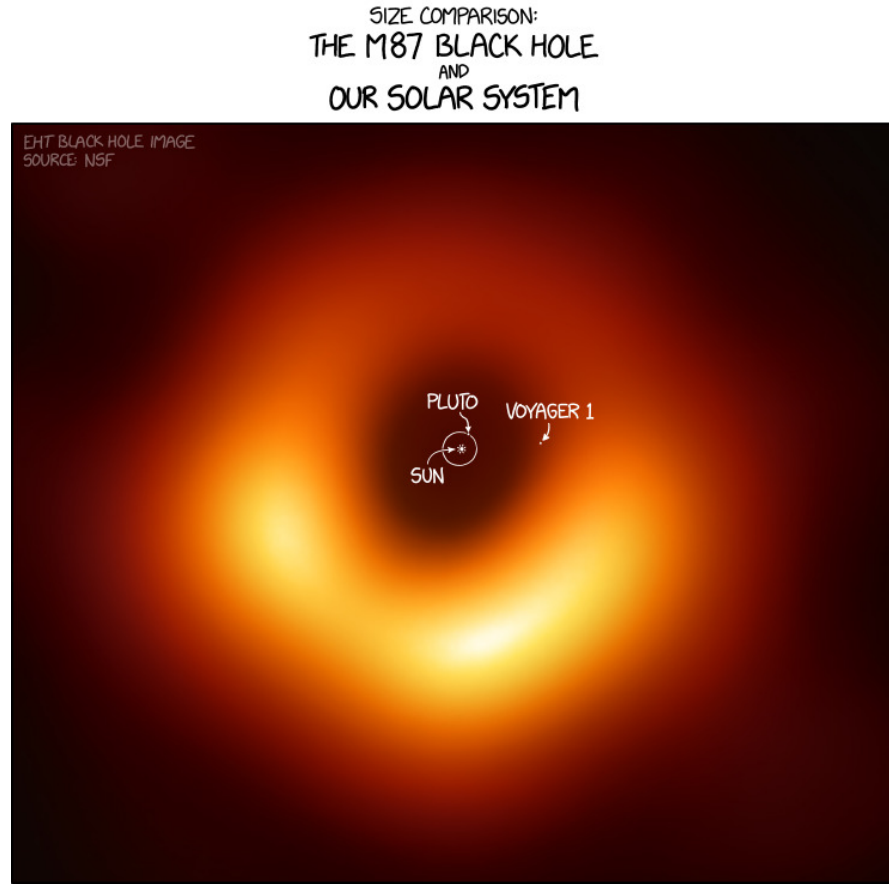


**Fig. 1** The shadow of the dark object found in M87. From <https://xkcd.com/2135/> and with the XKCD team authorization, using the original figure from the EHT team web page, <https://eventhorizontelescope.org/>

that they map spacetime around SMBHs. The number of cycles that they describe around the SMBH is inversely proportional to the mass ratio, so that an EMRI will provide us with a collection of about  $\sim 10^5$  snapshots of spacetime around a SMBH. This translates literally into a cartography of warped spacetime in the strong regime of gravity. In this sense, these sources of GWs are unique.

The ideal instrument to look for this kind of inspirals is the ESA/NASA mission The Laser Interferometer Space Antenna [LISA, see 17], because the total mass is too large for ground-based detectors (with the exception of some particular cases of IMRIs, as we will discuss). LISA consists of three spacecraft arranged in an equilateral triangle of  $2.5 \times 10^6$  km armlength flying on a heliocentric orbit, with a strain sensitivity of less than 1 part in  $10^{20}$  in frequencies of about a millihertz.

Most of this chapter will be devoted to addressing the question of how do you form these sources. We will see that not all phase-space is at our disposition to create one of these inspirals, and that the conditions change a lot depending on whether it is an EMRI, an IMRI or an XMRI.

### *Fundamental science*

EMRIs, IMRIs and, within some limitations, XMRIs are probes of fundamental physics with GWs, mostly due to the fact that these inspirals spend a large number of cycles very close at the verge of the the last stable orbit, where precessional are the strongest [see e.g. 24, 36].

An EMRI has three fundamental frequencies associated to it [14, 16] which are encoded in the gravitational wave emitted by the system. The associated timescales depend on the Kerr geometry and will evolve due to gravitational backreaction, which can evolve in very different ways depending on the type of gravity one considers, or whether there are extra dimensions or fields. In this sense, the detection and extraction of this information can be used as a tool to explore these new ideas, or might turn into something that we had not previously considered or even thought of.

Because we want to extract information from the modelling of a source that will last months to years, the waveforms ab definitio must be very precise and therefore subject to important (accumulated) deviations if what we are measuring does not correspond to the general relativity picture. In some sense, this might be regarded as a double-edged sword. On the one hand we can extract very accurately gravitational multipole moments describing the SMBH geometry, as well as other parameters that provide us with information about modifications of GR, such as coupling constants and extra dimension length scales. On the other hand, if such modifications are there and are important, we might lose the source altogether. Therefore, we can in principle use EMRIs as they generate GWs [31] as tools to explore the nature and geometry of SMBHs, i.e. the no-hair conjecture[see e.g. 14, 16], complementary in a sense with the detection of quasinormal models excited in the ringdown of a SMBH binary merger [37], and rule out exotic objects such as e.g. boson stars [15, 91]. This is particularly true for multi-bandwidth detections, i.e. IMRIs, which can be detected in the early inspiraling phase by LISA and later by ground-based detectors [6, 62], because the combined detection would help to break up different degeneracies in the parameter extraction.

EMRI GWs are subject to be affected by additional mechanisms that might alter them on their way towards us, such as extra polarizations, gravitational parity violation, breaking of Lorentz invariance, all of them related to high-energy effects [see 33]. There are also other potential effect that could importantly modify the waves, such as the aberrational- and beaming effects, and their combination [174, 175], which emerge when the source is moving relative to us.

In a more speculative manner, we could also use E/IMRIs to explore the possibility that primordial black holes do exist [47], assuming that we have confidence in our astrophysical modelling of what the mass of the CO is, which might not necessarily be true. This connects to the idea that dark matter could be constituted of such primordial black holes [see the review of 46]

For astrophysics, these sources of GWs are important because we can try to reverse-engineer the information that they will provide us with to probe regions of the galaxy which are inaccessible to light because of obscuration or distance.

## Extreme-mass ratio inspirals

### *A long story short*

The problem of how a CO could become an EMRI in a galactic nucleus is, as of writing these lines, a problem which goes back in time three decades to the best of our knowledge [162, 99, 90, 159]. The first reference uses the fundamentals of the theory of loss-cone in the context of relaxation to derive the rates and characteristics. It is natural that this first attempt happened at that time and place, because the study of stellar disruptions was one of the main interests of the second author of the paper. However, as compared to a tidal disruption, the slow, progressive inspiral of a CO is a more challenging problem, as we will see.

We will adopt the Milky Way as a typical, reference galaxy host to the kind of sources that we are going to address in this chapter. The mass of the central SMBH will have that of SgrA\*,  $4 \times 10^6 M_\odot$ , or of the order of it. The fiducial CO we will consider is a stellar-mass black hole of mass  $m_{\text{BH}} = 10 M_\odot$  for historical reasons: This was the default assumed mass before the first discoveries of LIGO/Virgo, since we cannot explain how to form stellar-mass black holes with larger masses via (reasonable) stellar evolution.

In this chapter we are going to focus in detail on the most well-understood mechanism (in the sense that the number of free parameters is very small), which is relaxation, more specifically two-body relaxation. Other mechanisms have been proposed, in particular the so-called “resonant relaxation” [150], which seemed very important a few years ago. Another interesting scenario has been proposed, which involves the tidal separation of a binary in which one of the stars is a CO. This possibility is an interesting one, but we are missing a fundamental piece of information, which is the distribution of initial semi-major axes and eccentricities, as well as the fraction of such binaries harbouring a CO. Nonetheless, since the mechanism is simple and robust enough, we will also address it in some detail.

To summarise in a few paragraphs what has been the work of decades, the study of EMRI event rate was addressed in the framework of two-body relaxation, since the problem shared similarities to the tidal disruption of a star. The event rate for a typical galaxy (i.e. a Milky-Way-like galaxy, as stated before) is very low, of the

order of  $10^{-5} - 10^{-6} \text{ yr}^{-1}$  [see e.g. 18, and references therein]. Because of the dynamical properties that the COs have when they form a potential EMRI source with the central SMBH, i.e. have very large eccentricities and semi-major axis of about  $0.1 - 1 \text{ pc}$ , at apocentre they risk being scattered off the EMRI orbit via the accumulation of gravitational tugs from other stars (we will elaborate this later). If we perturb the apocentre, the pericentre is also perturbed and the fate of the potential EMRI is twofold: It can either increase more and more the initial eccentricity to the point that it forms almost a straight line which leads it to a directly cross the event horizon of the SMBH or it can simply be reabsorbed by the stellar system. In the first case, it would produce one burst of gravitational radiation and then be lost in terms of GWs [35, 102]. It is important to note here that such orbits have unfortunately been dubbed in the (astrophysical) literature as “plunges” or “direct plunges”, which leads to confusion and should be avoided, since any EMRI will eventually cross the event horizon of the SMBH. This is referred to in other texts as the plunge of the orbit. We will only use the term “plunge” in the sense that the CO crosses the event horizon of the SMBH. In the second, it would never emit (detectable) GWs. A better term would be a “1-burst orbit”, because the system emits one intense burst of GWs and then it is lost. We note there are scenarios in which we can have repeated bursts coming parabolic orbits, not bound ones, and the rate is of about one burst per observation year [see references in 8]. We are not referring to these here.

The fact is that the assumptions under the classification of orbits which led to consider 1-burst orbits have been highly simplified in the literature. In reality, both for Schwarzschild and Kerr SMBHs, 1-burst orbits are extremely difficult to achieve. The work of [13] illustrates this with an example. The authors take a SMBH with no spin, Schwarzschild, and analyse orbits for a stellar-mass black hole with such an eccentricity that would lead to a 1-burst scenarios.

The authors then calculate the number of periapsis passages before it plunges through the event horizon. From the initial semi-latus rectum, eccentricity and inclination  $p, e, \iota$ , they calculate the constants of motion  $E, L_z, C$  (energy, z-component of the angular momentum and Carter’s constant), the average flux of these “constants”, i.e. the average time evolution,  $\dot{E}, \dot{L}_z$ , and  $\dot{C}$ . This allows them to calculate the time to go from apoapsis and back (radial period), and thus the change in  $E, L_z, C$  and so the new constants of motion,  $p_{\text{new}}, e_{\text{new}}, \iota_{\text{new}}$ . The authors find that the family of separatrices in the Kerr case deviate from the Schwarzschild case depending on (1) the spin of the SMBH, (2) the inclination of the orbit and (3) whether the orbit is pro- or retrograde.

For prograde orbits, the last stable orbit (LSO) is closer to the event horizon and, hence, the possibility that the CO is on a 1-burst orbit becomes more rare. Retrograde orbits, on the contrary, have LSOs farther away than in the Schwarzschild case. Therefore, it is easier to find 1-burst situations. Nevertheless, the situation is not symmetric. The farthest possible away separatrix for a retrograde orbit is much closer to the Schwarzschild separatrix than the equivalent for a prograde orbit. In Fig. (2), which is using the same method as in [13], we can see this. The green separatrices for retrograde orbits are closer to the Schwarzschild case than the blue ones, which correspond to prograde orbits.

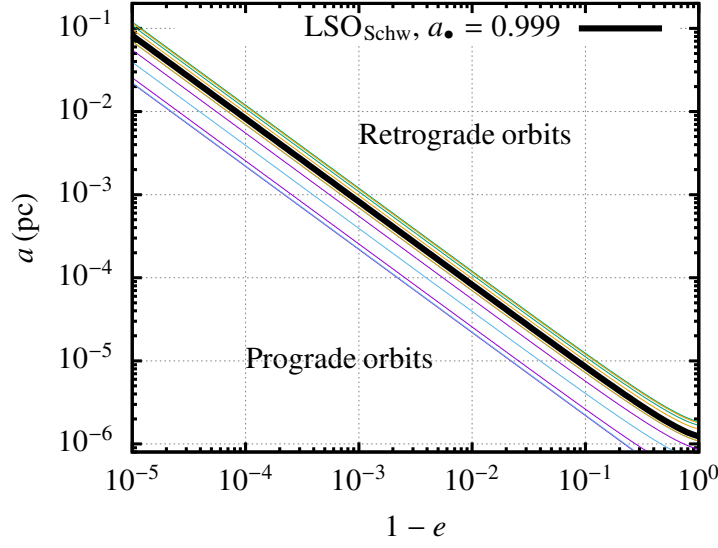


**Fig. 2** Different separatrices for a Kerr SMBH of  $a_* = 0.999$ . The separatrices which correspond to retrograde orbits are shown above the Schwarzschild LSO (black, thick line) and prograde below it.

The work of [13] shows that the number of cycles in the band of the detector before plunging through the event horizon is as large as  $10^5$  for some prograde cases, and at least of a few hundreds, depending on the spin and inclination. Retrograde cases, however, can lead more easily to 1-burst orbits. However, due to the asymmetry, these are much more rare.

It must be stressed out that, *even in the Schwarzschild case, it is difficult to have 1-burst orbits*. This is so because the energy radiated away at periaapsis is proportional to  $q$ , so that even for orbits with very small periaapsis distances the EMRI in general cannot radiate away the required amount of energy for the CO to plunge.

There are exceptions to this situations which, however, are fine-tuned, such as the zoom-whirl orbits [85]. In this case, even if we only have one radial oscillation, there is an arbitrary number of (different) oscillations along the azimuthal axis, which translate into a very strong precession of the orbit.

When a Keplerian orbit extends beyond the potential well in radius, the orbits are non-closed anymore [the Newtonian precession, see e.g. 8]. Such non-closed orbits have a periaapsis advance as a consequence. There are two periods in these orbits, the orbital period, is the required time to go from apo- to periaapsis and another one is the time to revolve  $2\pi$  in the orbit. These two periods are identical in the Keplerian case of closed orbits. In the relativistic case these two periods always differ, and the more relativistic, the larger the difference, to the point of being arbitrarily different. This leads to a precession of the orbit with an arbitrary number of cycles in a single radial period, if the initial conditions are matched. This means that one needs a high degree of fine tuning in the Hamiltonian system which describes the initial



dynamical parameters. In such a case, the amount of energy radiated is considerable and it could lead to the CO to indeed plunge through the event horizon after one single periapsis passage.

In the Kerr case the physical picture is even more complex, depending on whether the orbit is pro- or retrograde. If it is prograde, since the orbit gets closer to the LSO, it will induce a stronger precession of the orbit than in the Schwarzschild case. If it is retrograde, the number of cycles will be less than in the Schwarzschild case.

Another possibility would be that the SMBH is Kerr and the orbit of the CO is perfectly parallel and aligned with the axis of the spin of the SMBH. In that case, from the perspective of the CO, the SMBH would be de facto a Schwarzschild SMBH and this peculiar situation could have a 1-burst orbit.

These are nonetheless very peculiar configurations and tuning of the initial conditions of the orbits, so that the probability for these scenarios to happen frequently in the formation of EMRIs is low.

The belief that most sources would be lost to 1-burst orbits led a number of researchers to look at alternative scenarios, in particular to resonant relaxation. The idea was that by getting closer and closer to the SMBH, the number density of stars would decrease and, hence, the danger of turning a successful EMRI orbit into a 1-burst orbit would decrease. But, at the same time, because of the drop of density, the timescale associated to relaxation would increase more and more, so that the event rate would drastically drop. This is why the concept of (scalar) resonant relaxation as presented by [151] was envisaged as a possible way to enhance the rate.

This motivation led to interesting discoveries in the field of theoretical stellar dynamics (see in particular the work of [101, 66, 28, 168, 29]). However, even in the range of radii in which scalar resonant relaxation was thought to be a promising driver of EMRIs, it is now well settled that in the end two-body relaxation is the main mechanism. Therefore, in this work we will focus on two-body relaxation and loss-cone theory. For more details about resonant and scalar relaxation, and alternative scenarios, we refer the reader to the review [18].

## *Stellar tidal disruptions*

The theory on which we address the problem of formation and evolution of EMRIs is two-body relaxation [see e.g. 39, 164] in the context of stellar tidal disruptions (for a recent review of the theory and derivation of the rates, and references therein [169], and for some classical references, see [152, 128, 170, 178]).

When an extended star (meaning a star which is not a CO), such as our Sun, approaches “too closely” a SMBH, it will suffer a difference of gravitational forces on points diametrically separated on its structure due to the fact that it is not a point particle. Hence, depending on how close the star, typically on a hyperbolic orbit, gets to the SMBH, it will get disrupted or not, since we have to compare the work exerted over it by the tidal force with its own binding energy. The radius within which this happens is what we call the tidal radius  $r_t$ , and can be derived to be [see



e.g. Sec. 1.3 of [7], but note the small typo, the factor 2 should be outside of the brackets]

$$r_t = \left[ \frac{(5-n)}{3} \frac{M_{\text{BH}}}{m} \right]^{1/3} 2r, \quad (1)$$

with  $r$  the radius of the star,  $m$  its mass,  $M_{\text{BH}}$  the mass of the SMBH and  $n$  the polytropic index. For our Sun, considering a  $n = 3$  polytrope, and  $M_{\text{BH}} = 10^6 M_\odot$ ,

$$r_t \simeq 1.83 \times 10^{-6} \text{ pc} \simeq 0.38 \text{ AU}. \quad (2)$$

We show in Figure 3 a smoothed-particle hydrodynamics simulation of the tidal disruption of a star of mass  $m = 1 M_\odot$ , which corresponds to Fig. 2 of [7]. We can see that the star adopts a spheroidal shape after it has passed through periapsis on its orbit around a SMBH of mass  $10^6 M_\odot$ . The top, left panel corresponds to the initial time, and the rest of the panels to later moments.

As we can see in Figs. (3) and (4), the Sun will be able to only describe a close passage around the SMBH to then be tidally torn apart (if the trajectory crosses the tidal radius, and the disruption degree depends on how deep the passage is).

Contrary to extended stars, COs can revolve around the SMBH many times, as we have already mentioned. This is so because the tidal radius of a neutron star (NS) is located within the event horizon of the SMBH, so that we will never see the NS being disrupted. An interesting situation, however, are systems composed of an IMBH and a white dwarf (WD), because the WD will be tidally disrupted before plunging through the event horizon [see e.g. 131, 160, 153, 129].

In Fig. (5), we show the relation between the mass of a SMBH and the mass of a star, or sub-stellar object, for it to cross the event horizon without being tidally disrupted. For instance, we can see that a red giant with a mass of  $50 M_\odot$  can plunge directly the event horizon of a SMBH of mass  $\gtrsim 4 \times 10^8 M_\odot$  without being disrupted. For this figure we have taken into account the mass-radius relations from the modelling of stars of [156, 132, 51, 48]. These relations reproduce almost identically the more recent data of [49] for brown-dwarfs.

The problem of an EMRI is conceptually very similar to that of a tidal disruption. However, instead of one periapsis passage, the source will pass through periapsis tens to hundreds of thousand of times. EMRIs form initially with very high eccentricities, as we will see, so that the apocentre can extend well into the bulk of the stellar system. A perturbation at apocentre can lead to (i) the EMRI scattering off the orbit, so that we lose the source of GWs or to (ii) increase even more its eccentricity.

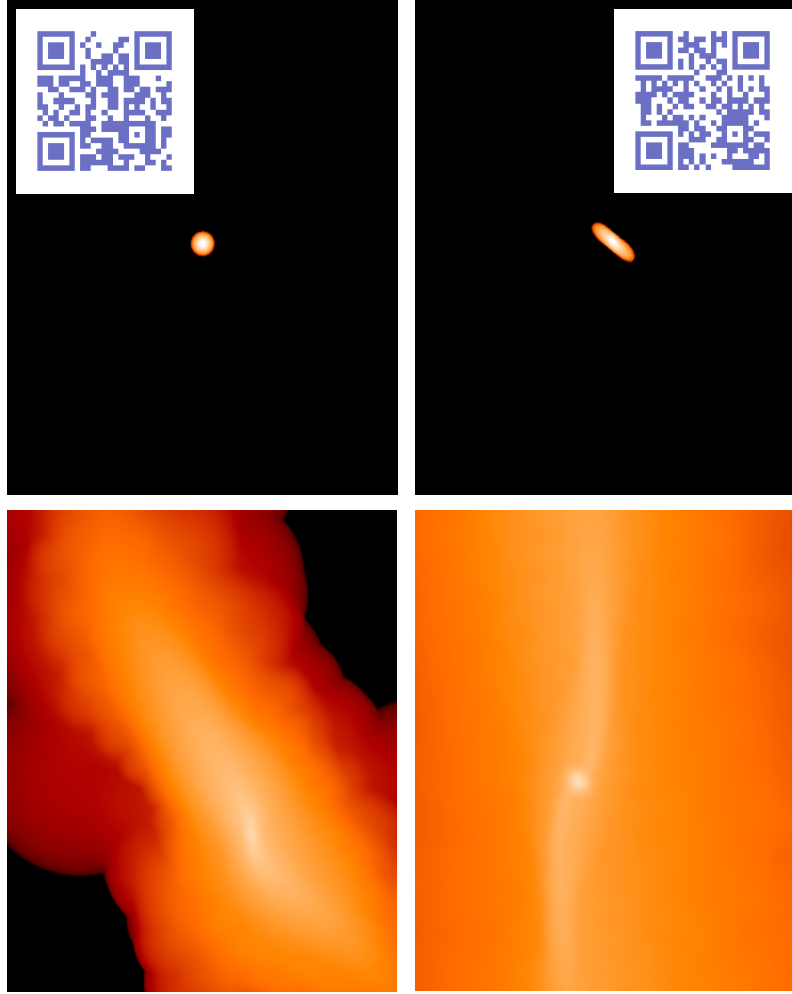


**Fig. 3** Tidal disruption of a sun-like star around a SMBH of mass  $M_{\text{BH}} = 10^6 M_{\odot}$ , on the frame of the star. The QRC link to the URLs <https://youtu.be/Ryc44v4Eb7I> and <https://youtu.be/uZqXBD8R9Dw>. This is Fig. (2) of [8], distributed under the terms of the Creative Commons Attribution 4.0 International License (<http://creativecommons.org/licenses/by/4.0/>).

### *Relaxation theory*

In Newtonian physics we cannot analytically solve systems with more than two bodies (but for very special configurations, in which there is an additional body which has a much smaller mass than the two other bodies, which is the restricted three-body problem). However, when we try to understand the formation of EMRIs, IMRIs or XMRIs, we need to look at dense stellar systems which might have up to

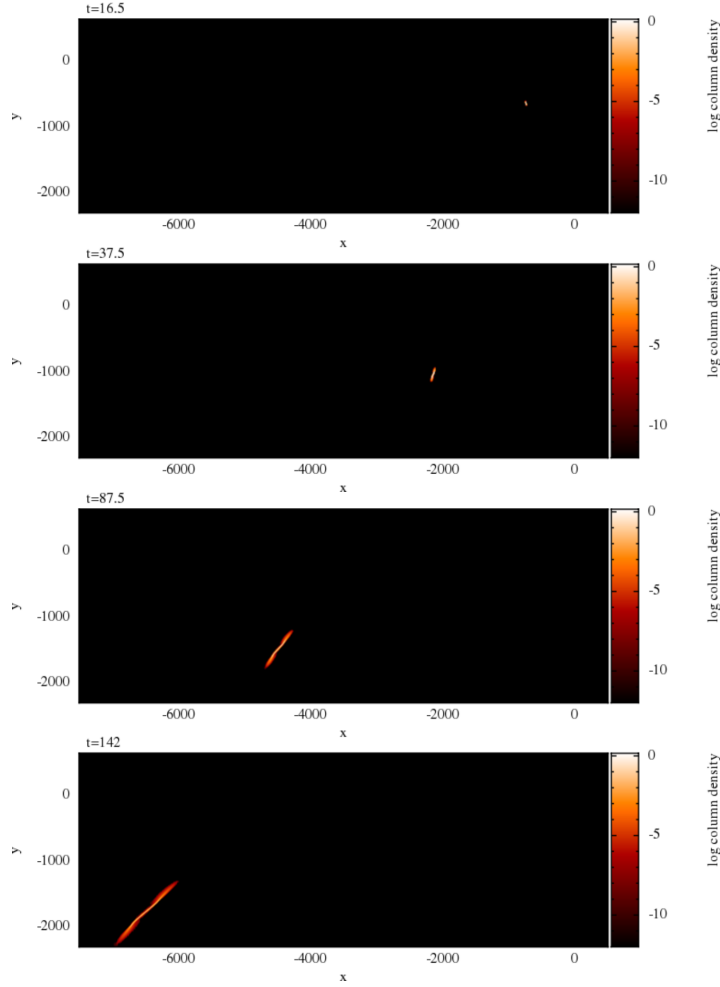


**Fig. 4** Same as Fig. (3) but in the general frame. The SMBH is located at the origin of coordinates. We have selected four snapshots right after the periastris passage. The length is expressed in solar radii. We can see how the star is torn apart and extends to much longer radii than the initial radius of the star,  $m = 1 M_{\odot}$ .

$10^8 M_{\odot} \text{pc}^{-3}$ . These densities are orders of magnitude above what we find around our solar system, which typically has of the order  $10^{-2} M_{\odot} \text{pc}^{-3}$ .

Since we cannot solve this problem, we try to address it by borrowing ideas from other fields in physics, such as plasma physics, because it also shares the property of inverse square laws. However, plasmas are often nearly uniform, rest and large spatial extent, which is not the case of a dense stellar system. Another possibility is thermodynamics because, in some sense, we can think of a dense stellar system as a gaseous medium. Nonetheless, thermodynamics excludes a description of

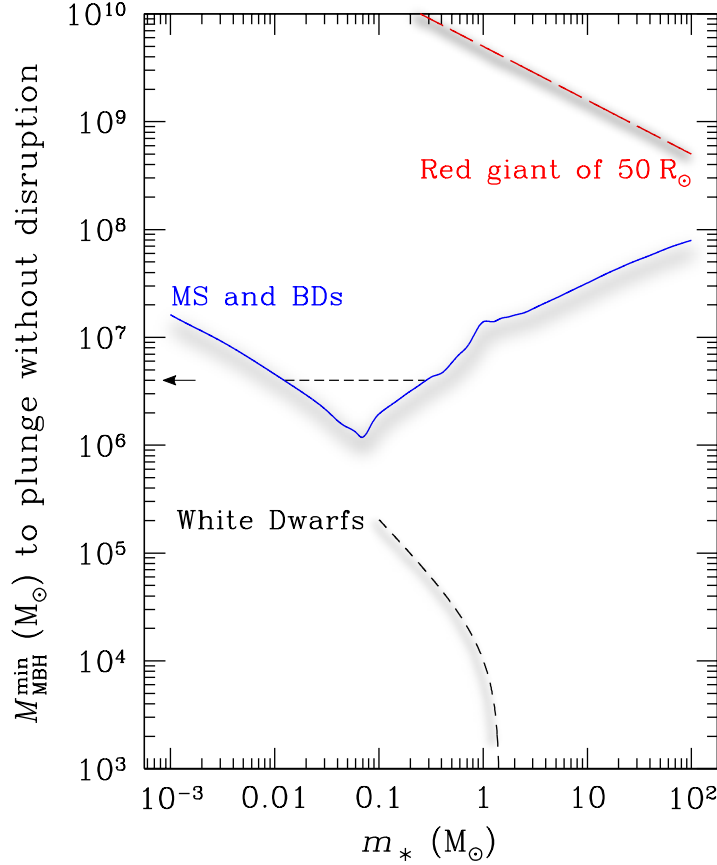


**Fig. 5** Adapted figure Fig. 1 from [19]. Minimum mass  $M_{\text{BH}}$  as a function of the mass of a star, or sub-stellar object, for the latter to cross the event horizon without suffering significant tidal stresses. The arrow points the mass of the SMBH at the centre of our Galaxy, and the dashed lines the interval of masses for stars and brown dwarfs (BD) which can directly plunge without disruption.

self-gravitating systems. We cannot have an asymptotic thermodynamic limit because the gravitational forces are long-range and we cannot ignore the effect of a star which is “far away”. This translates into the fact that the a thermodynamical equilibrium is ruled out by construction. In spite of this, using thermodynamics in the context of stellar dynamics has proven to be an important asset. Nevertheless, surprises arise in this context, such as the concept of negative heat capacity [“(…) stars act like donkeys slowing down when pulled forwards and speeding up when held back.” 125].

We introduce now the fundamentals of relaxation theory, just as a way to understand in an intuitive way how to ponder the phenomena that lead, in the Newtonian limit, to centrophilic orbits; i.e. those which will approach the SMBH enough so as

to stand a chance of forming an EMRI. For a more detailed description, we remit the reader to [95, 154, 164, 39].

In relaxation, the potential of the dense stellar system is described by approximating it in the addition of two separated components. One is given by a dominating smooth contribution, which we will call  $\Phi_s$ , plus the contribution of individual stars,  $\delta\Phi$ , which are responsible for the phase-space distribution function to follow the collisionless Boltzmann equation.

A way to describe the evolution of these dense stellar systems is the Fokker-Planck (or Kolmogorov forward-) equation, which is a partial differential equation that allows one to study the time evolution of the velocity probability density function of a particle (a star) due to drag forces and random forces. When two stars interact with each other, the associated volume typically has dimensions which are small compared to the macroscopic lengths of the system, such as the radius of the galactic nucleus. We can then approximate the evolution by assuming that the entire cumulative effect of all encounters on our star are identical to an ideal situation. We assume that the star is embedded in a homogeneous system with the same local distribution function everywhere [this is usually referred to as the “local approximation”, see e.g. Sec. 8.5 of 18, for a detailed description].

As time flows, the accumulated variations of  $\delta\Phi$  alter  $E$  and  $J$  and lead to a modification of the distribution function. We then treat the role of the individual changes of  $\delta\Phi$  as the sum of uncorrelated hyperbolic encounters between two stars with a small deviation angle. Hence, if we consider a star “1” in a stellar system which is perfectly homogeneous of stars of the type “2”, with the same masses and velocities, after a time  $\delta t$  the initial trajectory will suffer a deflection  $\theta$  of

$$\begin{aligned} \langle \theta \rangle_{\delta t} &= 0, \\ \langle \theta^2 \rangle_{\delta t} &\simeq 8\pi N \ln \left( \frac{b_{\max}}{b_0} \right) \frac{G^2 (m_1 + m_2)^2}{v_{\text{rel}}^3} \delta t, \end{aligned} \quad (3)$$

with  $m_1, m_2$  the masses of two stars,  $N$  the stellar number density,  $b_0$  is the impact parameter that leads to a deflection angle of  $\pi/2$ ,  $b_{\max}$  is a normalisation factor to avoid logarithmic divergence (interpreted as the maximum impact parameter, of the order the size of the stellar system), and  $v_{\text{rel}}$  is the relative speed between star 1 and the background stars 2. We note that we obtain  $\langle \theta \rangle_{\delta t} = 0$  because this is a diffusion process, and hence  $\langle \theta^2 \rangle_{\delta t} \propto \delta t$ .

We define the velocity dispersion  $\sigma$  of the nucleus or cluster via the statistical concept of root mean square dispersion. The variance  $\sigma^2$  provides us with a measure of the dispersion of the observations within the statistical population at our disposal (i.e. the observational data). This means that

$$\sigma^2 = \frac{1}{N} \sum_{i=1}^N (V_i - \mu)^2.$$

Where  $V_i$  are the individual stellar velocities and  $\mu$  the arithmetic mean,

$$\mu_a \equiv \frac{1}{N} \sum_{i=1}^N V_i.$$

If we take  $M$ ,  $R$  as the total stellar mass and radius of the nucleus, respectively, and define  $m_*$  as the average stellar mass, then the argument of the Coulomb logarithm (remember our discussion about plasma physics) is approximately

$$\frac{b_{\max}}{b_0} \simeq \frac{v_{\text{rel}}^2 R}{G(m_1 + m_2)} \simeq \frac{\sigma^2 R}{GM} \simeq \gamma \frac{M}{m_*} = \gamma N. \quad (4)$$

In the last equation  $\gamma$  is a dimensionless proportionality constant. Note that this proportionality applies only to self-gravitating, virialized stellar systems. In order to derive the relaxation timescale of the system, we would have to integrate over all possible values of  $b_{\max}/b_0$ ; however in practise this is again approximated by assuming that  $\gamma$  is constant. This global value can be derived using analytical arguments [165, 96], which has been corroborated with numerical simulations. For systems composed of stars with a single type of mass, [96] derived  $\gamma \simeq 0.10 - 0.17$ . He also proved that this value should be significantly smaller in the case that we consider a mass spectrum.

When we analyse relaxation via the local approximation we are implicitly assuming that the dense stellar system is finite and homogeneous. Real systems however, are quite the contrary, with important density gradients. By adopting the local approximation we are imposing the fact that  $b \ll R$ . This allows us, as explained, to neglect  $\Phi_s$  -and hence approximate the trajectories as Keplerian orbits- as well as to use the local properties around star 1 as representative ones. This a priori conceptual grotesque approximation is however physically tolerable because we are talking about the argument of a logarithm,  $\ln(b_2/b_1)$ . This assumption has been tested in a large number of works and seems to be acceptable for pragmatic purposes [80, 167, 79, 146, 171, 166].

Although there is a conceptual problem in the way we have introduced it [see discussion in 18], we can use Eq. (4) to introduce a characteristic timescale associated to relaxation,

$$\langle \theta^2 \rangle_{\delta t} \simeq \left( \frac{\pi}{2} \right)^2 \frac{\delta t}{T_{\text{rlx}}}. \quad (5)$$

The full expression of this timescale is given in e.g. [50], and see [114]. In this work we will not derive it. We only introduced the basic notions so that the reader can develop a physical intuition for the process. The expression is

$$T_{\text{rlx}} = \frac{9}{16\sqrt{\pi}} \frac{\sigma^3}{G^2 m \rho \ln(\gamma N)}, \quad (6)$$

which can be rewritten as

$$T_{\text{rlx}} \sim 2 \times 10^{10} (\ln \Lambda)^{-1} \text{yrs} \left( \frac{\sigma}{100 \text{km/s}} \right)^3 \left( \frac{m}{1 M_{\odot}} \right)^{-1} \left( \frac{r}{1 \text{pc}} \right)^{\gamma}. \quad (7)$$

In this expression we have adopted a power-law distribution in the stellar density,  $\rho(r) \sim r^{-\gamma}$ , see [34, 158, 74, 138].

Within the influence radius of a SMBH  $r_{\text{infl}}$  (which can be loosely defined as the radius within which the potential is dominated by the SMBH), we can approximate as explained before  $b_{\text{max}} = r_{\text{infl}}$ , and relaxation leads to a steady-state distribution of orbital energies on, of course, a timescale  $\approx T_{\text{rlx}}$ .

So far we have considered that all stars have the same mass in the nucleus. This is obviously not correct. Stellar-mass black holes, in particular, have a higher mass than our Sun, which we adopt to be in this work  $m_{\text{bh}} = 10 M_{\odot}$ . If we consider that a fraction of all stars are stellar-mass black holes, typically as small as  $\approx 10^{-3}$  for a standard initial mass fraction [see e.g. 112], then a limiting form of relaxation leads to an interesting phenomenon. Stars, or COs, with masses larger than the average stellar mass, assumed to be of  $1 M_{\odot}$  will segregate in phase-space in a timescale shorter than the associated  $T_{\text{rlx}}$  by a factor given approximately by the ratio  $Q$  of the average stellar mass divided by the mass of the CO. I.e. if  $m_{\text{bh}} = 10 M_{\odot}$  and  $m = 1 M_{\odot}$ , this timescale is 1/10 of  $T_{\text{rlx}}$ . This limiting form of relaxation was described by Chandrasekar [see e.g. 39] and is called dynamical friction, with the associated timescale

$$T_{\text{DF}} = \frac{v_c^3}{4\pi G^2 \rho m_{\text{bh}} \ln \Lambda} \left[ \text{erf}(X) - \frac{2X}{\sqrt{\pi}} e^{-X^2} \right]^{-1} \sim \frac{\langle m \rangle}{m_{\text{bh}}} T_{\text{rlx}} := \frac{T_{\text{rlx}}}{Q}, \quad (8)$$

where  $v_c$  is the (local, obviously) circular velocity,  $\rho$  is the mass density of the stars others than COs, the mass ratio is  $Q = m_{\text{bh}}/m$  and  $X = v/(\sqrt{2}\sigma)$ . What this means is that we *do* expect to have stellar-mass black holes very close to the SMBH in a timescale shorter than the  $T_{\text{rlx}}$ , which is what we need to create the orbit which will ultimately lead to an EMRI.

This leads us to the question whether nuclei in the bandwidth of LISA will have  $T_{\text{rlx}}$  shorter than a Hubble time because otherwise the nuclei will not be relaxed, and hence we cannot expect stellar-mass black holes close to the SMBH. If nuclei which are target of LISA, i.e. with masses approximately ranging between  $10^4 - 10^7 M_{\odot}$  are not *relaxed*, then we cannot expect EMRIs to be detected.

If these nuclei follow the so-called mass-sigma relationship (which is not clear, since they are at the low-mass end of the correlation, see e.g. [107]),  $M_{\text{BH}} \propto \sigma^4$ , then we can express the influence radius assuming that the nucleus is isothermal (i.e.  $\rho \sim r^{-2}$ ,  $\sigma(r) = \text{constant}$ , for  $r \gtrsim \text{few} \times 10^{-1} r_{\text{infl}}$ ) as  $r_{\text{infl}} \sim GM_{\text{BH}}/\sigma^2 \propto M_{\text{BH}}^{1/2}$ . On the other hand, the average stellar density at  $r_{\text{infl}}$  can be estimated roughly to be  $\rho \sim 2M_{\text{BH}}/(r_{\text{infl}}^3)$  (since we have the same mass in stars as the mass of the SMBH). The velocity dispersion within  $r_{\text{infl}}$  is  $\sigma^2(r) \sim GM_{\text{BH}}/r$  (as determined via the Jeans equation, see [39]), so that we finally have  $T_{\text{rlx}} \sim \sigma^3/\rho$ , which means that

$$T_{\text{rlx}} = \frac{17}{100} (m\Lambda)^{-1} \left( \frac{M_{\text{BH}}}{G} \right)^{1/2} r_{\text{infl}}^{3/2} \quad (9)$$



Adopting  $\ln A \sim \ln(M_{\text{BH}}/m_{\text{bh}}) \sim 11.5$  (see Eq. 13 of [18]), and normalising to typical values, we find that

$$T_{\text{rlx}} \cong 1.1 \times 10^9 \text{ yrs} \left( \frac{M_{\text{BH}}}{4 \times 10^6 M_{\odot}} \right)^{1/2} \left( \frac{\langle m \rangle}{0.4 M_{\odot}} \right)^{-1} \left( \frac{r_{\text{infl}}}{1 \text{ pc}} \right)^{3/2}, \quad (10)$$

where we have used the average stellar mass at the Galactic Centre. This can be roughly derived by assuming that  $\langle m \rangle = M_{\text{tot}}/N_{\text{tot}}$ , with  $M_{\text{tot}}$  the total stellar mass and  $N_{\text{tot}}$  the total number of stars. In our approximation, we only consider main sequence stars and stellar-mass black holes, which represent a fraction  $10^{-3}$  of the total number. Using a typical IMF, the average stellar mass is of  $\sim 0.4 M_{\odot}$ , which is in agreement with the Milky-Way models of [72].

Using the fact that stellar distribution follows a power-law expression of the radius, as explained before, we can furthermore derive that [see 19]

$$r_{\text{infl}} \simeq 2.5 \text{ pc} \left( \frac{M_{\text{BH}}}{4 \times 10^6 M_{\odot}} \right)^{3/5}. \quad (11)$$

Then, we are finally left with

$$T_{\text{rlx}}^{\text{tot}} \cong 4.35 \times 10^9 \text{ yrs} \left( \frac{M_{\text{BH}}}{4 \times 10^6 M_{\odot}} \right)^{11/10} \left( \frac{\langle m \rangle}{0.4 M_{\odot}} \right)^{-1}. \quad (12)$$

In this expression we have the relaxation time as a function only of the mass of the SMBH, while taking into account the scaling of the influence radius with this mass. This allows us to have an idea of what nuclei will be relaxed. We depict this in Fig (6) for a range of masses, and note that in the low-end of masses the results should be taken with skepticism, since SMBHs with light masses will wander off the centre. By wandering off, the massive black hole (in this case an IMBH) could potentially explore regions of phase-space with different relaxation times and, since the wandering timescale is much shorter than the relaxation timescale, the system does not have time to re-adjust. Hence any capture is led by a dynamical process, and not a relaxational one.

It is remarkably interesting to note that the relaxation time will exceed a Hubble time for nuclei harbouring SMBHs with masses slightly above  $10^7 M_{\odot}$  (the exact number should not be envisaged as a realistic one in view of the -few- assumptions that we have made in the derivation). Surprisingly, this type of masses fit perfectly well in the kind of nuclei that LISA will probe. If this had not been the case, LISA would never be able to detect an EMRI. To the best of my knowledge, nobody thought of this potential risk before designing the sensitivity curve of the instrument. I would appreciate it if somebody could provide me with more details, in case that I am wrong (which is a possibility, obviously).

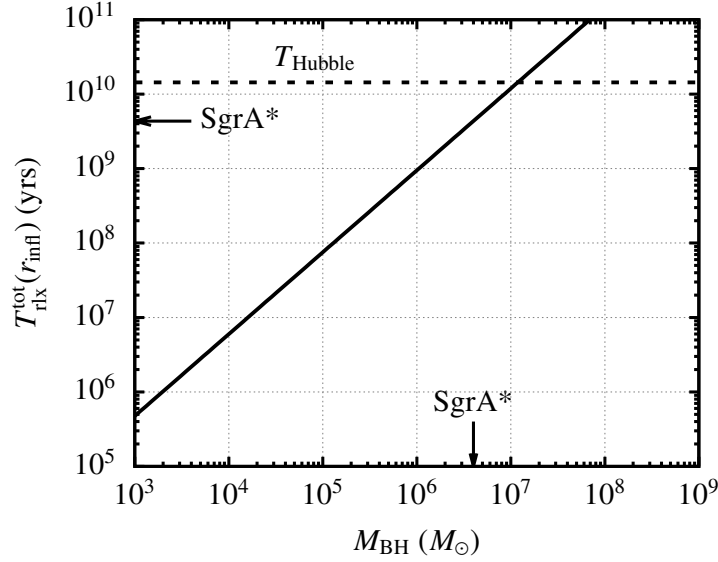


**Fig. 6** Relaxation time as a function of the SMBH mass  $M_{\text{BH}}$ . The horizontal, dashed line marks the Hubble time limit, the arrows the position of the SMBH in our Galaxy and in the relation we have taken into account the influence radius as a function of  $M_{\text{BH}}$ . Nuclei harboring SMBHs with masses  $M_{\text{BH}} \gtrsim 10^7 M_{\odot}$  have a relaxation time longer than the age of the Universe and have not had time to converge into a steady-state and develop segregated stellar cusps. Their stellar distribution keep memory from their formation and (if any) of the last strong perturbation process.

### The loss-cone

After having conceptually introduced what is the relaxation of a dense stellar system, we now look at the definition of the region of phase-space denoted as the “loss-cone”. Not all stars in a galactic nucleus or a globular cluster will have such an energy and angular momentum that will bring them very close to the SMBH; after all, from the point of view of the stellar system, the SMBH is something microscopic, with a size (i.e. a Schwarzschild radius) of  $R_{\text{Schw}} \simeq 3.8 \times 10^{-7}$  pc if its mass is that of SgrA\*. In comparison, its influence radius, as we have seen, is about  $r_{\text{infl}} \simeq 2.5$  pc, i.e. seven orders of magnitude bigger in length.

Only a very peculiar subset of all stars with a given semi-major axis will have an eccentricity high enough to bring them close at periapsis to interact with the SMBH. Since historically this was studied in the context of stellar disruptions, interest this subset is dubbed the “loss-cone”, because (1) the orbit around the SMBH can be defined in terms of an angle such that will lead the star to get close enough to the SMBH and (2) if at periapsis it crosses the tidal radius, the star can be tidally disrupted, as we saw before, and is hence lost for the system.

Previously we introduced the relaxation time. It is useful to define another interesting timescale, the dynamical timescale or the “crossing time”. This is the time required for a star to cross the host dense stellar system. For a cluster,  $T_{\text{dyn}} = r_{\text{infl}}/\sigma_{\text{infl}}$ ,

where  $\sigma_{\text{infl}}$  is the velocity dispersion at the influence radius. If we impose Virial equilibrium, then  $T_{\text{dyn}} \approx \sqrt{r_{\text{infl}}^3 / (GM_{\text{infl}})} \simeq (G\rho)^{-1/2}$ , with  $M_{\text{infl}}$  the total stellar mass comprised within  $r_{\text{infl}}$  (which is in order of magnitude equivalent to the mass of the SMBH).

Following our previous discussion of (cheating with) thermodynamics, we note that contrary to a gaseous system, in a stellar system the thermodynamical equilibrium timescale will be much longer than the crossing one,  $T_{\text{rlx}} \ll T_{\text{dyn}}$ . If we consider a perfectly homogeneous stellar system, we will reach a stationary state in the limit  $t \rightarrow \infty$ . How quickly a Virial equilibrium is reached depends on the timescale in which a perturbation in the stellar system is washed out.

We have introduced the relaxation time as the time that we need to wait for the system to “mix up”, i.e. more formally, for the perpendicular velocity component of a star to be of the same order than the perpendicular velocity component itself,  $\Delta v_{\perp}^2 / v_{\perp}^2 \simeq 1$ , as illustrated in Fig (7). I.e. the relaxation time is the required time to induce a change in the perpendicular velocity component of the same order as the perpendicular velocity component  $v_{\perp}$  itself,  $\Delta v_{\perp}^2 \simeq v_{\perp}^2$ , after a number of dynamical times (e.g. crossing times)  $n$ , which allows us to define the associated timescale for mixing up the system:  $\Delta v_{\perp}^2 / v_{\perp}^2 = T / T_{\text{rlx}}$ , as in e.g. [39]. This means that we have that  $\Delta v_{\perp}^2 / v_{\perp}^2 = n \delta v_{\perp}^2 / v_{\perp}^2 = 1$ , so that  $T_{\text{rlx}} = n T_{\text{dyn}} = (v_{\perp}^2 / \delta v_{\perp}^2) T_{\text{dyn}}$ .

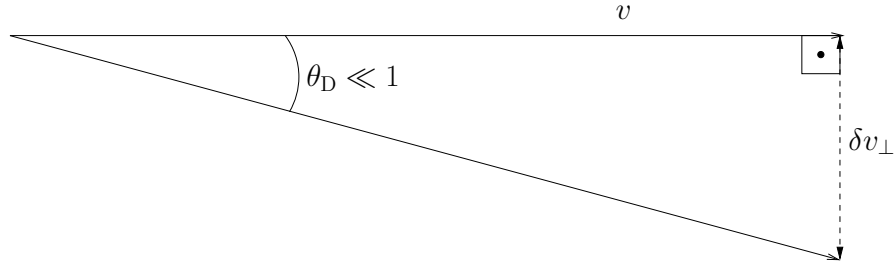


**Fig. 7** The change in the perpendicular component of the velocity of the star is assumed to be small after every single encounter with another star. This leads to the definition of a diffusing angle  $\theta_D$  which, ab definitiō (see text) must be small. When this component is of the same order than the perpendicular velocity component itself, a relaxation time has passed.

The mean deviation of a orbit in a dynamical timescale  $T_{\text{dyn}}$  (which is typically defined as the time required for a star to cross the system) can be estimated via a “diffusion angle”  $\theta_D^2 := T_{\text{dyn}} / T_{\text{rlx}}$ , and we furthermore assume that this angle is very small, following the line of thought of e.g. [71, 26, 117, 10]. Therefore,  $\sin \theta_D \simeq \delta v_{\perp} / v \simeq \theta_D$ , and so  $\theta_D \simeq \sqrt{T_{\text{dyn}} / T_{\text{rlx}}}$ . This angle is very useful to understand the evolution of the system; it will help us to quantify how efficiently (or not) the loss-cone can bring stars close to the SMBH.

Stars which *are* in the loss-cone are lost in a dynamical time, i.e. a crossing time. We can define the stars that belong to the loss-cone by evaluating the angular momentum of the star, the influence radius and the velocity dispersion of the system.

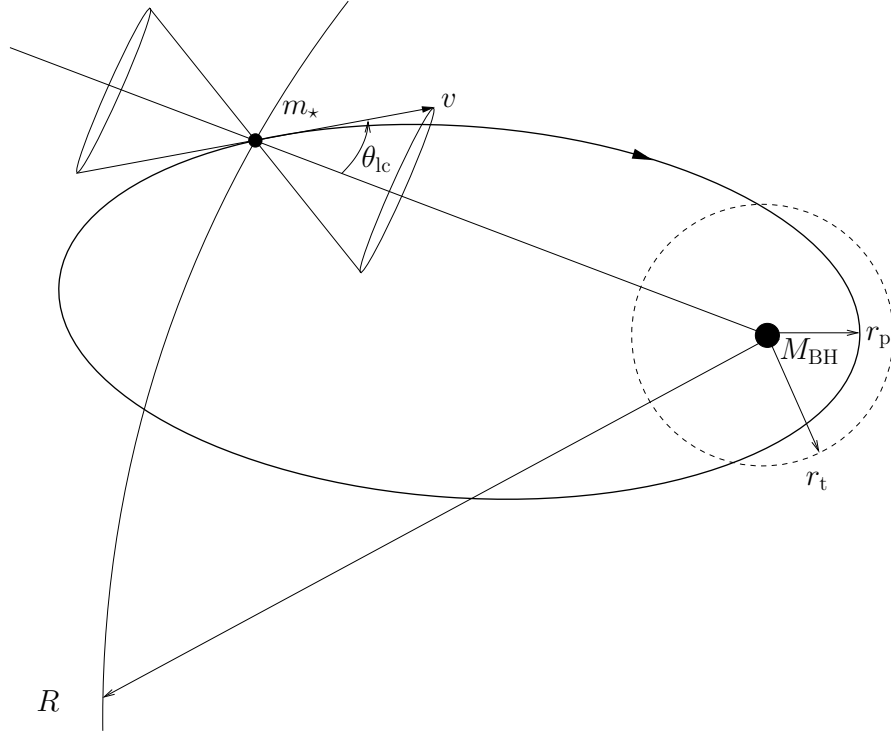


**Fig. 8** Definition of the loss-cone angle for a star of mass  $m_*$  approaching a SMBH of mass  $M_{\text{BH}}$ .

We can illustrate this angle in an approximate way as in Fig. (8). If the star of mass  $m_*$  has a velocity vector such that the periastron distance  $r_p$  falls within the tidal radius  $r_t$ , it will suffer important tidal stresses. A total disruption happens when the so-called “penetration factor”  $\beta := r_t/r_p > 1.85$ , see [88]. This will happen when  $r_p(E, L) \leq r_t$  and  $\theta \leq \theta_{lc}$ . One can show that the loss-cone angle is  $\theta_{lc} = \sqrt{2r_t/(3r)}$ , with  $r_t$  the tidal radius and  $r$  the distance from the MBH to the star, if  $r \leq r_{\text{infl}}$ , and  $\theta_{lc} \simeq \sqrt{2r_t r_{\text{infl}}/(3r)}$  for  $r \geq r_{\text{infl}}$  [for details about this derivation, see e.g. 18].

With these considerations we can define a critical radius which will determine the future of stars in the loss-cone. If we define the ratio  $\xi := \theta_{lc}/\theta_D$ , when  $\xi = 1$ ,  $\theta_{lc} = \theta_D$ , which can be converted into a distance  $r_{\text{crit}}$ . Stars inside this radius are removed on a  $T_{\text{dyn}}$  because  $\xi > 1$ ,  $\theta_{lc} > \theta_D$ .

We can therefore make an educated guess for the loss-cone to be replenished. The conditions is that  $\xi^2 \times T_{\text{dyn}}$ , where the square appears because, as illustrated in Fig. (9), the surface which corresponds to the radius  $b$  must cover the empty surface of radius  $a$ .

When a star is outside of the critical radius, even if it is in the loss-cone, it will be diffused out of the it before it can reach the central SMBH. This is so because  $\xi < 1$ ,  $\theta_{lc} < \theta_D$ , and by definition,  $\theta_D$  corresponds to the variation of  $\theta$  in a  $T_{\text{dyn}}$ . Inside of

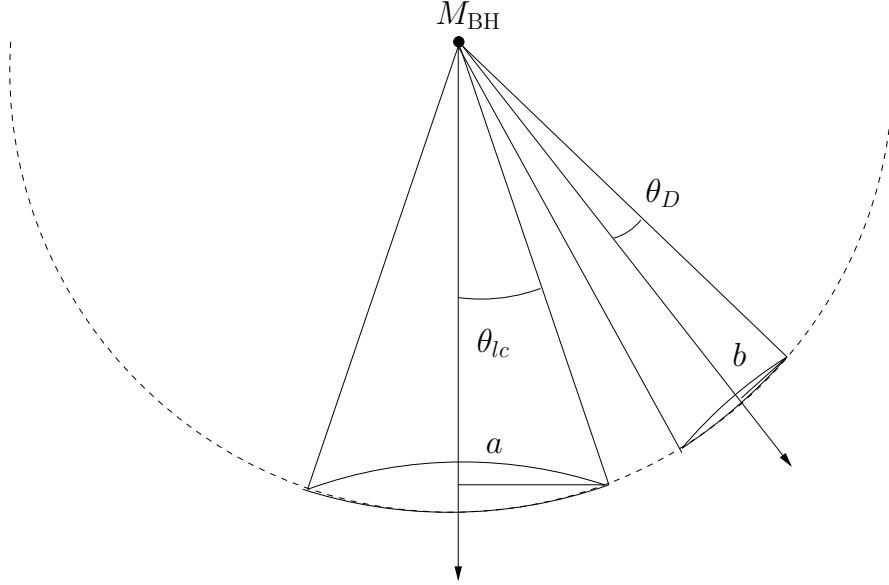


**Fig. 9** Definition of the critical radius via the loss-cone- and diffusion angles.

the critical radius, however, stars will fall on to the SMBH without being perturbed. We have that  $\xi = a/b$  because  $a = v \sin \theta_{lc} \approx v \theta_{lc}$ , and  $b = v \sin \theta_D \approx v \theta_D$ .

Whilst it would be ideal to be able to define a relativistic loss-cone, i.e. a “GW-cone”, in practise this turns out to be challenging, if not impossible. In Fig. (10) we depict the complications of this situation. The orbits are not closed and shrinking over time and, if the central SMBH is Kerr, there will be a change in the inclination of the orbit when the CO approaches the pericentre.

### ***Formation of EMRIs via relaxation***

The evolution of a CO on its way to becoming a source of gravitational waves is determined by two very different types of physics: stellar dynamics, for which we do not have to bother with general relativistic effects, but with two-body relaxation, and gravitational radiation. Since we obviously cannot solve the  $10^6 - 10^8$  problem in Newtonian gravity and not even the two-body problem in general relativity (even less at these mass ratios), we need to work with timescales to derive information about the process. We can define a threshold that separates the evolution via dynamics from general relativity by equating the two associated timescales, times a factor  $C$  of order 1,

$$T_{\text{rlx,peri}} = C T_{\text{GW}}(a, e) \quad (13)$$

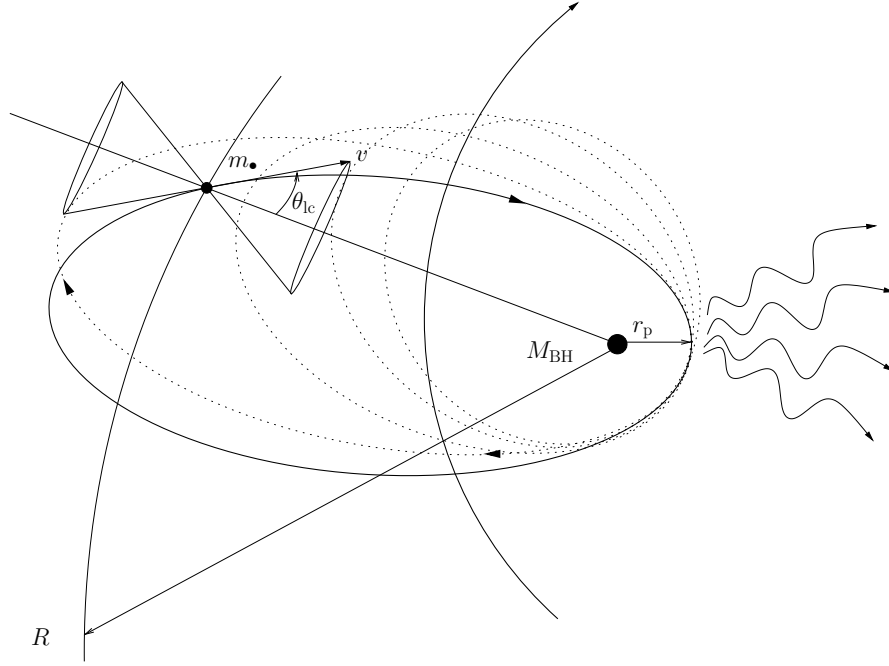


**Fig. 10** Same as Fig. (8) but for a CO orbiting around a SMBH. The orbit precesses, losses energy and thus shrinks over time and the plane of the orbit basculates due to frame-dragging if the SMBH is spinning, which is not shown in the illustration because it is a two-dimensional projection. At periapsis, there is a strong burst of gravitational radiation and the semi-major axis of the orbit shrinks a bit (the shrinkage is not to scale, as well as the precession). This figure illustrates the difficulty of defining analytically the relativistic equivalent of the loss-cone treatment for a tidal disruption.

In this equation,  $T_{\text{rlx,peri}}$  is the relaxation time at pericentre, i.e.,  $T_{\text{rlx,peri}} := T_{\text{rlx}}(a) \times (1 - e)$  [8], and  $T_{\text{GW}}$  the time derived in the approximation of Keplerian ellipses of [141]. Since the initial eccentricities of EMRIs are typically very large, as we will explain later, the function  $F(e)$  of  $T_{\text{GW}}(a, e)$  can be estimated to be  $F(e) = 425/(768\sqrt{2})$ . We also have to equate

$$\frac{8GM_{\text{BH}}}{c^2} = a(1 - e), \quad (14)$$

with  $c$  the speed of light and we note that the position of the last-stable orbit (LSO) depends on (i) the spin of the central SMBH  $a_{\bullet}$ , (ii) the inclination of the orbit  $\theta$ , and (iii) whether the orbit is pro- or retrograde, as described in the work of [13]. This is of course only true for Kerr SMBHs. The Schwarzschild case serves as a reference point, which has the LSO at a distance of  $4R_{\text{S}}$ , with  $R_{\text{S}}$  the Schwarzschild radius. The work of [13] provides us with the function  $\mathcal{W}(\theta, a_{\bullet})$  which captures this information and accordingly modifies the position of the LSO. This position is

crucial because it determines the upper integration limit when calculating the event rate, as we will discuss. In Fig. (11) we give the full shape of the function.

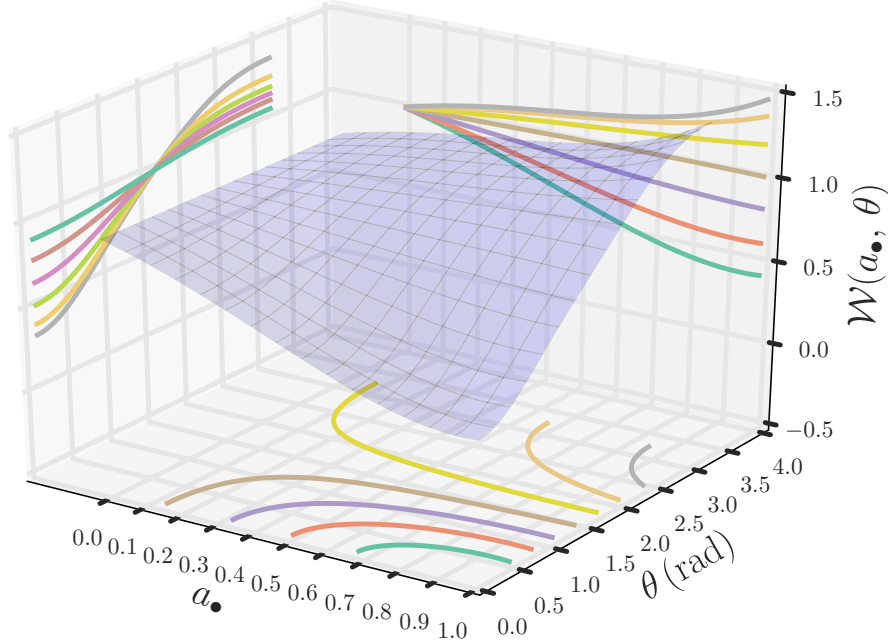


**Fig. 11** Function  $\mathcal{W}(\theta, a_*)$  which gives us the multiplying factor to identify the location of the LSO for a Kerr SMBH relative to the Schwarzschild case for prograde and retrograde orbits.

The GW timescale is given by

$$T_{\text{GW}}(a, e) \sim \sqrt{2} \frac{24}{85} \frac{c^5}{G^3} \frac{a^4 (1-e)^{7/2}}{m_{\text{CO}} M_{\text{BH}}^2}, \quad (15)$$

where  $m_{\text{CO}}$  is the mass of the CO in consideration. It could be a neutron star, a white dwarf, a stellar-mass black hole or even a brown-dwarf, which is not a compact object, but in the case of masses in the range of SgrA\*, as we have discussed, a powerful source of gravitational radiation. This is important, because the timescale is given by two bodies only, the SMBH and the CO. Moreover, we note that stars with different masses will segregate in different fashions. I.e. the density profile will follow a different power-law but, still, relaxation will be dominated by stellar-mass black holes, as discussed in [19]. This implies that, while relaxation is the driving mechanism dominating the stellar dynamical evolution, and is provided by the stellar-mass black holes at the radii of relevance, the CO must not necessarily follow the same density distribution as that of the stellar-mass black holes. This is why we will use two different power indices,  $\gamma$  for the distribution of stellar-mass black holes, and  $\beta$  for the distribution of the other species, the COs. Similarly, we



will use two separated masses, one for the stellar-mass black holes,  $m_{\text{bh}}$  and another for the COs,  $m_{\text{CO}}$ . If we are interested in EMRIs, then obviously  $m_{\text{bh}} = m_{\text{CO}}$  and  $\gamma = \beta$ .

As shown in [19], we can define the threshold between dynamics and general relativity taking into account the change of relaxation as a function of the radius with

$$(1-e)^{5/2} = \frac{4.26}{(3-\gamma)(1+\gamma)^{3/2}} \frac{85}{24} \frac{1}{\sqrt{2}c^5} \frac{G^{5/2}}{\ln(\Lambda)} \frac{M_{\text{bh}}^{7/2}}{N_{\text{BH}}} \frac{m_{\text{CO}}}{m_{\text{bh}}} R_0^{3-\gamma} a^{\gamma-11/2}. \quad (16)$$

In this equation  $R_0$  is the radius within which relaxation, as discussed before, is dominated by stellar-mass black holes. Accordingly,  $N_{\text{BH}}$  is how many of them are enclosed within  $R_0$ . We choose  $R_0 \equiv r_{\text{infl}}$ .

This allows us to solve for the critical semi-major axis, which is given by

$$a_{\text{crit}} = r_{\text{infl}} \left[ \frac{C}{4.26} \frac{6144}{85} (3-\gamma)(1+\gamma)^{3/2} \right]^{\frac{1}{\gamma-3}} \times \left[ \mathcal{W}(\theta, a_{\bullet})^{5/2} N_{\text{BH}} \ln(\Lambda) \left( \frac{M_{\text{BH}}}{m_{\text{CO}}} \right) \left( \frac{M_{\text{BH}}}{m_{\text{bh}}} \right)^{-2} \right]^{\frac{1}{\gamma-3}}, \quad (17)$$

With the threshold between dynamics and general relativity and  $a_{\text{crit}}$ , we can now plot the evolution of a potential source of GWs in phase-space. We represent this in Fig. (12). The source describes a random-walk-like evolution in energy and angular momentum due to the interaction with other stars in the stellar system, since we are on the right-hand of the red line, with a larger scatter in eccentricity than in semi-major axis until it crosses the threshold given by Eq. (16). From that moment onwards, on the left-hand of the red line, the driving mechanism is gravitational radiation and the evolution in phase-space follows very closely one of the green lines, which gives the relation between the semi-major axis and the eccentricity in the two-body problem as approximated by [141]. We note however, that for strong-field and fast-motion orbits, radiation reaction will enhance the eccentricity for very small values of the semi-major axis (i.e. if the semi-latus rectum  $p$  is close to its minimum value  $6+2e$ ), which can be used as an indicator of the imminent plunge of the orbit [60]. We give an example of this in Fig. (17), and see the discussion in the text of that section.

EMRIs with  $a \ll a_{\text{crit}}$  will have a much lower event rate because in the power-law solution for the stellar distribution, we have that the numerical density of stars  $n \propto r^{-\gamma}$ , so that the total number of stars  $N$  per unit  $\log(a)$  scales as  $dN/d(\log a) \propto a^{(3-\gamma)}$ . Moreover, as we move to deeper and deeper radii, the value of  $\gamma$  is lowered [117, 11]. This is so because the loss-cone is much more quickly depleted and in order to re-populate it we need to wait for several relaxation times. Also, as we get closer to the SMBH, the value of the relaxation time increases, as we can see

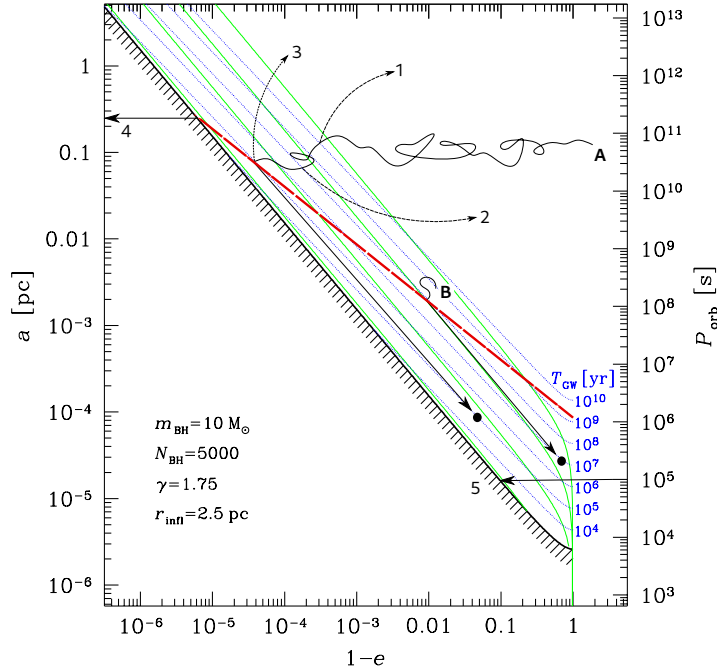


**Fig. 12** Evolution in phase-space (semi-major axis and orbital period as a function of the eccentricity) of a potential source of GWs, represented with a black circle. The mass of the SMBH is of  $M_{\text{BH}} = 4 \times 10^4 M_{\odot}$ . The green lines show the correlation between  $a$  and  $e$  as given in [141], and the blue, dotted lines are the isochrones for a given  $T_{\text{GW}}$ , as described in Eq. (15). The *standard relaxation scenario* is marked with the letter “A”: We have marked a few important points. The first and the second points show the dynamical parameters for which the CO would merge in less than  $10^{10}$  and  $10^8$  respectively, if it only evolved due to the emission of gravitational radiation, which is not the case, because the source is on the right of the oblique, dashed red line, where dynamics dominate the evolution. Point three represents the crossing of this very line, from which the evolution is dominated uniquely by GWs. Point four is the conjunction of the LSO (for a Schwarzschild SMBH) and the threshold line, which defines in the Y-axis the critical semi-major axis  $a_{\text{crit}}$ , and finally point five is a rough location of where the LISA bandwidth starts (based on the orbital period, which will change depending on the dynamical properties of the CO). The *tidal separation scenario*, which will be discussed later, is marked with the letter “B”: We can see that, when entering the LISA band, these sources will have significantly lower eccentricities. The values which we have chosen for this plot are shown in the left, bottom corner.

from Eq. (6) and Eq. (7). Indeed, unless SMBHs in the Universe are Schwarzschild, which is very unlikely [161], EMRIs will originate at large semi-major axes with very high eccentricities [see discussion in 13].

### ***Formation of EMRIs via tidal separation of binaries***

An interesting idea about how to produce an EMRI has its origins in the work of [98], who estimated that, in the same way a star can be tidally disrupted, as we have seen in Sec. (), a binary could be separated, “ionised”, via the same process: The gravitational forces acting on to one of the two companions would be different than on the other one, and depending on the distance to the SMBH, this difference of forces could overcome the binding energy of the star. He predicted that this would lead to the creation of the so-called “hyper-velocity stars”, stars with a velocity of  $> 10^3 \text{ km s}^{-1}$ . The discovery of these stars in the work of [43] led to literally an avalanche of theoretical and observational work. Among these works, Miller and collaborators in [134] presented an interesting idea. If one of the two stars happened to be a CO, more specifically a stellar-mass black hole. Because the separation happens very close to the SMBH, the stellar-mass black hole could eventually become an EMRI. These EMRIs, contrary to those produced by relaxation, would have a much lower eccentricity when entering the LISA band, as we can see in Fig. (12), case “B”. Because the initial semi-major axis is smaller than in the relaxation case “A”, the eccentricity at bandwidth entrance is much lower.

As in the tidal disruption problem, we can derive the splitting radius, which obviously is very similar to the former one,

$$R_{\text{split}} \sim a \left( \frac{M_{\text{BH}}}{m_{\text{bin}}} \right)^{1/3}, \quad (18)$$

with e.g.  $m_{\text{bin}} = m_{\star} + m_{\text{CO}}$ , if one of the companions is a star and the other one a CO. To get an idea of the ejection velocity that the companion will receive, we note that the orbital velocity is  $v_{\text{orb}} \sim \sqrt{G m_{\text{bin}} / a}$ , i.e.

$$v_{\text{orb}} \simeq 312 \text{ km s}^{-1} \left( \frac{m_{\text{bin}}}{11 M_{\odot}} \right)^{1/2} \left( \frac{a}{0.1 \text{ AU}} \right)^{-1/2}, \quad (19)$$

assuming that  $m_{\star} = 1 M_{\odot}$  and  $m_{\text{CO}} = 10 M_{\odot}$ . Note that this is just an example, because in a nucleus it is more likely that the mass of the extended star has a similar mass to that of the CO. Assuming a parabolic encounter, which is the most probable scenario, the velocity of the centre-of-mass  $V_{\text{CoM}}$  can be estimated to be

$$V_{\text{CoM}} \gtrsim \sqrt{\frac{G M_{\text{BH}}}{R_{\text{split}}}} \sim v_{\text{orb}} \left( \frac{M_{\text{BH}}}{m_{\text{bin}}} \right)^{1/3} \simeq 1.4 \times 10^4 \text{ km s}^{-1} \gg v_{\text{orb}}, \quad (20)$$

for a  $M_{\text{BH}} = 10^6 M_{\odot}$ . Following the derivations of [18], we have that the ejection velocity of the companion is  $v_{\text{eject}} \gtrsim (M/m_{\text{bin}})^{1/6}$  and the new semi-major axis of the binary  $a_{\text{capt}} \approx a (M_{\text{BH}}/m_{\text{bin}})^{2/3} \simeq 10^4 a \simeq 5 \times 10^{-4} \text{ pc}$ . One can approximate the separation radius  $R_{\text{split}}$  to the periapsis distance, and with that information we can derive the initial eccentricity when the CO is captured by the SMBH is of  $e_{\text{capt}} = 1 - (M_{\text{BH}}/m_{\text{bin}})^{-1/3} \simeq 0.97$  for the values that we have adopted here.

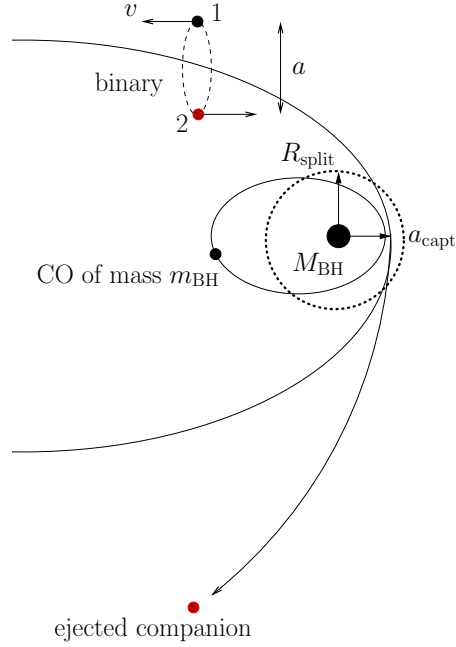


**Fig. 13** Tidal separation of a binary of two stars of semi-major axis  $a$ . We consider star “1” to be a compact object of mass  $m_{\text{BH}}$  which is gravitationally bound to the SMBH of mass  $M_{\text{BH}}$  because the orbit crosses the splitting radius  $R_{\text{split}}$ . This radius is equivalent to the tidal disruption radius in the tidal disruption problem. After the separation, star 2 is ejected and star 1 forms a new binary around the SMBH with a new semi-major axis  $a_{\text{capt}}$ , which typically is much smaller than  $a_{\text{crit}}$  as defined in Eq. (17). This leads to much smaller eccentricities in the LISA band.

These values for the initial semi-major axis and eccentricity are responsible for the source to enter the LISA band at much lower eccentricities, as we can see in Fig. (12), case B (which correspond to a slighter more massive SMBH, of  $4 \times 10^4 M_{\odot}$ ). This signature in the eccentricity as compared to a relaxation EMRI is what will allow us to extract information about the mechanism that produced the source in the first place. This is so because if we set all dynamical parameters of two EMRIs identical but for the eccentricity, we can calculate the mismatch  $M$  between them, as done in [18], to find

$$M := 1 - \frac{\langle h_{\text{rlx}} | h_{\text{bin}} \rangle}{\sqrt{\langle h_{\text{rlx}} | h_{\text{rlx}} \rangle \langle h_{\text{bin}} | h_{\text{bin}} \rangle}} = 99.9971\%, \quad (21)$$

with  $h_{\text{rlx}}$  and  $h_{\text{bin}}$  the waveforms of an EMRI produced via relaxation and binary separation respectively, using the kludge approximation of [73]. The natural scalar product  $\langle | \rangle$  is introduced by treating the waveforms as vectors in a Hilbert space [94], and we refer to this work as well as to [173, 69] for further details. For this kind of sources, as a rule of thumb, a mismatches  $M < 0.1$  will make detection

impossible, and a mismatch of  $M < 10^{-3}$  will make parameter extraction challenging [see e.g. 55, 56, 122, 61].

### ***Geodesic motion and relativistic precession***

In this section, which profits from parts of [12], we give a summary of the concepts that we will need for the evolution of an EMRI around a Schwarzschild SMBH, the geodesic motion and relativistic precession. The Kerr case is much more complex and we will simply give an illustrative summary. We then give examples that solve the evolution of an EMRI (or an IMRI, XMRI) in phase-space by resorting to approximate, semy-analytical and numerical techniques.

#### **Geodesic motion around a Schwarzschild black hole**

The only spherically symmetric solution of Einstein's equations for vacuum is the Schwarzschild solution (Birkhoff's theorem)<sup>2</sup>

$$ds^2 = -f dt^2 + \frac{dr^2}{f} + r^2 d\Omega^2, \quad f = 1 - \frac{2M_{\text{BH}}}{r}, \quad d\Omega^2 = d\theta^2 + \sin^2 \theta d\varphi^2. \quad (22)$$

This solution predicts the existence of a horizon at  $r_g = 2M_{\text{BH}}$  ( $= 2GM_{\text{BH}}/c^2$  in *normal* unit conventions) and hence a *black hole* geometry. We are interested in the motion of a test mass around such black hole (whose geometry is described by Eq. (22)). As in Newtonian gravity, the motion takes place in a plane that we can take to be the equatorial plane  $\theta = \pi/2$ . There are two constants of motion, the energy  $\mathcal{E}$  and the angular momentum  $\mathcal{J}$ , associated with the time and azimuthal Killing symmetries<sup>3</sup>. Thanks to this the motion is completely separable and hence integrable. Let us see how this works. The energy and angular momentum,  $(\mathcal{E}, \mathcal{J})$ , in terms of the Schwarzschild coordinates of Eq. (22), can be written as:

$$\mathcal{E} = f \frac{dt}{d\tau}, \quad \mathcal{J} = r^2 \frac{d\varphi}{d\tau}, \quad (23)$$

where  $\tau$  denotes proper time (the time measured by the clocks of an observer moving with the test mass) and  $t$  is the coordinate time of Eq. (22), the time measured by the clocks of distance observers, at infinity). Notice that the constants of motion

<sup>2</sup> Using normal units we have

$$f = 1 - \frac{2GM_{\text{BH}}}{c^2 r}$$

where  $G$  is Newton's constant and  $c$  denotes the speed of light.

<sup>3</sup> We use the letters  $(\mathcal{E}, \mathcal{J})$  to distinguish them from the Newtonian definitions,  $(E, J)$ . Later we will see what are the relations between them.

( $\mathcal{E}$ ,  $\mathcal{J}$ ) are also *specific* constants of motion (per unit mass of the test particle), like in the Newtonian situation of Eqs. (106) and (107).

In the language of General Relativity, we have the four velocity

$$u^\mu = \frac{dx^\mu}{d\tau}, \quad (u^\mu) = \left( \frac{dt}{d\tau}, \frac{dr}{d\tau}, \frac{d\theta}{d\tau}, \frac{d\varphi}{d\tau} \right), \quad (24)$$

which is a normalized vector with respect to the metric (because it has been defined in terms of proper time)

$$g_{\mu\nu} u^\mu u^\nu = -1, \quad (25)$$

where  $g_{\mu\nu}$  are the metric components, which in the case of Schwarzschild can be read off from Eq. (22). Then, Eq. (25) is equivalent to the following expression:

$$-1 = -f \left( \frac{dt}{d\tau} \right)^2 + \frac{1}{f} \left( \frac{dr}{d\tau} \right)^2 + r^2 \left[ \left( \frac{d\theta}{d\tau} \right)^2 + \sin^2 \theta \left( \frac{d\varphi}{d\tau} \right)^2 \right]. \quad (26)$$

If we substitute in this equation  $dt/d\tau$  and  $d\varphi/d\tau$  from Eq. (23) and use the choice  $\theta = \pi/2$ , which implies  $d\theta/d\tau = 0$ , we obtain the following equation for the radial motion:

$$\left( \frac{dr}{d\tau} \right)^2 = \mathcal{E}^2 - \left( 1 + \frac{\mathcal{J}^2}{r^2} \right) \left( 1 - \frac{2M_{\text{BH}}}{r} \right). \quad (27)$$

To summarize, the equations of motion, in terms of proper time are:

$$\frac{dt}{d\tau} = \frac{\mathcal{E}}{1 - \frac{2M_{\text{BH}}}{r}}, \quad (28)$$

$$\left( \frac{dr}{d\tau} \right)^2 = \mathcal{E}^2 - \left( 1 + \frac{\mathcal{J}^2}{r^2} \right) \left( 1 - \frac{2M_{\text{BH}}}{r} \right), \quad (29)$$

$$\frac{d\varphi}{d\tau} = \frac{\mathcal{J}}{r^2}. \quad (30)$$

Eq. (28) just gives the relation between coordinate time  $t$  and proper time  $\tau$ . We can use it, to rewrite the equations of motion, the geodesics, in terms of coordinate time.

For the purposes of this work, it is very convenient to introduce in an appropriate way a three-velocity. This can be done in a *natural* way by factoring out the time-component of the four velocity:

$$u^\mu = u^t v^\mu = u^t (1, v^i), \quad v^i \equiv \frac{u^i}{u^t}. \quad (31)$$

Here, it is important to notice that this three-velocity, or better spatial velocity, is now defined in terms of the coordinate time  $t$  as follows

$$v^i = \frac{dx^i}{dt}. \quad (32)$$

In this way, and by virtue of the normalization property of  $u^\mu$ , we can interpret  $u^t$  as the relativistic gamma factor associated with the observers that measure the coordinate time  $t$ :

$$g_{\mu\nu}u^\mu u^\nu = -1 \quad \Rightarrow \quad u^t = \frac{1}{\sqrt{-g_{tt} - 2g_{ti}v^i - g_{ij}v^i v^j}} \equiv \Gamma. \quad (33)$$

In special relativity, the gamma factor is just  $\Gamma = 1/\sqrt{1-v^2}$ . We can check that this is what we get from Eq. (33) for the Schwarzschild metric of Eq. (22) when we take the limit of no gravity, i.e.  $G \rightarrow 0$  (or, in our units, the limit  $M_{\text{BH}} \rightarrow 0$ ).

Going back to the study of Schwarzschild geodesics, let us now focus on bound orbits, since they are the ones we are interested in. By definition the radial coordinate for these orbits must lie inside a finite interval,  $[r_p, r_a]$ , where  $r_p$  is the pericenter radial coordinate and  $r_a$  is the apocenter one. This means that for these particular values of  $r$ ,  $dr/d\tau$  must vanish. If we look at Eq. (29) we realize this can only happen if  $\mathcal{E}^2 \leq 1$ . Assuming  $\mathcal{E} > 0$  (negative values corresponds to the time-reverse orbits), this means  $0 \leq \mathcal{E} \leq 1$ . More in detail, Eq. (29) can be rewritten as follows:

$$\left(\frac{dr}{d\tau}\right)^2 = \frac{1}{r^3} (1 - \mathcal{E}^2) (r_a - r) (r - r_p) (r - r_o), \quad (34)$$

only valid for bound geodesics. Here,  $r_o$  is a third root that satisfies:  $r_a > r_p > r_o$ , and hence it will not be reached during the motion. By comparing this with Eq. (29) we can obtain  $(r_p, r_a, r_o)$ ,

$$r_p + r_a + r_o = \frac{2M_{\text{BH}}}{1 - \mathcal{E}^2}, \quad (35)$$

$$r_p r_a + r_o(r_p + r_a) = \frac{\mathcal{J}^2}{1 - \mathcal{E}^2}, \quad (36)$$

$$r_p r_a r_o = \frac{2M_{\text{BH}} \mathcal{J}^2}{1 - \mathcal{E}^2}. \quad (37)$$

In order to solve them, we can introduce the eccentricity and dimensionless semilatus rectum orbital parameters,  $(e, p)$ , in the usual way<sup>4</sup>

$$r_p = \frac{pM_{\text{BH}}}{1+e}, \quad r_a = \frac{pM_{\text{BH}}}{1-e} \quad \Longleftrightarrow \quad p = \frac{2r_p r_a}{M_{\text{BH}}(r_p + r_a)}, \quad e = \frac{r_a - r_p}{r_a + r_p}. \quad (38)$$

Then, we can first find the expressions of  $(\mathcal{E}, \mathcal{J})$  and  $r_o$  in terms only of  $(e, p)$  and the black hole mass:

<sup>4</sup> The general rule to recover proper units is to make the substitution:  $M_{\text{BH}} \rightarrow GM_{\text{BH}}/c^2$ .



$$r_o = \frac{2pM_{\text{BH}}}{p-4}, \quad (39)$$

$$\mathcal{E}^2 = \frac{(p-2+2e)(p-2-2e)}{p(p-3-e^2)}, \quad (40)$$

$$\mathcal{J}^2 = \frac{p^2 M_{\text{BH}}^2}{p-3-e^2}. \quad (41)$$

An interesting relation comes out by imposing that  $r_o < r_p$  as we have assumed at the beginning:

$$p-6-2e > 0, \quad (42)$$

which is a separatrix between stable and unstable bound orbits.

In practice, in order to numerically integrate the equations of motion for bound orbits we have to take into account that  $r$  is not a good coordinate to use due to the existence of turning points. In order to avoid the numerical problems derived from this, it is very convenient to introduce the following alternative angular variable:

$$r = \frac{pM_{\text{BH}}}{1+e\cos\psi}, \quad (43)$$

The orbital motion, in terms of the variables  $(t, \psi, \varphi)$  is described by the following set of ODEs

$$\frac{d\psi}{dt} = \frac{(1+e\cos\psi)^2}{p^2 M_{\text{BH}}} \frac{(p-2-2e\cos\psi)\sqrt{p-6-2e\cos\psi}}{\sqrt{(p-2)^2-4e^2}}, \quad (44)$$

$$\frac{d\varphi}{dt} = \frac{(1+e\cos\psi)^2}{p^{3/2} M_{\text{BH}}} \frac{(p-2-2e\cos\psi)}{\sqrt{(p-2)^2-4e^2}}. \quad (45)$$

### Relativistic precession

In Keplerian motion, the time that a particle take to go from  $r_p$  to  $r_a$  and back to  $r_p$  (the radial period) is exactly the same as the time it takes to go  $2\pi$  around the central object, that is, to cover a  $\varphi$ -period. In General Relativity, this is not the case, and in the case of a non-spinning black hole these two periods do not coincide. The consequences of this is that the orbit does not close itself and there is precession of the pericenter (it is not located in the same position with respect to Cartesian coordinates associated with  $(r, \varphi)$ , i.e.  $(x, y) = (r\cos\varphi, r\sin\varphi)$ ).

Using the equations of motion given in Eqs. (44) and (45), the amount of angle  $\varphi$  covered during one single radial period is given by

$$\Delta\varphi = 2 \int_{t_p}^{t_a} \frac{d\varphi}{dt} dt, \quad (46)$$

where  $t_p$  and  $t_p$  indicate the coordinate time corresponding to the apocenter and pericenter locations. We can rewrite this integral in terms of  $\psi$  to get

$$\Delta\varphi = 2 \int_0^\pi \frac{d\varphi}{d\psi} d\psi = 2p^{1/2} \int_0^\pi \frac{d\psi}{\sqrt{p-6-2e\cos\psi}}, \quad (47)$$

and using that  $\cos\psi = -\cos(\pi-\psi) = -1 + 2\sin^2(\pi/2 - \psi/2)$  and defining  $x \equiv (\pi - \psi)/2$  we get

$$\Delta\varphi = \frac{4p^{1/2}}{\sqrt{p-6+2e}} \int_0^{\pi/2} \frac{dx}{\sqrt{1 - \frac{4e}{p-6+2e} \sin^2 x}} = \frac{4p^{1/2}}{\sqrt{p-6+2e}} K\left(\sqrt{\frac{4e}{p-6+2e}}\right), \quad (48)$$

where  $K(k) = \int_0^{\pi/2} d\alpha (1 - k^2 \sin^2 \alpha)^{-1/2}$  is the complete elliptic integral of the first kind. It turns out that this integral diverges as  $p$  approaches  $6+2e$ , that is, when we approach the separatrix of Eq. (42).

### The Kerr case

Now that we have addressed the Schwarzschild case, which is our reference point, we will describe the characteristics that distinguish a Kerr SMBH from it. This is a simple summary focused on the main ideas which are important for the evolution on phase-space that we address later. For a rigorous, detailed review, we refer the reader to the reviews of [177, 172].

The most interesting feature is that, whilst in the Schwarzschild case the geometry is spherically-symmetric, in Kerr it is axisymmetric respect to the spin axis. This translates into the fact that orbits outside the equatorial plane are not planar. There is no such (Keplerian- or Schwarzschild-like) concept in Kerr. As a matter of fact, the concept of “orbit” is not exactly straightforward in the relativistic case if it is not a bound one, and there is no simple way to compare it with the Keplerian concept. In any case, the inclination of the orbit  $\iota$  with respect to the spin axis is fundamental in Kerr and decides the dynamics of the system.

Non-equatorial orbits (which are a special case) precess with a given  $\iota$  at a frequency  $f_\theta$ , with  $\theta$  the polar Boyer-Lindquist coordinate [42, 135]. We can define the inclination for Kerr geodesic orbits in two different ways. One possibility is via Carter’s constant  $Q$ ,

$$\cos \iota = \frac{L_z}{\sqrt{L_z^2 + Q}}, \quad (49)$$

and another with the minimum value of  $\theta$ ,

$$\iota = \text{sign}(L_z) \left[ \frac{\pi}{2} - \theta_{\min} \right], \quad (50)$$

where  $\text{sign}(L_z)$  allows us to distinguish between prograde (positive) and retrograde orbits (negative).

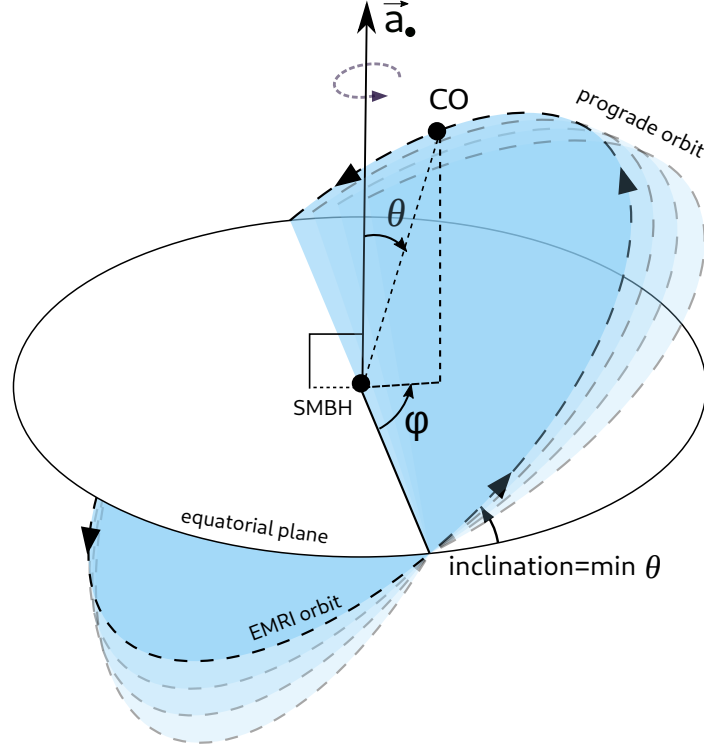


**Fig. 14** The minimum polar angle  $\theta$  from the spin axis is defined as the inclination  $\iota$  of the EMRI. We illustrate this with a prograde orbit of a CO revolving around a SMBH of spin  $a_\bullet$  on a prograde orbit. While  $\theta$  changes significantly, the inclination does not, as we can see in Fig. (19).

In Fig. (14) we depict the orbit of a prograde EMRI revolving around a SMBH of spin  $a_\bullet$ . The minimum value of the polar angle  $\theta$ , determines  $\iota$ . This figure is to be regarded as an illustration of the process to show the effect of radiation reaction. The orbital plane however precesses on a much faster timescale, so that the orbit does not look like depicted for a static observer. In general it fills the volume of a torus. For a more realistic illustration, see e.g. Fig. (4) of [32]. The inclination  $\iota$  must vary as the EMRI approaches more and more the LSO, it is a constant of motion for geodesics, not to be misinterpreted with the instantaneous orbital colatitude  $\theta$  of Boyer-Lindquist coordinates.

As in the Schwarzschild, the periapsis precesses, so that we need to introduce two additional frequencies. One is related to the radial motion and the time to go from periapsis,  $r_{\text{peri}}$ , to apoapsis,  $r_{\text{apo}}$ , and back. The second one is linked to the azimuthal motion around the spin axis and the required time to describe  $2\pi$  around it, i.e. the

time for the azimuthal angle  $\phi$  to increase  $2\pi$  radians. We call these two frequencies  $f_r$  and  $f_\phi$ , respectively. These three fundamental frequencies and their harmonics are responsible to make so rich in information an EMRI, because they allow the CO, the EMRI, to probe the geometry around the SMBH with gravitational radiation, which encodes this cartography of warped spacetime.

The emitted gravitational waves backreact on to the CO itself and lead to a change of its orbital parameters which can be estimated by the energy and angular momentum carried away from the radiation, namely the semi-latus rectum -or alternatively the semi-major axis-, the eccentricity and the inclination of the orbit,  $(p, e, \iota)$ .

The geodesic motion around a Kerr SMBH has three constants of motion, the energy per unit mass  $E$  (which we normalise to  $m_{\text{CO}}$ ),  $L_z$ , and the Carter constant per unit mass square. This last is linked to an extra symmetry of the Kerr geometry, in the same way that some axisymmetric Newtonian potentials display [see e.g. 39, 8]. These three constants are modified due to the emission of gravitational radiation. The work of [157] shows that there is a connection between the constants  $(E, L_z, C)$  and the set of orbital parameters  $(p, e, \iota)$ ; more precisely, there is a (bijective, an injective-surjective) mapping between both sets, which is useful to analyse the evolution of the EMRI without having to explicitly solve the evolution of the orbit. This mapping is however complex and we refer the reader to e.g. the implementation of [163] for a reference.

Again, as a reference, we illustrate this mapping for a simpler case, a Schwarzschild SMBH. It is simpler because  $\iota$  and  $C$  are not required. In this case,

$$\frac{E^2}{c^2} = \frac{(p-2-2e)(p-2+2e)}{p(p-3-e^2)}, \quad (51)$$

$$L_z^2 = \frac{G^2 M_{\text{BH}}^2 p^2}{c^2(p-3-e^2)}. \quad (52)$$

Using the symmetries of the geometry of a Kerr SMBH we can separate the equations for geodesic orbital motion so that the trajectory of a massive body, described in terms of Boyer-Lindquist coordinates  $\{t, r, \theta, \phi\}$ , can be written as follows

$$\rho^2 \frac{dt}{d\tau} = \frac{1}{\Delta} \left( \Sigma^2 \frac{E}{c} - 2a_\bullet r_\bullet \frac{L_z}{c} \right) \quad (53)$$

$$\rho^4 \left( \frac{dr}{d\tau} \right)^2 = \left[ (r^2 + a_\bullet^2) \frac{E}{c} - a_\bullet \frac{L_z}{c} \right]^2 - \left( \frac{Q}{c^2} + r^2 \right) \Delta \equiv R(r) \quad (54)$$

$$\rho^4 \left( \frac{d\theta}{d\tau} \right)^2 = \frac{C}{c^2} - \frac{L_z^2}{c^2} \cot^2 \theta - a_\bullet^2 \left( 1 - \frac{E^2}{c^2} \right) \cos^2 \theta \quad (55)$$

$$\rho^2 \frac{d\phi}{d\tau} = \frac{1}{\Delta} \left[ 2a_\bullet r_\bullet \frac{E}{c} r + \frac{L_z}{c} \frac{\Delta - a_\bullet^2 \sin^2 \theta}{\sin^2 \theta} \right]. \quad (56)$$

Where we have defined the gravitational radius  $r_\bullet \equiv GM_\bullet/c^2$ ,  $Q \equiv C + (L_z - a_\bullet E)^2$ ,  $\rho^2 \equiv r^2 + a_\bullet^2 \cos^2 \theta$  and  $\Delta \equiv r^2 - 2r_\bullet r + a_\bullet^2 = r^2 f + a_\bullet^2$ , with  $f \equiv 1 - 2r_\bullet/r$ , and  $\Sigma^2 \equiv (r^2 + a_\bullet^2)^2 - a_\bullet^2 \Delta \sin^2 \theta$ . In this set of equations, Eq. (53) gives us the link between the change of coordinate time  $t$ , the time of observers at infinity, and the proper time  $\tau$ , while Eqs. (54), (55) and (56) give us the link for the spatial trajectory. This set can be combined to derive the spatial trajectory in terms of coordinate time  $t$ ,  $(r(t), \theta(t), \phi(t))$ .

### Evolution in phase-space

We can analyse the evolution of the radiation emitted by an EMRI thanks to the approximation of Keplerian ellipses of [142]. In this approximation, the orbital parameters change slowly because of GWs, which are emitted at every integer multiple of the orbital frequency,  $\omega_n = n \sqrt{GM_{\text{BH}}/a^3}$ . At a given distance  $D$ , the strain amplitude in the  $n$ -th harmonic is

$$h_n = g(n, e) \frac{G^2 M_{\text{BH}} m_{\text{BH}}}{D a c^4} \quad (57)$$

$$\simeq 1.6 \times 10^{-22} g(n, e) \left( \frac{D}{1 \text{ Gpc}} \right)^{-1} \left( \frac{a}{10^{-2} \text{ pc}} \right)^{-1} \left( \frac{M_{\text{BH}}}{4 \times 10^4 M_\odot} \right) \left( \frac{m_{\text{BH}}}{10 M_\odot} \right). \quad (58)$$

In this expression  $g(n, e)$  is a function of the harmonic number  $n$  and the eccentricity  $e$  [see 142]. We consider the RMS amplitude averaged over the two GW polarizations and all directions. Whilst there are more accurate descriptions of the very few last orbits, as e.g. [143, 83, 30, 73], the scheme of [142] yields a qualitatively correct estimation of the frequency cutoff at the innermost stable circular orbit.

In Fig. (15) we show the first ten harmonics in the plane of characteristic amplitude as a function of the frequency. We can see that at detector “entrance” the source is already quite circular, even if the initial eccentricity was set to what we expect from a relaxation EMRI. This is why the second harmonic dominates over the rest of them. Even if initially the periapsis distance was of  $R_p^0 = 26.1 R_S$ ,  $10^4$  yrs before the plunge (i.e. crossing the event horizon of the SMBH), the EMRI has an eccentricity of  $e = 0.547$  and a periapsis distance of  $R_p = 21.2 R_S$ . This depicts quite clearly the slow shrinkage and circularization of EMRIs. Ten years before the plunge, we have that  $e = 1.97 \times 10^{-2}$ , with  $R_p = 3.77 R_S$ , and nine years later,  $e = 1.44 \times 10^{-2}$ , with  $R_p = 3.11 R_S$ . This means that the CO, a stellar-mass black hole in this case, is at the verge of falling on to the SMBH but for a small epsilon, and this distance becomes smaller by extremely amounts over a timescale of 9 years. This translates into a very large number of strong bursts from a coherent source at the verge of the abyss, being transported to us in an almost unperturbed way and carrying informa-

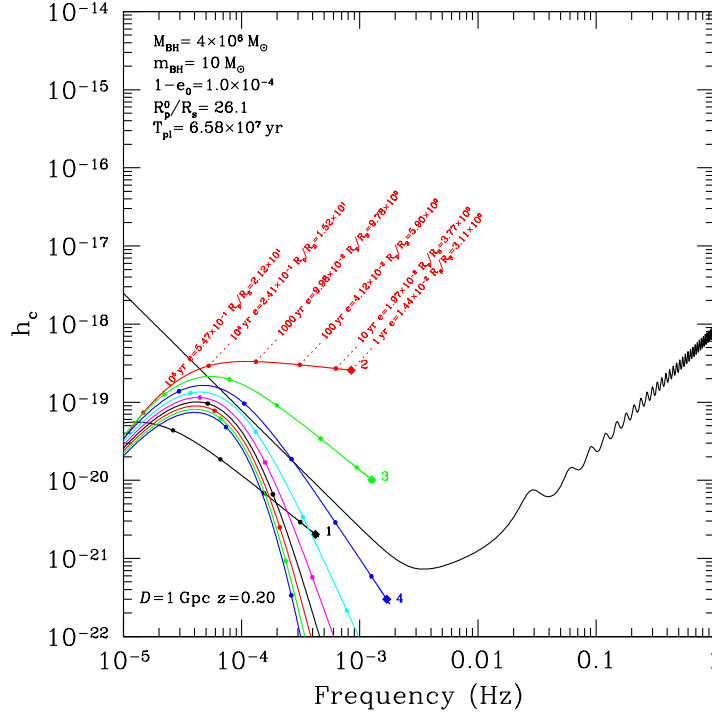


**Fig. 15** Cascade of the first 10 harmonics in the approximation of [141]. The Y-axis shows the characteristic, dimensionless amplitude (how much the length of the arms of the detector changes divided by the length) as a function of the frequency in Hz. The CO has been set on an orbit whose dynamical parameters are summarised on the top, left corner, with  $e_0$  the initial eccentricity,  $R_p^0$  the initial periastron distance, and  $T_{pl}$  corresponds to the associated timescale  $T_{GW}$  as described in Eq. (15). We have adopted values corresponding to a relaxation EMRI, as in Fig. (12). The upper, red curve corresponds to the second harmonic, which is dominant in this case because, although the CO initially has a large eccentricity, it has circularised. Different points on this curve display information about the system as it evolves with time. The diamond corresponds to one year before the plunge on to the SMBH.

tion about spacetime from a region inaccessible to the photon. Moreover, since the CO is changing the plane of the orbit (for a Kerr SMBH), shrinking the semi-major axis and precessing, we are de facto gathering a cartography of warped spacetime.

We now give a few examples for the dynamical parameters of relaxation EMRIs as well as their polarizations. We follow the “numerical kludge scheme”, which conceptually computes the trajectory of the CO using Boyer-Lindquist coordinates [42], to then identify them with flat-space spherical polar ones. This allows us to then derive the waveform from the multipole moments in the context of linearised gravitational perturbation theory in flat spacetime. This waveform is computed with a slow-motion quadrupole formula, a quadrupole/octupole formula, and the weak-field approach for fast-motion of [147]. This scheme has evolved over the years and

has been significantly improved, see [30, 23, 54, 55]. For the particular calculations we have done, we have used the “EMRI Kludge Suite” of [54, 55].

Fig. (16) corresponds to the evolution of the eccentricity for an EMRI with characteristics similar to those of Fig. (15), at detector entrance, when the eccentricity is of about  $e \simeq 10^{-2}$ . In Fig. (17) we show the same but for a system of a much lower eccentricity, so that the separatrix is located very close to the minimum value of the semi-latus rectum of a Schwarzschild black hole,  $p = 6 + 2e$ .

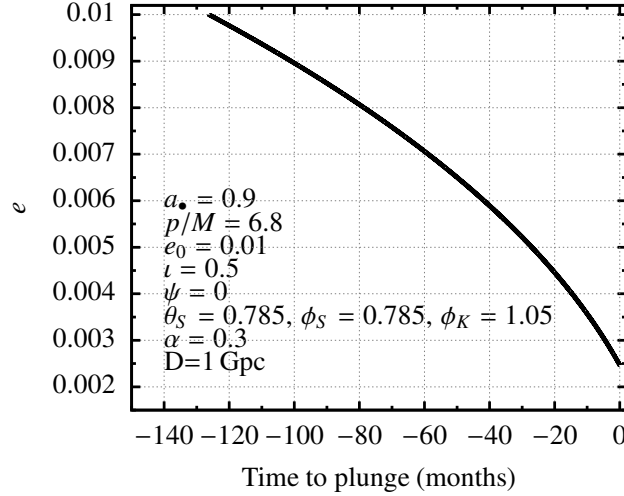


**Fig. 16** Eccentricity evolution as a function of time to plunge in months. The labels correspond (from the top to the bottom, left to right) to the initial values of the semi-latus rectum  $p/M$ , the spin of the SMBH  $a_*$ , the inclination  $i$ , the true anomaly  $\psi$ , the source polar angle  $\theta_S$ , the azimuthal angle  $\phi_S$ , the SMBH spin azimuthal angle  $\phi_K$  (all of them in ecliptic coordinates), the azimuthal orientation  $\alpha$ , as defined in Eq (18) of [30], and the distance to the source  $D$ . Note that we do not see an increase in the eccentricity as in Fig. (17) because the separatrix for  $a_* = 0.9$  located at a different minimum value of the semi-latus rectum  $p$ .

In Fig. (18) we depict the evolution of the energy  $E$  of the same system as a function of time. We normalise to the initial value of the energy when the system still has 126.23 months ( $\sim 10.5$  yrs) to go before the plunge.

In Fig. (19) we show the evolution of the inclination for the same system. At this point, it is important to note that when we say inclination we are not referring to the polar angle, but to the maximum value reached by the polar angle with respect to the equatorial plane of the orbit if the SMBH was Schwarzschild (or if the direction of the spin was perfectly aligned with the z-component of the angular momentum of the orbital plane,  $L_z$ ).

Because the minimum value of  $\theta$ , i.e. the inclination  $i$ , see Fig. (14), changes very slowly [see e.g. Fig. 2 of 84], it has been assumed to be fixed by the kludge models in the past, as e.g. in the Teukolsky approach of Fig. 2 of [103]. In that figure the dashed line is the location of the innermost stable spherical orbit. We can see that



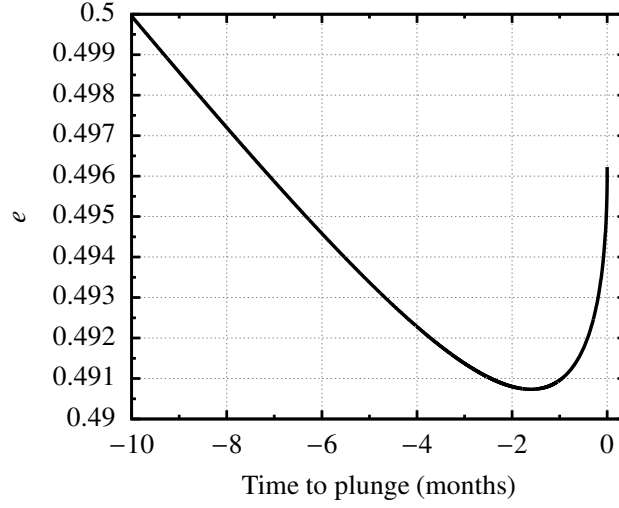


**Fig. 17** Evolution of the eccentricity of an EMRI displaying the increase in the last orbits for a SMBH of mass  $M_{\text{BH}} = 4 \times 10^6 M_{\odot}$ , of spin  $a_{\bullet} = 0.2$ , and a CO which initially had  $e_0 = 0.5$ . The rest of the parameters are identical to those of Fig. (16).

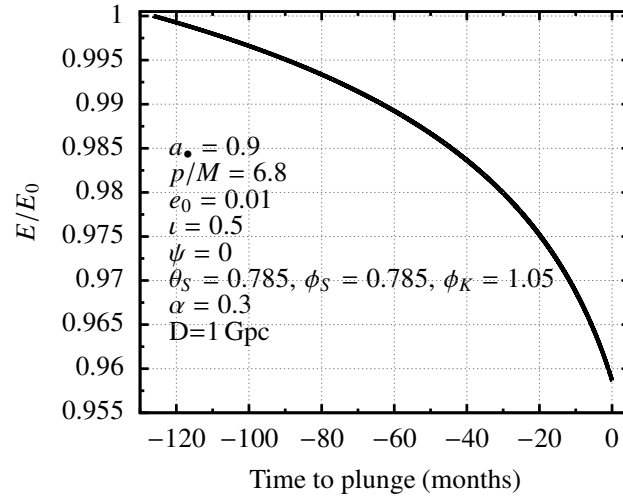


**Fig. 18** Evolution of the energy of the EMRI normalised to the initial energy at the beginning of the integration. This system corresponds to the one described in Fig. (16).

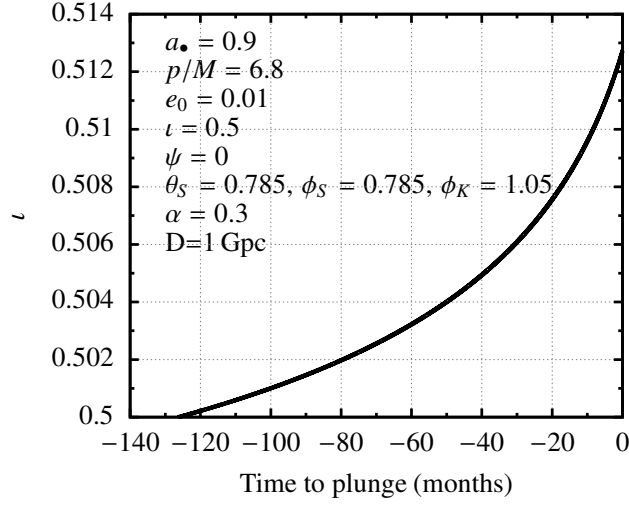


**Fig. 19** Same as Fig. (16) but for the evolution of the inclination.

the secondary explores the maximum and the corresponding minimum value during every period.

In Fig. (20) we show the evolution of the polarizations only for the few last hours because otherwise the figure is too crowded. The system corresponds to the same one as in the rest of the previous figures.

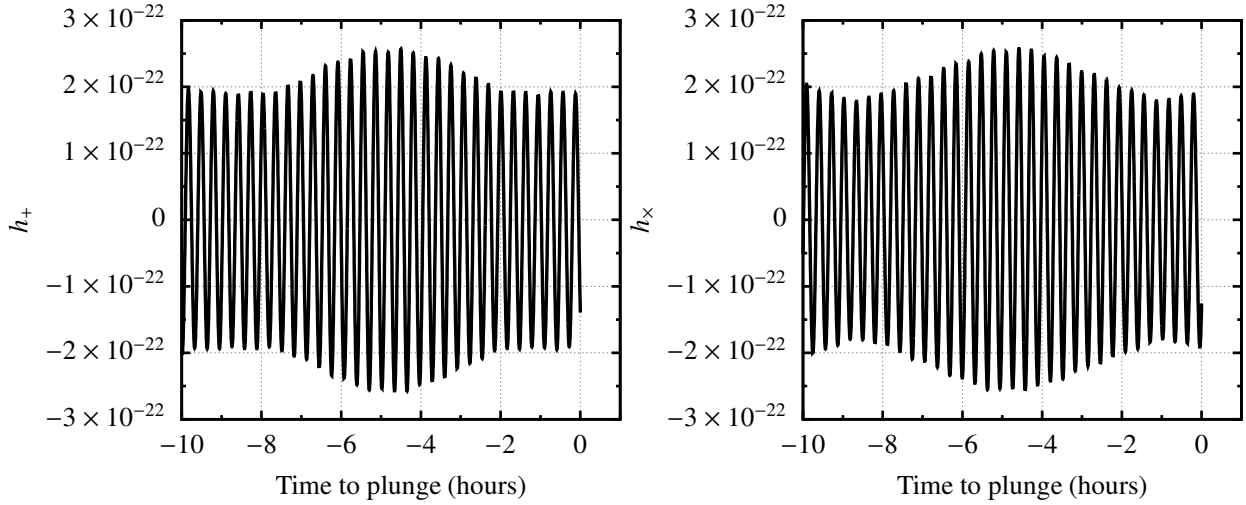


**Fig. 20** The two waveform polarizations  $h_+$  (left panel) and  $h_x$  (right panel) as a function of time to merger. The system correspond to that of Fig. (16).

### *Accumulated phase shift*

We have seen that there are different mechanisms to form EMRIs. In this chapter we are focusing only on relaxation EMRIs and those formed via tidal separation of binaries. These, but also other scenarios, leave a fingerprint in the dynamical parameters of the EMRIs when it enters the LISA band that allows us to reverse-engineer the properties of the host environment, which is interesting from a point of view of astrophysics. The same applies to IMRIs, as we will discuss later.

In particular, we can look at the impact on how the phase shifts due to any residual eccentricity that the source might have. As an example, we have seen that relaxation EMRIs will typically have higher eccentricities as those produced via the tidal separation of a binary. This eccentricity will induce a difference in the phase evolution of the signal as compared to a circular source.

We can estimate the accumulated phase shift to lowest post-Newtonian order and to first order in  $e^2$  (via the derivation of [110] of the phase correction),

$$\Delta\Psi_e(f) = \Psi_{\text{last}} - \Psi_i \cong -\Psi_i = \frac{7065}{187136} e_i^2 (\pi f M_z)^{-5/3}. \quad (59)$$

Here  $e_i$  represents the eccentricity at the frequency of the dominant harmonic when it enters the detector, we have introduced the quantity

$$M_z := \frac{G(1+z)}{c^3} \frac{(M_{\text{BH}} m_{\text{CO}})^{3/5}}{(M_{\text{BH}} + m_{\text{CO}})^{1/5}}, \quad (60)$$

and  $f$  is the frequency for the  $n = 2$  harmonic. We have furthermore assumed that

$$\Delta\Psi_e(f) = \Psi_{\text{last}} - \Psi_i \simeq -\Psi_i, \quad (61)$$

with  $\Psi_{\text{last}}$  and  $\Psi_i$  the final and initial phase. As shown in section B.2 of [59],  $\Psi_e(f)$  has a pronounced fall-off with increasing frequency. Hence, to derive the accumulated phase shift in terms of  $f$  and the remaining time to merger, we now recall from [104] that the semi-major axis of the binary is

$$a^3 = \frac{G(M_{\text{BH}} + m_{\text{CO}})}{(\pi f)^2}, \quad (62)$$

so that we can derive the accumulated phase shift in terms of  $f$  and the remaining time to merger, because this last quantity is given by [141]

$$T_{\text{mrg}} \cong \frac{5}{256} \frac{c^5}{G^3 M_{\text{BH}} m_{\text{CO}} (M_{\text{BH}} + m_{\text{CO}})} \left[ \frac{G(M_{\text{BH}} + m_{\text{CO}})}{(\pi f)^2} \right]^{4/3}, \quad (63)$$

and we will elaborate on this in the section about the rates. From the same reference, relation 5.12, assuming  $1/(1 - e^2) \simeq 1$  and Eq. (62), we have that  $e^2 f^{19/9} \cong \text{constant}$ , which means that  $a \propto f^{-2/3}$ . Hence, from Eq. (63) and Eq. (62),

$$\pi f \cong \left(\frac{5}{256}\right)^{3/8} M_z^{-5/8} T_{\text{mrg}}^{-3/8}, \quad (64)$$

so that the accumulated phase shift is

$$\begin{aligned} \Delta\Psi_e(f) &= \left(\frac{5}{256}\right)^{-17/12} \frac{7065}{187136} (\pi f_i)^{19/9} e_i^2 M_z^{25/36} T_{\text{mrg}}^{17/12} \\ &\cong 10 (\pi f_i)^{19/9} e_i^2 M_z^{25/36} T_{\text{mrg}}^{17/12}, \end{aligned} \quad (65)$$

and is detectable if  $\gtrsim \pi$ .

### *Event rate of relaxation EMRIs*

In this section, and as mentioned in the introduction, we will focus on relaxation as the mechanism for producing EMRIs. To derive the event rate, we have to solve the following integral,

$$\dot{\Gamma}_{\text{CO}} \simeq \int_{a_{\text{min}}}^{a_{\text{crit}}} \frac{dn_{\text{CO}}(a)}{T_{\text{rlx}}(a) \ln(\theta_{\text{lc}}^{-2})}. \quad (66)$$

where the loss-cone angle can be estimated to be  $\theta_{\text{lc}} \simeq (J_{\text{max}}/J_{\text{lc}})^{-1}$ , as can be derived from the previous discussion, and see [18] for more details. Following [5]  $\theta_{\text{lc}}^2 \simeq \sqrt{8R_S/a}$ . The numerator is given by [see 19]

$$dn_{\text{CO}}(a) = f_{\text{sub}}^{\text{CO}} (3 - \beta) \frac{N_{\text{inflMS}}^{\text{CO}}}{r_{\text{infl}}} \left(\frac{a}{r_{\text{infl}}}\right)^{2-\beta} da. \quad (67)$$

with  $f_{\text{sub}}^{\text{CO}}$  the fraction of the type of CO in consideration in the stellar system (e.g. for stellar-mass black holes  $\sim 10^{-3}$ ) and  $N_{\text{inflMS}}^{\text{CO}}$  the total number of objects (main-sequence stars and COs, or brown-dwarfs) within  $r_{\text{infl}}$ .

The lower limit in the integral can be estimated by calculating the radius within which we expect to have at least one CO of the type we are considering. Since  $N_{\text{inflMS}}^{\text{CO}} = M_{\text{BH}}/\bar{m}_*$ , with  $\bar{m}_*$  the average stellar mass, we have that  $a_{\text{min}} \simeq 1.65 \times 10^{-5} \text{ pc } f_{\text{CO,sub}}^\beta [r_{\text{infl}}/(1 \text{ pc})]$ , with  $f_{\text{CO,sub}}$  the the fraction of CO taken into consideration. With these values, we can solve analytically Eq. (66), which yields

$$\dot{\Gamma}_{\text{CO}} = \frac{3 - \beta}{2\lambda} \frac{N_{\text{inflMS}}^{\text{CO}}}{T_0 r_{\text{infl}}^\lambda} f_{\text{sub}}^{\text{CO}} \left\{ a_{\text{crit}}^\lambda \left[ \ln(a_{\text{crit}}/8R_S) - \frac{1}{\lambda} \right] - a_{\text{min}}^\lambda \left[ \ln(a_{\text{min}}/8R_S) - \frac{1}{\lambda} \right] \right\}, \quad (68)$$

where we have introduced [19]

$$T_0 \simeq \frac{4.26}{(3-\gamma)(1+\gamma)^{3/2}} \frac{\sqrt{r_{\text{infl}}^3 (GM_{\text{BH}})^{-1}}}{\ln(\Lambda) N_{\text{bh}}} \left( \frac{M_{\text{BH}}}{m_{\text{bh}}} \right)^2. \quad (69)$$

These equations are not easy to interpret in terms of rates, so that we will give now investigate Eq. (68) for the standard EMRI scenario, i.e. we choose the CO to be a stellar-mass black hole with a mass of  $10M_\odot$ . As for the power indeces, we address two possibilities. One is a classical solution, the so-called Bahcall-Wolf result [BW, 26]. We remark, however, that their results for two-mass components (the stellar-mass black holes and the main-sequence stars, all with the same type of mass,  $1M_\odot$ ) are heuristically derived from their earlier work of [25]. In their paper they derive  $\gamma = 7/4$  and  $\beta \rightarrow 3/2$ . This result of is based only on the mass ratio of the two populations and assumes that stellar-mass black holes have a fraction as high as 50% of all stars. A physically realistic solution of the problem must require that stellar-mass black holes have a fraction at most of  $10^{-3}$  of all stars, as derived from a standard IMF. When using this occupation fraction, [4] and [148, 9] found that diffusion is more efficient and  $\gamma = 2$  and  $\beta = 3/4$ . We shall call this solution the strong-mass segregation result (SM). For legibility reasons, we introduce the quantities  $\hat{\Lambda} := \ln(\Lambda)/13$ ,  $\hat{N}_{\text{infl}} := N_{\text{infl}}/12 \times 10^3$ ,  $\hat{r}_{\text{infl}} := r_{\text{infl}}/(1\text{pc})$  and  $\hat{m}_{\text{bh}} := m_{\text{bh}}/(10M_\odot)$ .

With these definitions, we derive that for the (mathematically correct but physically unrealistic) Bahcall & Wolf solution,

$$\begin{aligned} \dot{\Gamma}_{\text{BW,bh}} &\sim 2.63 \times 10^{-6} \text{ yrs}^{-1} \hat{N}_{\text{infl}} \hat{\Lambda} \hat{r}_{\text{infl}}^{-5/2} \hat{m}_{\text{bh}}^2 \times \\ &\quad \left\{ 5 \times 10^{-2} \hat{r}_{\text{infl}} \hat{N}_{\text{infl}}^{-4/5} \hat{\Lambda}^{-4/5} \hat{m}_{\text{bh}}^{4/5} \mathcal{W}(\theta, \mathbf{a}_\bullet)^{-2} \times \right. \\ &\quad \left[ \ln \left( 16318 \hat{r}_{\text{infl}} \hat{N}_{\text{infl}}^{-4/5} \hat{\Lambda}^{-4/5} \hat{m}_{\text{bh}}^{4/5} \mathcal{W}(\theta, \mathbf{a}_\bullet)^{-2} \right) - 1 \right] \times \\ &\quad \left. 2 \times 10^{-3} \hat{r}_{\text{infl}} \times [\ln(618 \hat{r}_{\text{infl}}) - 1] \right\}. \end{aligned} \quad (70)$$

Setting  $\hat{m}_{\text{bh}} = 1$  and all of the other quantities with a hat to unity as well,  $\dot{\Gamma}_{\text{BW,bh}} \sim 10^{-6} \text{ yr}^{-1}$ , which is the usual solution [see 7]. As for the strong mass segregation result, which *does* represent correctly the segregation in a galactic nucleus,

$$\begin{aligned}
\dot{\Gamma}_{\text{SM,bh}} \sim & 1.92 \times 10^{-6} \text{ yrs}^{-1} \hat{N}_{\text{infl}} \hat{\Lambda} \hat{r}_{\text{infl}}^{-2} \hat{m}_{\text{bh}}^2 \times \\
& \left\{ 1.6 \times 10^{-1} \hat{r}_{\text{infl}}^{1/2} \hat{N}_{\text{infl}}^{-1/2} \hat{\Lambda}^{-1/2} \hat{m}_{\text{bh}}^{1/2} \mathcal{W}(\theta, \mathbf{a}_\bullet)^{-5/4} \times \right. \\
& \left[ \ln \left( 9138 \hat{r}_{\text{infl}} \hat{N}_{\text{infl}}^{-1} \hat{\Lambda}^{-1} \hat{m}_{\text{bh}} \mathcal{W}(\theta, \mathbf{a}_\bullet)^{-5/2} \right) - 2 \right] - \\
& \left. 4 \times 10^{-2} \hat{r}_{\text{infl}}^{1/2} \times [\ln(618 \hat{r}_{\text{infl}}) - 2] \right\}, \tag{71}
\end{aligned}$$

which is then  $\dot{\Gamma}_{\text{SM,bh}} \sim 2 \times 10^{-6} \text{ yr}^{-1}$ . Note that for both results we have adopted a Schwarzschild solution, which means that we have set  $\mathcal{W}(\theta, \mathbf{a}_\bullet) = 1$ . The rates for a Kerr SMBH will have a multiplying factor that depends on the inclination of the orbit and spin of the SMBH. A detailed analysis of (i) the relativistic evolution in phase-space and (ii) the rates depending on the mass species and distribution is in preparation and will be submitted elsewhere (Amaro Seoane & Sopuerta in preparation).

It is important to note that these results are subject to be revisited, since recently [183] derived an improved timescale  $T_{\text{GW}}$  which differs from the results of [141] because it includes the effects of the first-order post-Newtonian perturbation and additionally provides a simple fit to account for the Newtonian self-consistent evolution of the eccentricity. These improvements can be captured via relatively trivial modifications to the usual timescale, which must be multiplied by two factors,

$$\begin{aligned}
R(e_0) &= 8^{1-\sqrt{1-e_0}} \\
Q_{\text{f}}(p_0) &= \exp\left(\frac{2.5R_{\text{S}}}{p_0}\right), \tag{72}
\end{aligned}$$

where  $e_0$  is the initial eccentricity and  $p_0 = a_0(1 - e_0)$  the periapsis. The final corrected expression for the GW-induced decay of two orbiting bodies  $M_{\text{BH}}$  and  $m_{\text{CO}}$ , is

$$T_{\text{GW}} = \frac{24 \sqrt{2}}{85} \frac{c^4 a^5 (1-e)^{7/2}}{G^3 m_{\text{CO}} M_{\text{BH}}} 8^{1-\sqrt{1-e_0}} \exp\left(\frac{2.5R_{\text{S}}}{p_0}\right), \tag{73}$$

as derived in [183]. Since we are modifying  $T_{\text{GW}}$ , this will be propagated into the rates, as we can see from Eq. (13). For high eccentricity orbits and spin, the correction factors are (Zwick et al to be submitted 2020)

$$\begin{aligned}
R(e_0) &= 8^{\sqrt{1-e_0}} \\
Q_{\text{h}} Q_{\text{s}} &\rightarrow \exp\left(\frac{2.8R_{\text{S}}}{p_0} + s_1 \left(\frac{0.3R_{\text{S}}}{p_0}\right) + |s_1|^{3/2} \left(\frac{1.1R_{\text{S}}}{p_0}\right)^{5/2}\right) \tag{74}
\end{aligned}$$

And accordingly, the corrected timescale is

$$T_{\text{GW}} = \frac{24\sqrt{2}}{85} \frac{c^4 a^5 (1-e)^{7/2}}{G^3 m_{\text{BD}} M_{\text{BH}}} 8^{1-\sqrt{1-e_0}} \times \exp \left[ \frac{2.8R_S}{p_0} + s_1 \left( \frac{0.3R_S}{p_0} \right) + |s_1|^{3/2} \left( \frac{1.1R_S}{p_0} \right)^{5/2} \right], \quad (75)$$

where  $s_1$  is a spin parameter defined as  $s_1 := s \cos \theta$ , with  $s$  the magnitude of the spin and  $\theta$  the angle between the SMBH spin vector and the angular momentum vector of the orbit. The detailed derivation of this result will be presented soon as Zwick et al. 2020 and the impact on the event rates as Vázquez et al 2020. We see that when we take into account both corrections, namely the first-order post-Newtonian perturbation with a self-consistent evolution recipe for the evolution of the eccentricity and the spin effects on that timescale (additionally to the location of the LSO, via the  $\mathcal{W}(\theta, a_\bullet)$  function), the results do not differ significantly from the location of  $a_{\text{crit}}$  in Eq. (17).

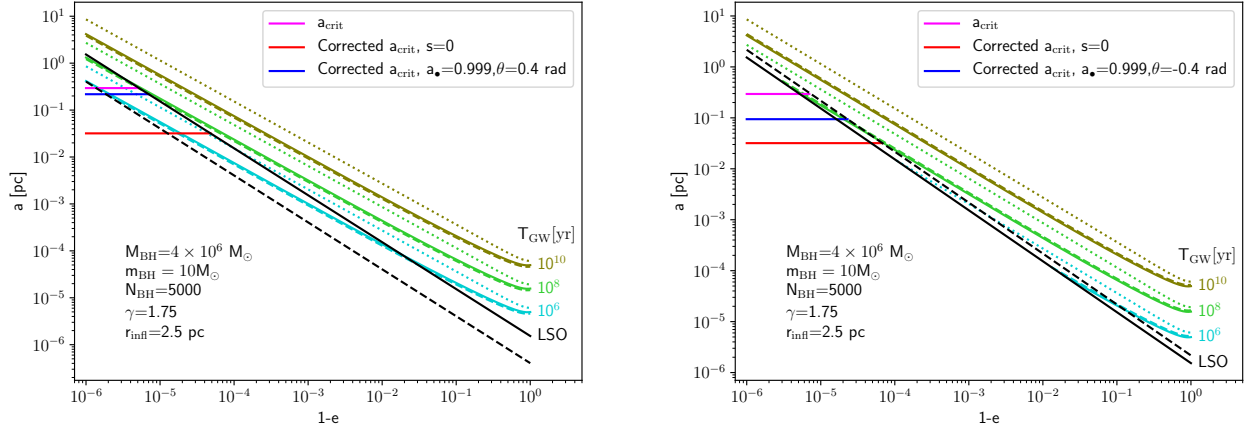


**Fig. 21** Derivation of  $a_{\text{crit}}$  as in Eq. (17) and in Fig. (12) with the modified  $T_{\text{GW}}$ , which takes into account both the effects of the first-order post-Newtonian perturbation with a simple fit to account for the Newtonian self-consistent evolution of the eccentricity, and the effect of the spin as well. Note that the correction for the spin is a different one as the location of the LSO via the  $\mathcal{W}(\theta, a_\bullet)$  function presented in Fig. (11), although we do use this function as well (for details, see the upcoming work of Zwick et al 2020 and Vázquez et al 2020). The left panel corresponds to prograde orbits and the right panel to retrograde ones.

## Intermediate-mass ratio inspirals

### *Intermediate-mass black holes*

For an IMRI to exist, we first have to introduce what intermediate-mass black holes are, what motivates this search and how many of these have been detected. On the one hand, for a long time we know that stellar-mass black holes must be present thanks to electromagnetic observations. Ground-based gravitational wave observatories have opened up a new window and have corroborated this.

On the other hand, the understanding of galactic nuclei (the inner-most cores of galaxies) has advanced rapidly during the past decade, not least due to major advances in high angular resolution instrumentation at a variety of wavelengths. As we have previously mentioned, the overwhelming evidence is that supermassive black holes (with masses between a million and ten thousand million Suns), occupy the centers of most galaxies for which such observations can be made.

Moreover, an intimate link exists between the central supermassive black hole and its host galaxy [107], as exemplified by the discovery of correlations between the mass of the supermassive black hole and global properties of the surrounding stellar system, e.g. the velocity dispersion  $\sigma$  of the spheroid of the galaxy. Despite much progress in recent decades, many fundamental questions about these relations remain open.

These two flavors of black holes have masses that differ by up to nine orders of magnitude. The same way humans grow from babies to teenagers and, later, to adults, black holes must also exist in the intermediate regime. Such “teenager”, intermediate-mass black holes (IMBHs) must have masses typically ranging between  $\sim 10^2 - 10^4 M_\odot$ , and in fact we have detected high X-ray luminosities not coincident with the nucleus of the host galaxy, which translate into these masses under the assumption that they are black holes. Theoretically, we know that IMBHs form and are located at the center of dense stellar systems such as globular clusters, young clusters, or the cores of dwarf galaxies, and indeed this is what the correlations we mentioned before predict [see 75, 77], and the reviews of [133, 124].

IMBHs are key to understand how supermassive black holes gained their titanic masses from stellar-mass black holes, but they are elusive and we do not have any conclusive evidence of their existence in X-rays or radio, although they should accrete matter. For decades, in spite of the effort with electromagnetic radiation, we lacked an evidence of their existence. Recently this has changed, thanks to the observation of GW190521, a gravitational wave signal resulting from the merger of two progenitor black holes of  $85 M_\odot$  and  $66 M_\odot$ , resulting into an IMBH of mass  $142 M_\odot$  [118], which means that a total of  $9 M_\odot$  were completely transformed into energy in the form of gravitational waves [120].

These massive black holes must be lurking in star clusters, as we explained before. These clusters are complicated and interesting, not least because they allow us to probe the event horizon. They are, however, key to understand IMBHs but difficult to simulate due to the many orders of magnitude we have to overcome.



If we want to observe IMBHs with light in globular clusters, we need ultra-precise astronomy, because the influence radius of an IMBH of mass  $10^4 M_\odot$ ,  $r_h \sim 5''$ , assuming a central velocity dispersion of  $\sigma = 20 \text{ km s}^{-1}$  and a distance of  $\sim 5 \text{ kpc}$ . Within that radius we only have a few stars. At such a distance and assuming an observational timescale of 10 yrs, with adaptive optics we could in the best of the cases have a couple of measurements of velocities. The sensitivity limits correspond to a K-band magnitude of  $\sim 15$ , like the kind of stars that we observe in our own Galactic Centre, at 8 kpc and of type B- MS. To derive the influence of the mass of the IMBH on the stellar population around it, as it has been done in our Galactic Centre with SgrA\*, one needs instruments such as the VSI or GRAVITY [82, 67]. Until the recent discovery of the LIGO/Virgo team, IMBHs were simply a logical conjecture which has now been corroborated.

### *Wandering of IMBHs*

It is relatively simple to estimate in an analytical way how far away an IMBH can wander off the centre due to Brownian motion. For simplicity, we assume that the stellar cluster is described by a so-called eta model [63, 176] with enclosed stellar mass

$$M_*(r) = M_{\text{tot}} \left( \frac{r/R_{\text{cut}}}{1 + r/R_{\text{cut}}} \right)^\eta, \quad (76)$$

where  $M_{\text{tot}}$  is the total mass in stars and  $R_{\text{cut}}$  the cut-off radius. For  $r \ll R_{\text{cut}}$ , we have the usual power-law distribution  $\rho \propto r^{-\gamma}$  with  $\gamma = 3 - \eta$ . The massive black hole will wander within a given radius  $R_w$ , where it can capture COs by perturbing stellar orbits (i.e. dynamically) for light enough IMBHs. We simplify the problem by assuming a constant stellar density, so that the gravitational potential in which the IMBH is located can be described as a harmonic oscillator, with angular frequency  $\omega = \sqrt{GM_*(R_w)/R_w^3}$ . Given an equilibrium point, the maximum speed  $V_{\text{osc}}$  achieved by the oscillator for an amplitude (the maximum displacement from the equilibrium position)  $R_{\text{osc}}$  is  $V_{\text{osc}}^2 = \omega^2 R_{\text{osc}}^2$ . This value, commonly referred to as the root mean square amplitude of the oscillations in velocity, is linked to its equivalent in space,

$$V_{\text{osc}}^2 = \omega^2 R_{\text{osc}}^2 \approx \omega R_w^2 = \frac{GM_*(R_w)}{R_w}. \quad (77)$$

Assuming equipartition of kinetic energy between the IMBH and the stellar component, we have that [see 64, for the specific case  $\eta = 1.5$ ]

$$M_{\text{BH}} V_{\text{osc}}^2 \simeq m_* \sigma(R_{\text{cut}})^2, \quad (78)$$

where  $\sigma$  is the stellar velocity dispersion at  $r = R_{\text{cut}}$ . We note that  $\sigma^2 \simeq 0.1 G M_{\text{tot}} / R_{\text{cut}}$ . Since we can assume that typically  $R_w \ll R_{\text{cut}}$  and, hence,  $M_*(R_w) \simeq M_{\text{tot}} (R_w / R_{\text{cut}})^\eta$  and combining Eq. (77), (78) and the expression for  $\sigma^2$ , we obtain

$$R_w \propto R_{\text{cut}} \left( \frac{m_*}{M_{\text{BH}}} \right)^{1/(2-\gamma)}. \quad (79)$$

In Fig. (22) we show the wandering radius of an IMBH with two different masses for different values of the power-law index  $\gamma$ . As we can see, for shallow values the IMBH can reach significant values. As we have seen in Eq. (12 and in Fig. (6), the system could be relaxed, but this implicitly assumes that the mass- $\sigma$  relationship holds at the low-end of masses, which has not been yet confirmed observationally. This means that we expect a cusp to build around the IMBH, so that for a single-mass population,  $\gamma = 1.75$ , and in the case of a mass spectrum, it will be typically of the order of  $\gamma \gtrsim 1.75$  for the heavier components, and  $\gamma \simeq 1.5$  for the lighter ones.

This quick estimate agrees well with the much more detailed work of [121]. The authors identify three main mechanisms for the wandering of the IMBH: (1) Brownian motion, (2) the effect of the segregated stellar cusp and (3) three-body interactions between stars and the IMBH. The authors however find that Brownian motion is the most important one. Later, [89] ran scattering, numerical experiments of single stars on to a binary formed by the IMBH and another star. Their results are that only IMBHs with masses above  $300 M_\odot$  have small wandering radii. Below this limit, the IMBHs wander off the centre of the cluster. Hence, if Brownian motion was the only phenomenon to take into account, we could assume that the IMBH is fixed at the centre, since for any realistic value of  $\gamma$  the displacement is negligible, and so the treatment of loss-cone could be applied but in view of the results of [89], this can only be done for rather massive IMBHs.

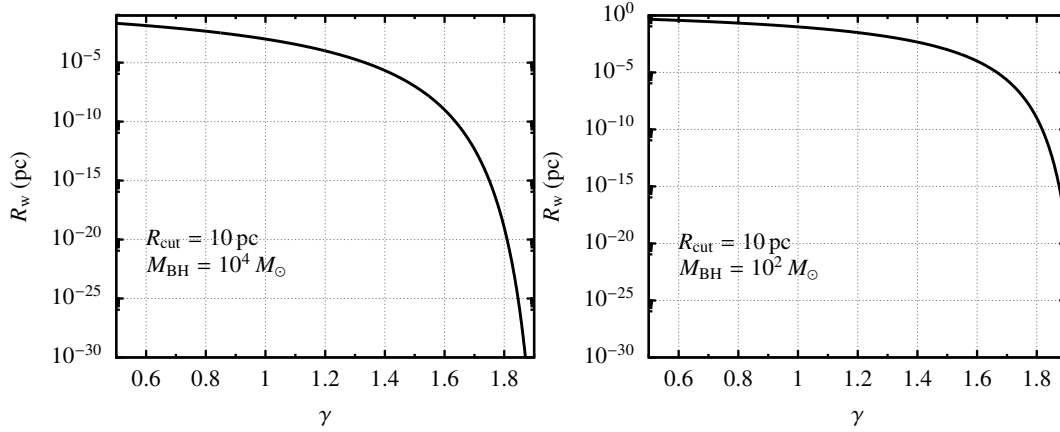


**Fig. 22** Wandering radius  $R_w$  of an IMBH due to Brownian motion in a dense stellar cluster as a function of the power-law exponent  $\gamma$ . We use a so-called “eta” model with cutoff radius  $R_{\text{cut}}$  and the mass of the IMBH is shown as  $M_{\text{BH}}$ .

### *Numerical simulations of IMRIs*

Because of the challenges related to the analytical approach in the case of an IMBH, in particular the wandering of the massive black hole, we need to resort to numerical simulations to at least win some intuition about the physics at role.

For this aim, and as discussed in detail in the relativistic context in [8], the most accurate integration one can do are the so-called direct-summation  $N$ -body algorithms. These integrators have been used for decades in astronomy and have been put to test a number of times with observations and analytical techniques. It all boils down at integrating Newton's equations of motion between all stars in the stellar system at every timestep, with a regularisation algorithm for binaries. Since we are integrating directly, all phenomena purely related to dynamics (i.e. a star is a point) emerge naturally [see e.g. 1, 2, 3, and the latter for the concept of regularisation]. Nowadays many of these Newtonian integrators have adapted a post-Newtonian correction, first implemented in [113]. We note however, that the post-Newtonian expansion assumes the bodies to be completely isolated and without additional perturbations. This has been neglected in all astrophysical integrations with relativistic corrections of this type, but it has been shown that it can induce important errors. Indeed, it has been shown that the so-called cross-terms must be taken into account [182]. These are terms that represent a coupling between the SMBH and the stellar potential. In the case of having a hierarchical triple system, the author shows that the effects of such terms can actually be enhanced to amplitudes of Newtonian order.

But, in general, and even for a binary in vacuum, the post-Newtonian approach is not yet fully understood and as a matter of fact, it has received criticism. In particular, the work of [65] pointed that the derivations either contained inconsistencies or are incomplete. These points have been addressed almost completely, already in the 1990's. There remains however one important open question, about the nature of the sequence itself, because we do not know yet whether it converges, diverges or is asymptotic. However, on the calculation side, we can avoid divergences by carefully constructing the hierarchy of the equations [see e.g. 22]

Nonetheless, it is *for some reason* a very efficient tool to address the evolution of isolated binaries. I refer the reader to the elegant work “On the unreasonable effectiveness of the post-Newtonian approximation in gravitational physics” presented in [181]. The summary could be the following sentence from the article: “The reasons for this effectiveness are largely unknown.”.

We note that an interesting alternative is implementing a geodesic solver to the Newtonian algorithm in the regime of interest; i.e. when the CO is detached from the rest of the stellar system, at distances close to periapsis from the SMBH (or IMBH, in this case). The details are given in Sec. (8.8.2) of [8].

In the context of stellar dynamics and IMRIs, the first numerical work that addressed the formation and evolution of an IMRI in a cluster is the work of [106]. They observe the formation of an IMRI with masses  $M_{\text{BH}} = 500 M_{\odot}$  and  $m_{\text{CO}} = 26 M_{\odot}$ . After some 50 Myrs, the IMRI merges and the IMBH receives a relativistic recoil [45, 27, 86]. The result is that, due to the low escape velocity of the cluster, the IMBH leaves the host stellar system. They noticed in their simulations

that the IMBH forms a binary with a (relatively massive) stellar-mass black hole for about 90% of the time of the simulation.

The interesting fact is that the stellar-mass black hole that forms the IMRI is the result of an abrupt exchange of companion with the IMBH. In view of the initial semi-major axis and eccentricity,  $a \sim 10^{-5}$  pc and  $e = 0.999$ , this capture seems to follow the “gravitational brake” capture of the parabolic orbits: A sudden loss of energy via gravitational radiation can lead to the spontaneous formation of a relativistic binary. This was first presented in the work of [149], while the energy and angular momentum changes in the case of a hyperbolic orbit presented in [92]. This scenario has been recently explored numerically by [105, 130, 137, 115, 100].

The work of [106] has been confirmed by [116], who finds very similar results but using a different numerical scheme. Also, the work of [93] is basically a reproduction of [106] but with a different integrator, which leads the authors to similar results as well. Later, the detailed analysis of [126] explore lighter IMBHs and also find that the IMBH spends about 90% of the integration time on a binary with a CO, also with a distribution of semi-major peaking at values of  $\lesssim 10^{-5}$  pc.

### *Event rate of IMRIs*

As we have discussed previously, we rely on numerical simulations to address the formation and evolution of IMRIs. Therefore, the derivation of the event rate must accordingly rely on a large sample of numerical simulations that allows us to at least have an educated guess about the free parameters that riddle the problem.

In Fig. (23) we show a cartoon of the set of  $3 \times 10^4$  simulations of [20], which sweep the parameter space based on the initial conditions motivated by the previous work of [106, 116, 126, 93]. We elaborate more on this in the next section.

Thanks to the outcome of the numerical study we can make a guess on the event rate that we expect for different detectors. I.e. depending on the horizon distance  $z_{\text{hor}}$  of the detector we consider for a given type of mass, the rates will be different.

The work of [20] derive the rates by estimating the total number of IMRIs within a given cosmological volume of radius  $z_{\text{hor}}$ . We reproduce here their calculation as a way to exhibit clearly the number of free factors that are at play in the calculation. The number of IMRIs,  $\Gamma_{\text{IMRI}}$ , can be obtained via the following integral

$$\Gamma_{\text{IMRI}} = \Omega_s \int_{M_1}^{M_2} \int_0^{z_{\text{hor}}} \frac{dn_{\text{IMRI}}}{dM_{\text{IMBH}} dz} \frac{dV_c}{dz} \frac{dz}{1+z} dM_{\text{IMBH}}, \quad (80)$$

where  $dV_c/dz$  is the comoving cosmological volume element,  $(1+z)^{-1}$  takes into account the time dilation and  $dn_{\text{IMRI}}/dM_{\text{IMBH}}$  expresses how many IMRIs we have per unit of mass. This, as pointed by the authors, can be rewritten as

$$\frac{dn_{\text{IMRI}}}{dM_{\text{IMBH}}} = \xi_{\text{BH}} f_{\text{GW}} p_{\text{IMBH}} n_{\text{rep}} \frac{dn}{dM_g dz} \frac{dn_{\text{GC}}}{dM_{\text{GC}}} \frac{dM_{\text{GC}}}{dM_{\text{IMBH}}}. \quad (81)$$

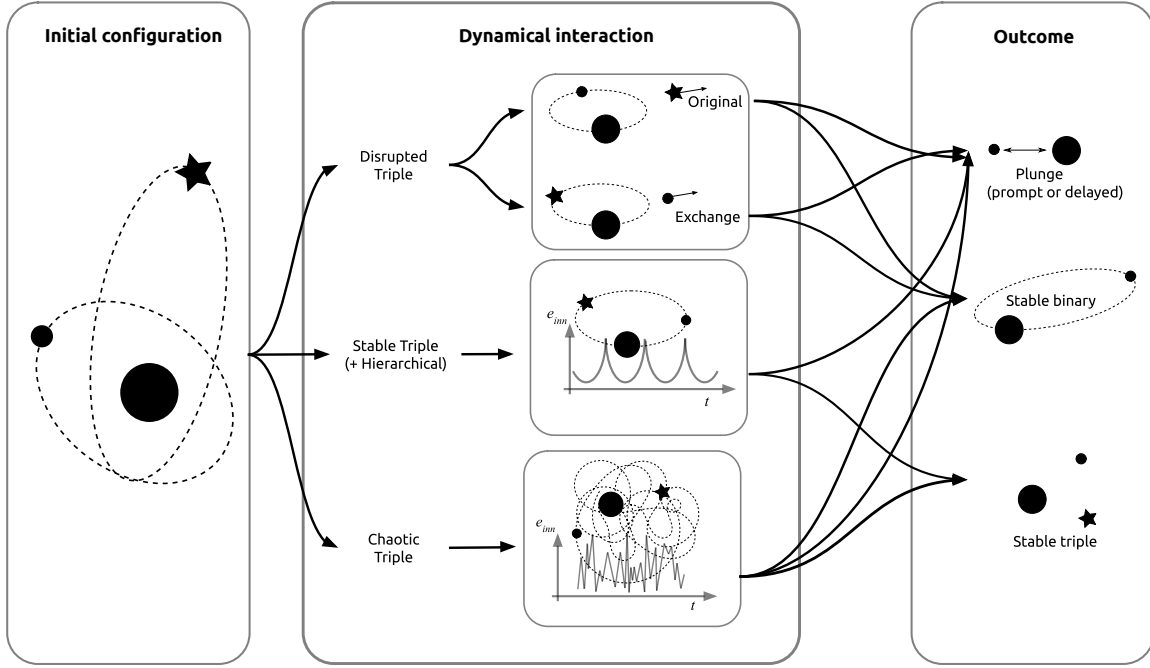


**Fig. 23** Sketch of the set of  $\sim 3 \times 10^4$  numerical simulations of [20]. The three boxes display the different stages in the simulation. The first one corresponds to the initial conditions, which are based on previous works, in particular on [106], which has been confirmed by independent groups. An IMBH (the larger black circle) forms a binary with a stellar-mass black hole (smaller black circle) and a perturber, which is another stellar-mass black hole, but in principle could be another type of star with the proviso that the mass is large enough to have been segregated to small distances from the IMBH (black star). This three-body problem is embedded in an external stellar potential representing the background stellar component, and the evolution can be approximately divided in three different possibilities, as we see in the “dynamical interaction” box. The last box gives us the result of the interaction depending on the details of the initial configuration.

In this last expression  $dn/(dM_g dz)$  is the number of galaxies per  $z$ ,  $\xi_{\text{BH}}$  is (a priori) a free parameter that gives us the probability for an IMBH to be in a binary with a stellar-mass black hole,  $dn/dM_{\text{GC}}$  represents the number of clusters per cluster mass in a certain host galaxy,  $dM_{\text{GC}}/dM_{\text{IMBH}}$  links the mass of the GC to that of the IMBHs,  $n_{\text{rep}}$  is another unknown factor that expresses how often an IMBH can form a binary with a CO,  $f_{\text{GW}}$  is the fraction of successful IMRIs (i.e. those which merge within a Hubble time, an information drawn from their simulations). Finally,  $p_{\text{IMBH}}$  is the probability that an IMBH is indeed lurking in the considered GC. This is very likely the most unknown parameter. The authors rely on the set of Monte-Carlo simulations of [81] and decide to set it to  $p_{\text{IMBH}} = 0.2$ , i.e. 20% of all GC are supposed to be hosting an IMBH. The authors assume a power-law for  $dn/dM_{\text{GC}}$  of the following fashion,

$$\frac{dn}{dM_{GC}} = kM_{GC}^{-s}, \quad (82)$$

with a slope  $s = 2.2$ , for consistency reasons with the initial mass function of young and old star clusters in galaxies, as derived in the work of [e.g. 78], with the normalisation factor  $k$  defined as

$$k = \frac{\delta M_g(2-s)}{(M_{GC2}^{2-s} - M_{GC1}^{2-s})}.$$

We need to assume some reference values for this normalisation. The authors adopt Galactic values, so that  $M_g = 6 \times 10^{10} M_\odot$  and  $M_{GC1,2} = (5 \times 10^3 - 8 \times 10^6) M_\odot$ , and derive  $M_{IMBH} \simeq (30 - 4.6 \times 10^4) M_\odot$ , as well as  $M_{GC}^{-s} = aM_{IMBH}^{-bs}$ , which again, contain two parameters. As for  $dn/(dM_g dz)$ , they resort to the results of [58].

Hence, the number of IMRIs contained in a given observable volume is

$$N_{IMRI} = ka^{1-s} b p_{IMBH} n_{rep} \xi_{BH} \int_{M_1}^{M_2} \int_0^{z_{hor}} f_{GW} M_{IMBH}^{(1-s)b-1} dM_{IMBH} \frac{\phi(z)}{1+z} \frac{dV_c}{dz} dz. \quad (83)$$

with

$$\phi(z) = -\frac{\phi_* 10^{(\alpha_*+1)(M_2-M_*)}}{\alpha_*+1}, \quad (84)$$

a parametric expression of galaxies number density, where  $\phi_*$ ,  $\alpha_*$ ,  $M_*$  a function of  $z$  [see Table 1 in 58], and  $M_2 = 12$ . The estimation limits  $z_{hor}$  to either  $z = 2$  (which corresponds to the peak of GC formation), or  $z = 6$  (formation of the first stars). The probability that the IMBH forms a tight binary with a CO is given by  $\xi_{BH}$ , and it is assumed that  $\xi_{BH} \rightarrow 1$ , based on initial mass function arguments but, more importantly, on the results of the different numerical simulations performed by different groups.

The last piece of information required is the timescale for the IMRIs to form, which can be expressed as the accumulative sum of the timescales for cluster formation, IMBH formation, IMRIs formation and coalescence. Since we are, to put it mildly, at debate about the process that leads to IMBH formation, [20] adopt a weighted timescale for it of 2 Gyr based on the numerical experiments of [81, 21]. They take the mass-segregation timescale for the IMRI formation, which is sensible, of  $\sim 0.1 - 1$  Gyr, and they derive from their simulations that  $t_{GW} = 0.6 - 1.5$  Gyr.

As [20] point out, an alternative way of deriving the merger rate is via the cosmological GC star formation rate  $\rho_{SFR}(z)$ . This can be used to obtain the total number of GCs as a function of  $z$ ,

$$N(z_{max}) = \int_0^{z_{max}} \frac{\rho_{SFR}(z)}{\langle M_{GC} \rangle} \frac{dV_c}{dz} \frac{dz}{1+z}. \quad (85)$$

If one adopts the power-law GCs mass function, the normalisation in this case is

$$k = \frac{(1-s)}{M_{\text{GC},1}^{1-s} - M_{\text{GC},2}^{1-s}}, \quad (86)$$

so that the total number of IMRIs within a given volume is

$$N_{\text{IMRI}} = ka^{1-s}bp_{\text{IMBH}}n_{\text{rep}} \int_{M_1}^{M_2} \int_0^{z_{\text{hor}}} M_{\text{IMBH}}^{(1-s)b-1} f_{\text{GW}} \rho_{\text{SFR}}(z) \frac{dV_c}{dz} \frac{dz}{1+z} dM_{\text{IMBH}}. \quad (87)$$

Therefore, so as to obtain the merger rate, we convert Eqs. (83) and (87) at a given  $z$  with the relation  $\Gamma_{\text{IMRI}} = N_{\text{IMRI}}/T$ . Therefore, we can convert the rates to specific detectors, and we have that

- **LIGO/Virgo** should detect up to 1 – 5 IMRIs per yr with  $M_{\text{IMBH}} \simeq 100 M_{\odot}$
- **LISA** is in the position of observing up to  $\sim 6 - 60$  events per yr
- **ET** could detect 100 – 800 IMRIs per yr with masses  $M_{\text{IMRI}} < 2000 M_{\odot}$
- **Decihertz detectors** could detect up to 3800 events per yr

Obviously, in view of the detection of [118] of the system GW190521 by LIGO/Virgo with a mass  $142 M_{\odot}$  suits well these predictions but we are talking about single-point statistics. We need to wait to have more detections to derive any conclusion.

### **Multibandwidth IMRIs**

Intermediate-mass ratio inspirals are particularly interesting because, as discussed in [6], they can not only be detected by future space-borne gravitational wave observatories. Depending on their masses and, in general, dynamical parameters, they could already be present in ground-based detectors, such as LIGO/Virgo. Moreover, also depending on their dynamical characteristics, a percentage of them will be detectable by both space-borne- and ground-based facilities.

As we have already mentioned in the previous section, we rely on numerical simulations to address this kind of source. We stress out that the findings of the first numerical simulation by [106] have been confirmed by at least another three different groups. This is important, because IMRIs seem to form at very high eccentricities and very small semi-major axes. To illustrate this, in Fig. (24) and Fig. (25) we show the eccentricities and semi-major axes of one of the simulations of [106], which led to the formation of an IMRI. This particular example is a representative one of what has been found by other groups. The IMBH forms a binary with a compact object, a stellar-mass black hole of mass  $\sim 20 M_{\odot}$  for most of the time of the simulation. The binary is ionised and the CO replaced with another one, which is also of the same type and mass, while the semi-major axes become smaller and smaller. Eventually, after an abrupt interaction, a final binary forms with an initial eccentricity of  $e \sim 0.999$  and the IMRI forms and merges in a fraction of the total

simulation time ( $\sim 2.5\%$  of the total). In these figures we can see how quickly both the semi-major axis and eccentricity decay.

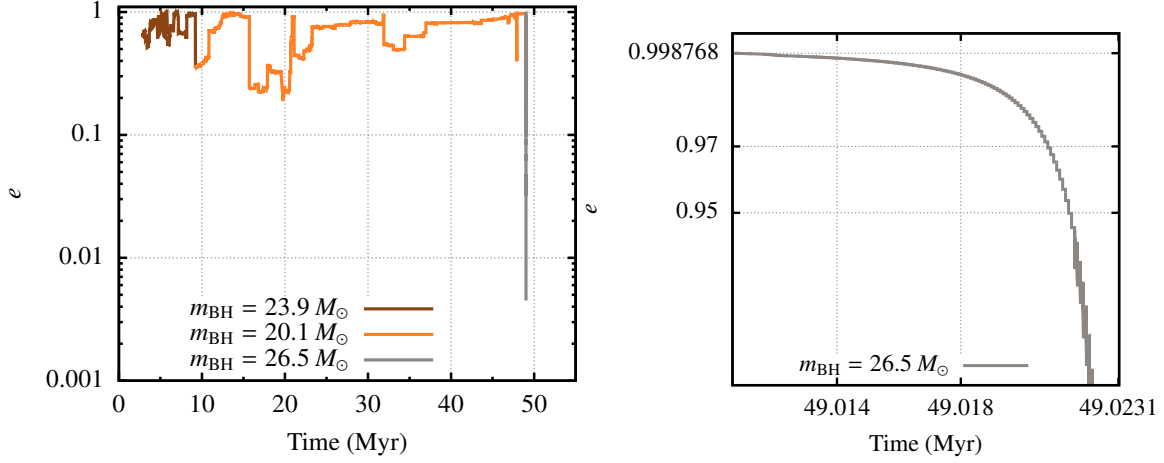


**Fig. 24** Evolution of the eccentricity for the three different stellar-mass black holes which form a binary with the IMBH (data from [106]), as a function of time. The masses of the three COs is shown in the left panel, which is the complete evolution of the three systems. On the right panel we have a zoom in of the last binary, which lasts  $1.25 \times 10^4$  yr from the formation to the merger. We can see the extreme eccentricity that it achieves and how quickly it circularises as an effect of the radiation of energy.

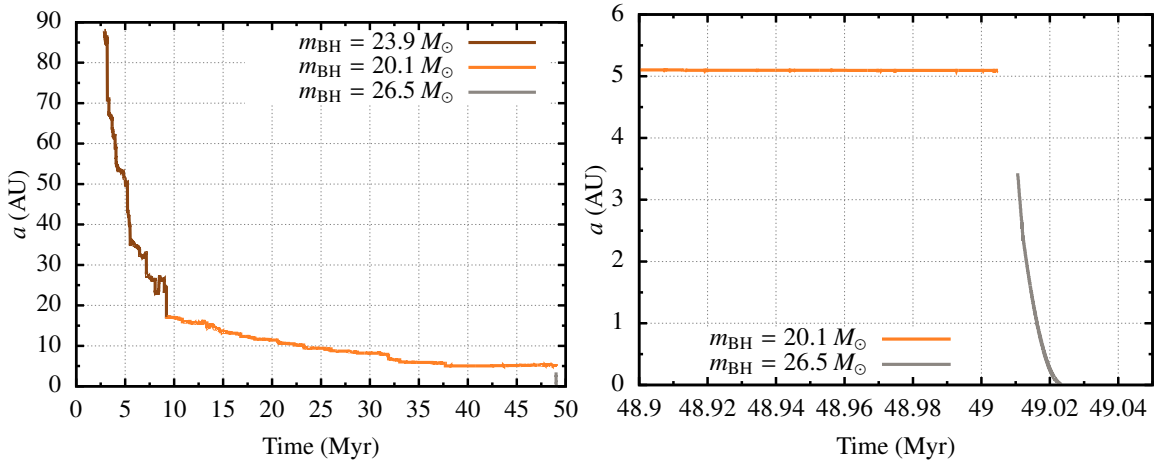


**Fig. 25** Same as Fig. (24) but for the semi-major axes. On the right panel we only show the evolution of the two last COs in the order of the dynamical interactions with the IMBH.



Based on these results, and in view of the similarity with other groups, we can take these initial values as representative and ask the question how these systems would be observed from the space and from the ground, as in the work of [6]. In Fig. (26) we follow the approach of Eq. (58). We can see that the dominant harmonic  $n = 2$ , crosses a range of frequencies in a timescale of a few years. This means that if LISA and ground-based observatories are operational at the same time, a LISA detection would translate into a forewarn to decihertz observatories (if any) and the ground-based LIGO/Virgo (or ET).

This is interesting because the combination of these detections would allow us to impose enhanced constraints on the system's parameters. Since LISA can observe the inspiral, we can derive parameters such as the chirp mass easily. Ground-based detectors are in the position of observing the merger and ringdown, and hence one can derive additional parameters such as the final mass and spin. This compound detection has also the advantage of splitting various degeneracies and therefore to achieve better measurements of the parameters, as compared to individual detections.

In the work of [6] it is shown that IMBHs with light and medium-size can be observed by space-borne and ground-based observatories with eccentricity values ranging between  $e \in [0.99, 0.9995]$ . The most eccentric ones can only be seen from the ground [see discussion in 52]. This is an implication of the characteristic frequency changing as the pericenter distance decreases because eccentricity increases. The peak frequency is therefore shifted [see Eq. 37 of 180]. Heavier IMBHs have their frequency peak receding in frequency as compared to medium-size ones, and therefore the harmonics are embedded in the LISA range.

We can estimate the signal-to-noise ratio (SNR or  $\rho$ ) as follows. Assuming that the  $h_c$  of an IMRI is, at a given frequency  $f$  [70]

$$h_c = \sqrt{(2\dot{E}/\dot{f})/(\pi D)}, \quad (88)$$

where  $\dot{E}$  is the power emitted, and  $\dot{f}$  the time derivative of the frequency, the sky- and orientation-averaged  $\rho$  of a monochromatic source (assuming the the ansatz of ideal signal processing) is [70]

$$(\rho)^2 = \frac{4}{\pi D^2} \int \frac{\dot{E}}{\dot{f} S_h^{SA}(f)} \frac{df}{f^2} \quad (89)$$

where  $S_h^{SA}(f) \approx 5S_h(f)$  is the sky- and orientation average noise spectral density. For a source with multiple frequency components, the total value of  $\rho^2$  is obtained by summing the former equation for the different components.

For high-eccentricity sources we use the expression [see 6, for an explanation]

$$(\rho)_n^2 = \int_{f_n(t_{\text{ini}})}^{f_n(t_{\text{fin}})} \left( \frac{h_{c,n}(f_n)}{h_{\text{det}}(f_n)} \right)^2 \frac{1}{f_n} d(\ln(f_n)), \quad (90)$$

where  $f_n(t)$  is the (redshifted) frequency of the  $n$  harmonic at time  $t$  ( $f_n = n \times f_{\text{orb}}$ , with  $f_{\text{orb}}$  the orbital frequency),  $h_{c,n}(f_n)$  the characteristic amplitude of the  $n$

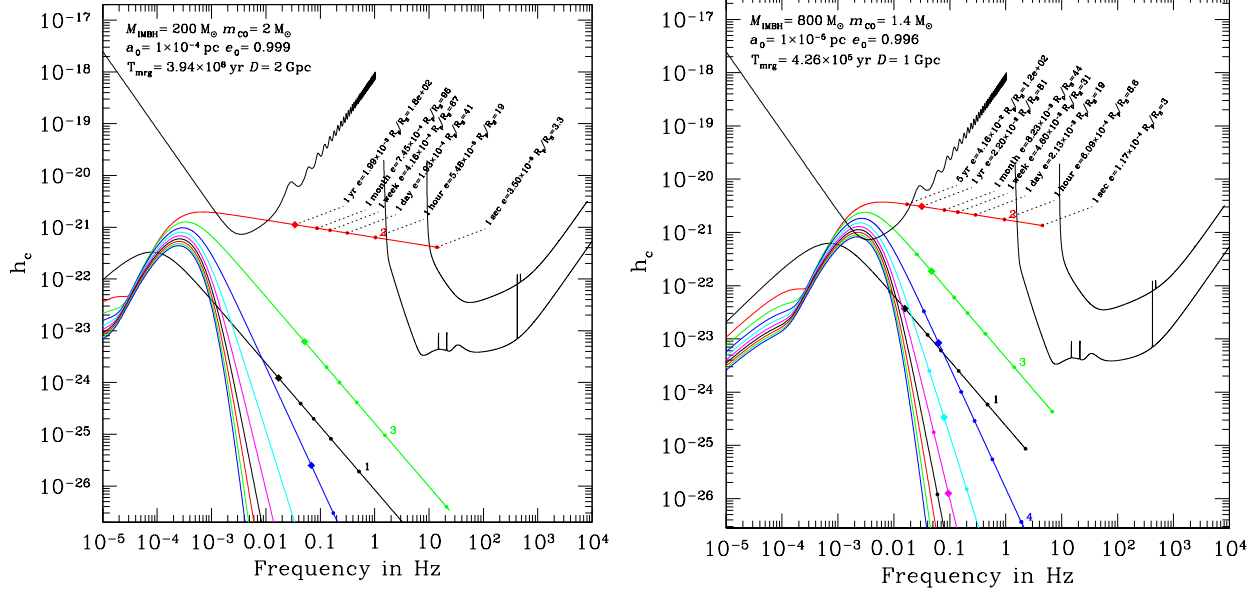


**Fig. 26** Evolution of the first harmonics of IMRIs with typical values for the semi-major axis and eccentricity. As in Fig. (15), we show different moments in the evolution, as well as the periastron distances, distance to the source, and the merger time. Additionally, we also display the Einstein Telescope [155, 97] sensitivity curve on the right, at higher frequencies, and above it, the LIGO sensitivity curve.

harmonic when the frequency associated to that component is  $f_n$ , and  $h_{\text{det}}$  is the square root of the sensitivity curve of the detectors.

With this in mind, we can estimate typical SNRs for different detectors and sources. Typically, the values are from tens of LISA, LIGO to thousand in ET, at  $D = 500 \text{ Mpc}$  [6].

We therefore have that IMRIs are (a) sources that might already be present in current ground-based observatories and (b) multiband probes. The fact that no IMRI has been yet detected (and we are excluding here the “mysterious source” [119], because it has  $q \simeq 0.1$ ) is very likely due to the reasons given in the next section.

However, there is another particular characteristic of IMRIs that makes them interesting, at least from the point of view of modelling. This is the fact that they are “clean sources”. What this means is that, contrary to EMRIs, which might have their inspiral affected by gas effects (or even dark-matter, if one invokes such a possibility), IMRIs can and must be considered as a relativistic two-body problem in vacuum from the moment in which it is formed and the driving mechanism is the emission of GWs (i.e. once it has detached from the stellar dynamics regime, see Fig. (12) and related discussion).

This is so because (a) globular clusters have a negligible amount of gas and (b) the timescale for merger, once the IMRI has formed, is very small as compared to other typical timescales associated to perturbations. Indeed, [6] shows this by

analysing the evolution of a completely isolated IMRI and another one embedded in a dense stellar system with typical densities of  $\sim 10^5 - 10^6 M_\odot \text{pc}^{-3}$ . When comparing the evolution of the isolated case with the multi-body one, there is no difference.

Finally, we note that it is possible to use IMRIs to extract properties of the host environment by following the method of accumulated phase shift. Indeed, [6] finds that, imposing a threshold  $\text{SNR} = 5$ , for LISA and the ET  $\Delta\Psi_f(e) \gtrsim 10^4$  radians, and some systems, typically the light ones, in LIGO have  $\Delta\Psi_f(e) \gtrsim 10$  radians. This means that we can extract information from the host cluster from IMRI detections.

### ***Modelling IMRIs***

Detecting IMRI systems in GW-data will require us to push data analysis techniques to beyond the state-of-the-art. In particular, we need to include higher signal harmonics and to combine data from multiple detectors coherently. All the gravitational-wave events found so far are from binaries in which the two components have comparable masses, in any case very different from the asymmetric systems we are considering here.

This asymmetry has two implications. First, the gravitational wave signal is much more complicated, mostly due to the higher modes and harmonics becoming more important. Secondly, the higher asymmetry implies that the signals have a lower amplitude (compared to a more symmetric system which is equally far away). Thus, the analysis must be more sensitive by including more physical effects, and by combining the data from multiple detectors more optimally.

All of the searches thus far have only looked for the dominant harmonic of the signal with additional physical restrictions (especially assuming no-precession) and moreover, they have combined the data from different detectors without considering phase coherence. It is thus not a surprise that the highly asymmetric systems have not yet been found. This would require dropping these simplifying assumptions. We would need to include higher signal harmonics and precession, and also combine data from the different detectors coherently.

However, even assuming that the signal detection problem have been understood and addressed, we will still not be able to find IMRIs. This requires critical advances in general relativity and numerical analysis. To explain this, we need to briefly discuss the existing methods and their range of validity.

Comparable mass-ratios, as exemplified by the current LIGO/Virgo detections, are modeled by post-Newtonian methods [see 40, for a review] for a review, while the extreme-mass ratio systems relevant for LISA require the self-force calculations in general relativity [see 32, 144, for a review].

The intermediate-mass ratio systems fall in the middle and represent an unexplored part of parameter space. The most reliable calculations of the gravitational signal are by solving the Einstein equations numerically. For comparable mass-ratio systems, it is now routine to solve the equations with astrophysical initial conditions and to calculate the full gravitational wave signal.

Current methods do not work when the mass ratio  $q = m_{\text{CO}}/M_{\text{BH}}$  is small; it is computationally far too expensive to simulate even a fraction of an orbit for  $q \sim 10^{-3}$ . The most extensive publicly available catalogues of gravitational waveforms [136, 119] currently only go until  $q = 0.1$ , and  $q = 0.01$  represents the smallest ever mass ratio simulated [123, unfortunately covering too few orbits]. The most extreme mass ratio found by the LIGO/Virgo collaboration is GW190814, the “mystery object” [119], and it has  $q \simeq 0.1$ .

The presence of the much smaller black hole introduces a small length scale in the problem which, in the standard approach, needs to be resolved. This affects then the time steps in the integration of the Einstein equations and the computational cost increases correspondingly. Going to  $q \sim 10^{-3}$  or  $10^{-4}$  is well beyond the capabilities of current methods. At the other end, very small values of  $q \lesssim 10^{-5}$  can be studied using the self-force calculations, analogous to the self-force due to electromagnetic radiation in classical electrodynamics. Here  $q$  is a small parameter linearly perturbing a background solution [32, 145]. While several difficulties remain, it is reasonable to expect that current methods can address the problem. These methods cannot however be extended for  $q \sim 10^{-3}$  as this would necessitate going well beyond the linear perturbation approximation.

It is worth pointing out here that there are attempts to interpolate between the two regimes, in particular by the “effective-one-body” approach [see e.g. 44, 41]. In this approach, as the name suggests, the idea is to replace the true 2-body system by an effective description in terms of a 1-body system with a modified Hamiltonian. The results of this approach have proven to be effective in the comparable mass and extreme mass ratio regimes, however it is not clear that this will work in the intermediate-mass ratio regime.

## Extremely-large mass ratio inspirals

We have seen in Fig. (5) the range of masses for a stellar object to plunge directly through the event horizon of a SMBH without suffering significant tidal stresses, as a function of the mass of the object. We note that there is a range of masses which correspond to sub-stellar objects, in particular to brown-dwarfs (BDs) which will inspiral and cross the event horizon of SgrA\* in our Galaxy without being disrupted.

The typical mass of a BD translates into a mass ratio, for SgrA\* of  $q \sim 10^{-8}$ . This is particularly interesting because if one of these BDs was to form a relativistic binary with the SMBH in our Galaxy, because of the following points,

1. The number of cycles that it would revolve until plunging into the event horizon is roughly inversely proportional to  $q$  [see e.g. 127]. This means that a BD would describe of the order of  $\sim 10^8$  cycles in the band of the detector (in this case LISA). Because of this value, these sources are called “extremely-large mass ratio inspirals” (XMRI).
2. Due to the previous point, XMRI would have a much longer life in the band of the detector as compared to an EMRI.

3. Because of the distance to our Galactic Centre, of  $\sim 8$  kpc, the signal-to-noise ratio (SNR) of an XMRI would be extremely high, achieving that of binaries of SMBHs or even exceeding it.
4. Since backreaction is proportional to the mass ratio, the modelling of XMRI would be much easier than that of EMRIs and, in any case, trivial as compared to IMRIs. The orbit approaches more and more a pure geodesic and is, hence, trivial to calculate.

These points were realised by [19]. In this work, the author addresses the possibility that one of these sources exists in our Galactic Centre, and estimates the associated SNR.

The mass of a BD ranges approximately between  $0.012M_\odot$  to  $0.076M_\odot$ . We note that this is a lower limit, since they can also have masses in the range  $0.07 - 0.15M_\odot$  through the BD formation process, see [111], so that the results here are to be regarded as conservative, since we assume masses lower than  $0.07M_\odot$ .

By following a similar procedure as the one presented starting from Eq. (88), and in the same approach, [19] calculates the SNR for conservative values of XMRI systems and finds that LISA would be able to detect them with SNRs ranging from 10 millions of years before the final plunge, to values as high as  $\text{SNR} \gtrsim 10^4$  thousands of years before it, assuming only one year of observation. We can see this in Fig. (??).

In Fig. (28) we show the evolution in phase-space of a typical XMRI. We can see that the XMRI can spend millions of years in the band of the detector. This is the reason (and the proximity in distance) of the large SNR of Fig. (27).

The event rate for an XMRI to plunge into the SMBH of our Galaxy is not drastically higher than what can be expected for an EMRI, given in Eq. (70) and Eq. (??). The procedure to derive the event rate is very similar to that of stellar-mass black holes, i.e. EMRIs, with a crucial subtlety related to the dynamics of BDs, which we summarise here for the convenience of the reader, and refer to details to the work of [19].

BDs have their own initial mass function, which is not well-constrained, but it can be approximated by a single power law [Eq. 4.55 of 111], and this is consistent with the observational data of [179]. Moreover, we can assume that relaxation is dominated, driven, by stellar-mass black holes. This implicitly assumes that relaxation can be added up individually from these two mass species, the BDs and the stellar-mass black holes. Indeed, close to the central region, energy equipartition is found only among the largest masses, and this equipartition is spread then to velocity at low masses first [38]. This means that for a given distribution  $f(m, v)$  with  $v$  the velocity and  $m$  the mass, the moment of the change of velocities is

$$\langle dv^2 \rangle = \int dv^2 f(m, v) dm dv.$$

Because we can neglect equipartition among the low-mass object, we can then express this as

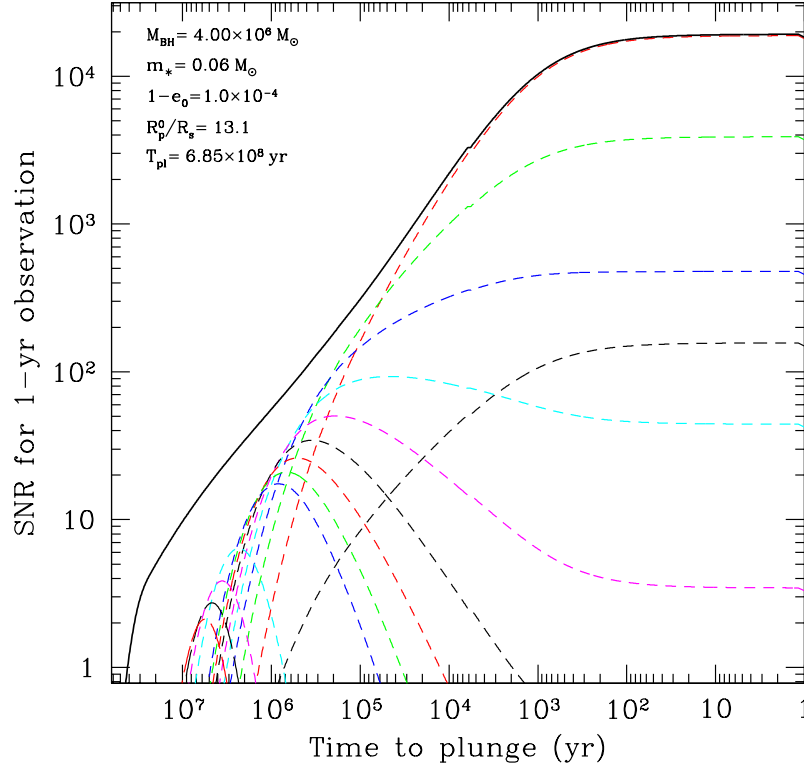


**Fig. 27** SNR of an XMRI with typical parameters in our Galactic Centre. About  $10^7$  yrs before the BD plunges through the event horizon, and assuming that we can only follow the XMRI for one year, it can be observed with a SNR of 10. Different lines correspond to different harmonics, while the black, upper line is the sum of them. One million of years before the plunge, it achieves  $\text{SNR} \simeq 60$ . From a thousand years before the plunge, it is  $\text{SNR} \gtrsim 10^4$ .

$$\langle dv^2 \rangle = \sum_m n(m) \left( \int dv^2 f(v) dv \right),$$

with  $n(m)$  the density of stars of mass  $m$ . This is crucial, because it implies that (1) BDs must be close to the centre and (2) we can ignore the contribution of relaxation provided by them.

The event rate, as derived in [19], and following the same nomenclature starting from Eq. (68), is

$$\dot{N}_{\text{X-MRI}} = \frac{3-\beta}{2\lambda} \frac{N_{\text{OMS}}^{\text{BD}}}{T_0 R_h^\lambda} f_{\text{sub}}^{\text{BD}} \times \left\{ a_{\text{crit}}^\lambda \left[ \ln(\Lambda_{\text{crit}}) - \frac{1}{\lambda} \right] - a_{\text{min}}^\lambda \left[ \ln(\Lambda_{\text{min}}) - \frac{1}{\lambda} \right] \right\},$$

where we have introduced  $\lambda = 9/2 - \beta - \gamma$ ,  $\Lambda_{\text{crit}} = a_{\text{crit}}/(8R_s)$  and  $\Lambda_{\text{min}} = a_{\text{min}}/(8R_s)$ .

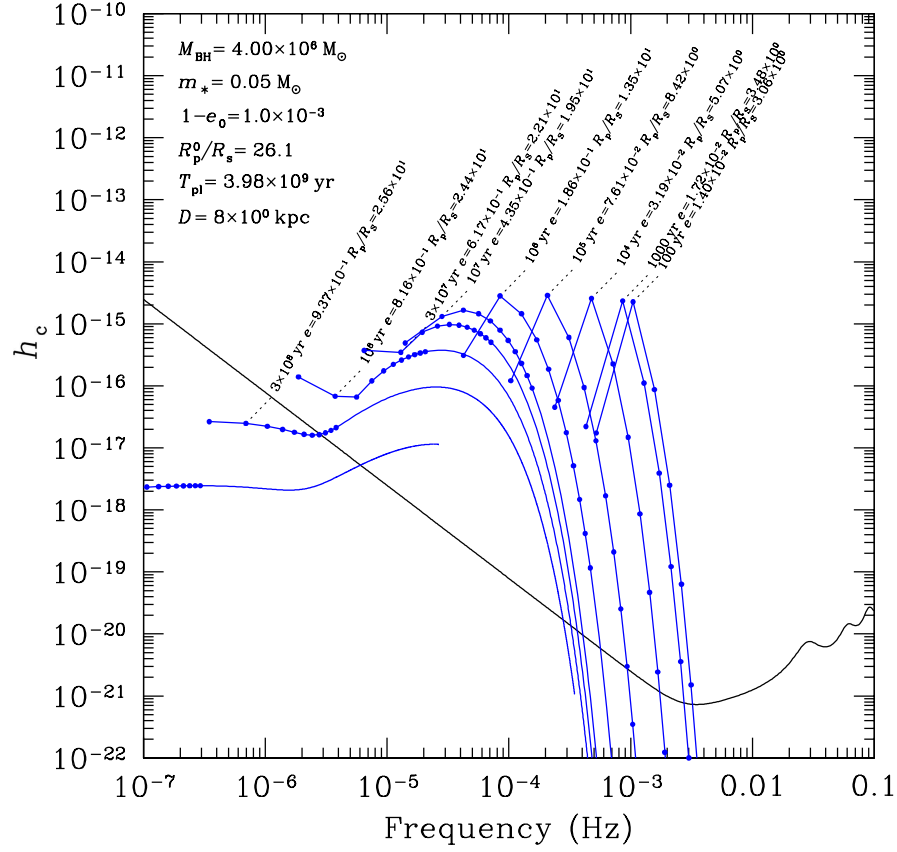


**Fig. 28** Evolution in phase-space of an XMRI following the same approach and convention as in Fig. (12). However, instead of showing the different harmonics as in that figure, we display the isochrones. This means that a curve depicts the position of the different contribution of the different harmonics at the same time. At the time of formation, the XMRI time to plunge is of  $T_{\text{pl}} \sim 4 \times 10^9$  yrs.

As with the EMRI rates, and following the same notation, we give now two examples, the BW- and SM-solution,

$$\begin{aligned}
\dot{\Gamma}_{\text{BW}} &\sim 1.8 \times 10^{-4} \text{ yrs}^{-1} \hat{N}_0 \hat{\Lambda} \hat{r}_{\text{infl}}^{-11/4} \times \\
&\left\{ 1.34 \times 10^{-4} \hat{r}_{\text{infl}}^{5/4} \hat{N}_0^{-1} \hat{\Lambda}^{-1} \hat{m}_{\text{BD}} \mathcal{W}(\iota, \mathbf{a}_\bullet) \times \right. \\
&\left[ \ln \left( 262 \hat{r}_{\text{infl}} \hat{N}_0^{-4/5} \hat{\Lambda}^{-4/5} \hat{m}_{\text{BD}}^{4/5} \mathcal{W}(\iota, \mathbf{a}_\bullet)^{-2} \right) - \frac{4}{5} \right] - \\
&\left. 6.86 \times 10^{-25/4} \hat{r}_{\text{infl}}^{5/4} \times \left[ \ln(15.22 \hat{r}_{\text{infl}}) - \frac{4}{5} \right] \right\}. \quad (91)
\end{aligned}$$

Where we have introduced  $\tilde{m}_{\text{BD}} := m_{\text{BD}} / (0.05 M_\odot)$ . In the case of SM, we have that

$$\begin{aligned}
\dot{\Gamma}_{\text{SM}} &\sim 2.3 \times 10^{-3} \text{ yrs}^{-1} \hat{r}_{\text{infl}}^{-5/2} \hat{N}_0 \hat{\Lambda} \times \\
&\left\{ 1.4 \times 10^{-4} \hat{r}_{\text{infl}} \hat{N}_0^{-1} \hat{\Lambda}^{-1} \hat{m}_{\text{BD}} \mathcal{W}(\iota, \mathbf{a}_\bullet)^{-5/2} \times \right. \\
&\left[ \ln \left( 46 \hat{r}_{\text{infl}} \hat{N}_0^{-1} \hat{\Lambda}^{-1} \hat{m}_{\text{BD}} \mathcal{W}(\iota, \mathbf{a}_\bullet)^{-5/2} \right) - 1 \right] - \\
&\left. 4.67 \times 10^{-7} \hat{r}_{\text{infl}} \times [\ln(15.24 \hat{r}_{\text{infl}}) - 1] \right\}. \quad (92)
\end{aligned}$$

We reproduce here the results of [19], in Fig. (29). We can see that the event rate is not much higher as for the EMRI case, see Eq. (68) and the examples.

The important, and interesting point about XMRI is that, contrary to more massive EMRIs, XMRI spend a long time on band, as we have seen. They start with a  $\text{SNR} > 10$  in LISA  $T \sim 10^6 \text{ yr}^{-1}$  before the final plunge, and the event rate  $\dot{\Gamma} \cong 10^{-5} \text{ yr}^{-1}$ . Therefore, the number of sources in band at *any given moment* (with the proviso that the nucleus is relaxed) is the multiplication of the event rate times their lifetime, i.e.  $\sim$  a few 10.

From the continuity equation of the events we can derive the relative occupation fractions of the (line) density  $g = dN/da$ , with  $N$  the number of sources and  $a$  their semi-major axes. Taking into account the eccentricity of the sources when integrating  $N$ , [19] finds

- $\gtrsim 15$  X-MRIs at low frequencies with high eccentricities and associated SNRs of  $\simeq$  a few 100.
- $\gtrsim 5$ , at higher frequencies, i.e. at very high SNRs (from a few 100 up to  $2 \times 10^4$ ), in circular-, or almost circular orbits.

Is is important to stress that this derivation has been done assuming a steady-state distribution; it is a statistical representation of the system. This means that, *at any given moment of the Milky Way* -under the assumption that our Galactic Centre is in the range of relaxed nuclei, see Fig. (6)-, *the numbers of sources that we quote above hold*. If this requirement is fulfilled, this means that millions of years ago and



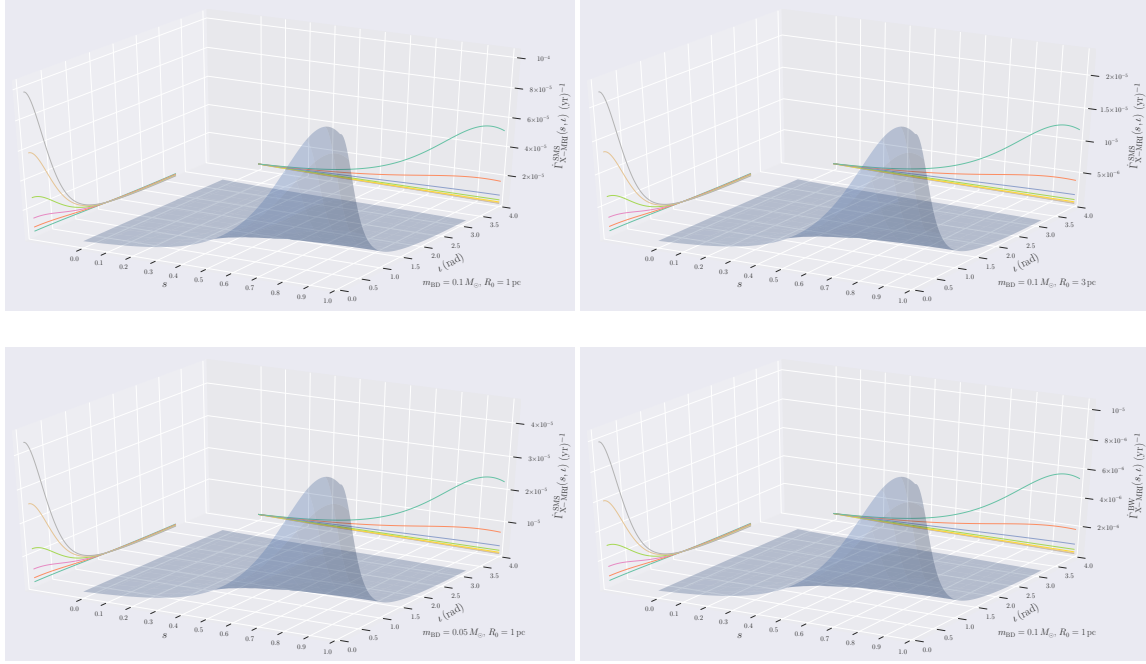


**Fig. 29** Event rate for XMRI at the Galactic Centre in the BW- and SM solution.

millions of years in the future, those are the numbers of XMRI that we can expect to be populating the Galactic Centre.

We stress that these are conservative values. These numbers can be multiplied by a factor of a few depending on the eccentricity of the sources when they form. Also, this approach is purely analytical and based on pure power-laws. These should decrease as one approaches the innermost radii, which translates into a more efficient diffusion of stellar-mass black holes. Hence, we are artificially enhancing the relaxation time and therefore decreasing the event rate.

While the SNRs are very high, to the point of being able to bury the SNR of binaries of SMBHs in some cases, the distance plays a crucial role. This means that, whilst we can expect to detect them in our own Galactic Centre, other galaxies are out of question but for, maybe, satellite galaxies of M82 with SMBHs in the range of LISA.

Because of their extreme mass ratios, these systems are closer to a geodesic than EMRI, which makes it easier to model them. However, because XMRI evolve so slowly, in the lifetime of LISA they can be envisaged as monochromatic sources. This, in turn poses the question of how many of them and in what distribution of orbital parameters would we need to reproduce the exploration of timespace that an EMRI can do. An EMRI probes a vast range of values in the semi-major axis, eccentricity and change of plane of the orbit in as short as a few months or years. Each burst can be considered like a picture of warped spacetime, and hence it delivers us

with thousands of pictures to allow us to do a cartography of that spacetime around the SMBH. An XMRI, on the contrary, is “fixed” in phase-space and the question arises of how many of them, and in what distribution, would we need to derive that mapping of spacetime

There is an additional problem related to XMRI. Since we can expect the Milky Way to be a proxy galaxy of the type that LISA will probe, it is very likely that an important fraction of all of them will have a few XMRI distributed around their SMBHs. As we have noted before, this is a steady-state representation of relaxed nuclei. In other words, we can expect that all *relaxed* nuclei in the range of masses that LISA will observe will have a few tens of XMRI distributed around the SMBH moving at a fraction of the speed of light.

Any infalling EMRI will therefore inevitably encounter them on its orbit towards the final plunge into the SMBH. Because the XMRI are moving at such high velocities, their effective masses are similar to those of the EMRI, which means that an interaction EMRI-XMRI can significantly alter the orbit of the EMRI or, even worse, scatter it completely off, cancelling the merger of the system.

## A Relativistic Fokker-Planck Algorithm

As we have seen in the previous sections, the problem of forming an EMRI (or IMRI/XMRI) involves both astrophysics (in particular stellar dynamics) and general relativity. This is challenging because this translates into addressing the two-body problem in general relativity, which is unsolved at these mass ratios, as we have briefly described before, and the  $10^6$ – $10^8$  body problem in Newtonian gravity. The host galactic nucleus (in the case of an EMRI or XMRI) or globular cluster (for an IMRI) has that order of stars. While we care about relativistic effects between COs and the central SMBH/IMBH, relativity does not play a significant role in general among the stars that form part of the stellar system in which the inspiral takes place.

In this section, which gives the primary idea of [12], we describe what ought to be done to address this problem with a two-dimensional Fokker-Planck integrator, which has shown to be very robust even compared to direct  $N$ –body simulations [see e.g. 148, 9], with the advantage that (i) one has a control over the physics as it is implemented into the integrator scheme and (ii) the Fokker-Planck approach is orders of magnitude faster than any brute force, direct-summation integrator.

Before we describe the main idea, we need to introduce a few physical concepts, and the connection between the Newtonian and relativistic regimes.

### *Newtonian motion around a Newtonian potential*

We start from the Hamiltonian of Eq. (106). In this case, the equation for radial motion can be written as:

$$\left(\frac{dr}{dt}\right)^2 = -2E + \frac{2GM_{\text{BH}}}{r} - \frac{J^2}{r^2} = \frac{2E}{r^2}(r_a - r)(r - r_p). \quad (93)$$

From here, and using the definitions of the previous section of the pericenter and apocenter radial coordinates, we find

$$E = \frac{GM_{\text{BH}}}{r_p + r_a} = \frac{G(1 - e^2)}{2p}, \quad (94)$$

$$J^2 = \frac{2GM_{\text{BH}}r_p r_a}{r_p + r_a} = GM_{\text{BH}}^2 p. \quad (95)$$

### ***Relations between the Relativistic and Newtonian parameters for a Schwarzschild SMBH***

In order to connect the Newtonian and relativistic calculations into a single Fokker-Planck integrator, it is important first to have a clear way of connecting the Newtonian and relativistic parameters describing the orbital motion. Here, we want to relate the Newtonian constants of motion  $(E, J)$  of Eqs. (106) and (107) with the relativistic constants of motion  $(\mathcal{E}, \mathcal{J})$  of Eqs. (23). Let us start first with the angular momentum. For that, we need to compare the Newtonian definition of the angular momentum in terms of the spherical coordinates of motion

$$J = r^2 \dot{\phi}, \quad (96)$$

with the second equation in (23). We realize that, by identifying the radial and azimuthal coordinates (there is a justification for this), we can just identify the angular momentum parameters, i.e.

$$\mathcal{J} \equiv J. \quad (97)$$

The case of the energy is more complex, in part because of the intrinsic four-dimensional character of general relativity. Moreover, the properties of the Einsteinian and Newtonian gravitational fields are different and complicate the comparison since, at finite distance, the energy involves the gravitational potential. Hence, the ideal way of comparing things is by going to spatial infinity, which means analyzing the energy at  $r \rightarrow \infty$ . At infinity, the relativistic specific energy satisfies

$$\Gamma_\infty = u_\infty^t = \mathcal{E}, \quad (98)$$

$$\Gamma_\infty = \frac{1}{\sqrt{1 - v_\infty^2}}, \quad (99)$$

where we have used Eqs. (23) and (33) in the case of the Schwarzschild metric. Here  $v_\infty^2$  is the spatial velocity at infinity, given by

$$v_\infty^2 \equiv g_{ij}^\infty v_\infty^i v_\infty^j = \left( \frac{dr}{d\tau} \right)_\infty^2 + \left[ r^2 \left( \frac{d\phi}{d\tau} \right)_\infty^2 \right]. \quad (100)$$

Then, combining Eqs. (98) and (99) we obtain the well-known relation in special relativity:

$$v_\infty^2 = \frac{\Gamma_\infty^2 - 1}{\Gamma_\infty^2} = \frac{\mathcal{E}^2 - 1}{\mathcal{E}^2}. \quad (101)$$

In the Newtonian case, from Eq. (106), we have

$$v_\infty^2 = -2E. \quad (102)$$

Hence, by comparing we can relate both energies in the following way

$$E = \frac{1 - \mathcal{E}^2}{2\mathcal{E}^2}, \quad \mathcal{E} = \frac{1}{\sqrt{1 + 2E}}. \quad (103)$$

Since we are analyzing the equations at infinity, this is only valid for unbound orbits, which satisfy  $E < 0$ . For bound orbits we have to make a different analysis. A possibility is to identify the  $(e, p)$  parameters as they have the same meaning both in Newtonian and Einsteinian gravity, as they determine the turning points of the motion, i.e.  $r_p$  and  $r_a$ . However, this produces  $\mathcal{J} \neq J$ , which in principle is not a problem by itself. By doing this identification one can get the following relations

$$\frac{\mathcal{J}^2 - J^2}{\mathcal{J}^2} = \frac{4 + e}{p}, \quad (104)$$

$$\frac{E - \frac{1 - \mathcal{E}^2}{\mathcal{E}^2}}{\frac{1 - \mathcal{E}^2}{\mathcal{E}^2}} = \frac{4(1 - e^2)}{p(p - 4)}, \quad (105)$$

where we are comparing the Newtonian energy  $E$  with  $(1 - \mathcal{E}^2)/\mathcal{E}^2$  [as in Eq. (103)]. We have normalized with respect to the relativistic values as they are supposed to be closer to reality. Notice that for orbits with big  $p$ , the identification can be reasonable, as both expressions go to zero as  $p$  goes to infinity.

### ***Relations between the Relativistic and Newtonian parameters for a Kerr SMBH***

In this case the situation is a bit more complicated, as we have an additional constant of motion. In a spherically symmetric gravitational potential the constants of motion are just two,  $(E, J)$ , but in the case of a spinning SMBH (Kerr geometry) there are

three:  $(E, \mathbf{J}_z, C)$ , where  $\mathbf{J}_z$  is the angular momentum component in the spin direction and  $C$ , the Carter constant, related to the total angular momentum.

In the Newtonian limit  $\mathbf{J}_z^2 + C \approx \mathbf{J}^2$ . For some triaxial Newtonian potentials there is an analogous to the Carter constant. An important point is that in the spherically symmetric case  $(E, \mathbf{J}_z)$  is equivalent to  $(e, r_p)$ , where  $r_p$  denotes the pericenter radial coordinate. With spin,  $(E, \mathbf{J}_z, C)$  is equivalent to  $(e, r_p, \iota)$ , where  $\iota$  denotes the inclination of the orbit with respect to the equatorial plane (the plane orthogonal to the spin). This means that the inclination plays a different role in the spherical symmetric case with respect to the axisymmetric one.

### *A possible scheme*

The first step is to obtain the steady state distribution, defined by the density profile  $\rho(r)$  and the phase space distribution function (DF)  $f(E)$ , of stars around the SMBH. This is given by the solution of the Fokker-Planck equation (or by N-body simulations). We have solutions for clusters which are spherically symmetric and which have an isotropic distribution of velocities. Here, we assume that the cluster is spherical and the SMBH spin does not change this appreciably. It is possible that the distribution of inclinations for stars with lowest  $J$  will deviate from sphericity due to close interactions with the hole, but not the cluster as a whole.

We now define  $\mathbf{J} = (J_x, J_y, J_z)$ . We note that we use specific energy  $E$  and angular momentum  $\mathbf{J}$ . An  $E > 0$  corresponds to bound orbits, so for an elliptical orbit in the field of the SMBH, the Hamiltonian of the system becomes

$$H = -\frac{1}{2}v^2 + \frac{GM_{\text{BH}}}{r} = E > 0, \quad (106)$$

and the magnitude of total angular momentum is

$$J = \frac{GM_{\text{BH}}}{\sqrt{2E}}. \quad (107)$$

Since the stars originate from a spherical cluster, all components of  $\mathbf{J}$  are allowed to diffuse independently under two-body relaxation and, as a result, orbital inclinations diffuse with  $\mathbf{J}$ . We define  $J_z \parallel \mathbf{a}_\bullet$ , where  $\mathbf{a}_\bullet$  is the spin axis of the SMBH.

Stars interact relativistically with the Kerr SMBH, this leads to deterministic changes in  $(E, \mathbf{J}_z, C)$ ; we need  $(E, \mathbf{J})$  to evolve them in the cluster. This needs to establish a correspondence between Newtonian and relativistic constants of motion (either for spinning or non-spinning black holes). With this at hand, we can then try to distinguish between changes in different components of the angular momentum,  $\Delta\mathbf{J}$ .

Then, we want to determine the region of phase space  $(E, \mathbf{J})$  from which EMRIs originate. For such calculation we need to include not only the effect of scattering on the EMRI candidate due to the other stars, but also the deterministic loss

$(\Delta E_{GW}, \Delta \mathbf{J}_{GW})$  that results from the emission of GWs at close passages to the SMBH.

We need to then estimate the changes in the constants of motion due to gravitational wave emission,  $(\Delta E^{GW}, \Delta \mathbf{J}_z^{GW}, \Delta C^{GW})$ . This means that we do not need  $\Delta C^{GW}$  for the Fokker-Planck simulations. Nevertheless, in order to work with the orbital parameters  $(p, e, \iota)$  we have to calculate  $\Delta C^{GW}$  to estimate the changes in the orbital parameters.

The idea is to study the phase space evolution of many individual EMRI candidates in a Monte Carlo fashion. One starts by sampling the stellar population according to the DF given by FP calculation. So, each EMRI candidate has an initial set of phase space coordinates such as  $(E_0, \mathbf{J}_o)$ . In principle, we should be interested in orbits which are bound to the SMBH, but one is also interested in the case when they are unbound to the hole, but bound to the cluster.

The FP solution  $\rho(r)$  and  $f(E)$  completely determines the diffusion coefficients for scattering with the cluster stars—assuming that two-body relaxation is the only dynamical mechanism. The EMRI candidate will undergo a random walk in phase space plus a determination loss of energy and angular momentum due to radiation reaction. The angular momentum jump  $\delta J_P(E, J)$ , per orbital period  $P(E)$ , is given by

$$\begin{aligned} \delta J_P(E, J) &= \langle \Delta J \rangle_t P(E) + \xi_J \left( \langle (\Delta J)^2 \rangle_t P(E) \right)^{1/2} - \Delta J_{GW}(E, J) = \\ &= \frac{J_c^2(E)}{2 J T_{\text{rlx}}(E)} P(E) + \xi_J \left( \frac{J_c^2(E)}{T_{\text{rlx}}(E)} P(E) \right)^{1/2} - \Delta J_{GW}(E, J), \end{aligned} \quad (108)$$

where  $\xi_J = \pm 1$  and the quantities inside  $\langle \cdot \rangle$  are the first and second diffusion coefficients per unit time. The second equality is obtained from simple scaling arguments. The orbital energy jump, per orbital period, is given by

$$\delta E_P(E, J) = \langle \Delta E \rangle_t P(E) + \xi_E \left( \langle (\Delta E)^2 \rangle_t P(E) \right)^{1/2} + \Delta E_{GW}(E, J), \quad (109)$$

In this equation  $D_{EE}$  and  $D_E$  are the diffusion coefficients, introduced when defining the time-dependent, orbit-averaged, isotropic, Fokker-Planck equation in energy space. For each component this is [164, 53]

$$p(E) \frac{\partial f_i}{\partial t} = - \frac{\partial F_{E,i}}{\partial E}, \quad F_{E,i} = -D_{EE,i} \frac{\partial f_i}{\partial E} - D_E f_i, \quad (110)$$

with

$$\begin{aligned}
D_{EE,i} &= 4\pi^2 G^2 m_*^2 \mu_i^2 \ln \Lambda \left( \frac{\mu_j}{\mu_i} \right)^2 \sum_j^{N_c} \left[ q(E) \int_{-\infty}^E dE' f_j(E') + \int_E^{+\infty} dE' q(E') f_j(E') \right], \\
D_{E,i} &= -4\pi^2 G^2 m_*^2 \mu_i^2 \ln \Lambda \sum_j^{N_c} \left( \frac{\mu_j}{\mu_i} \right) \int_E^{+\infty} dE' p(E') f_j(E').
\end{aligned} \tag{111}$$

The indices  $i, j$  run from 1 to the number of mass components considered,  $N_c$ , and we define  $\mu_i = m_i/m_*$ , with  $m_* = 1/N$ . One can obtain gravitational potential  $\Phi$  from Poisson's equation  $\nabla^2 \Phi(r) = 4\pi G \rho(r)$ , which needs to be updated as  $\rho(r)$  evolves over time. This can be achieved following the technique of operator-splitting by [57] and [53]. One successively updates the distribution function  $f(E)$  through the diffusion equation and the gravitation potential  $\Phi(r)$  via the Poisson equation. In each diffusion step  $\Phi(r)$  is kept constant, whilst  $f(E)$  and the diffusion coefficients are updated. Correspondingly, for every Poisson step,  $\Phi(r)$  is updated and  $f(E)$  is kept constant as a function of the adiabatic invariant.

One then needs to take into account the deterministic losses  $(\Delta E_{GW}, \Delta \mathbf{J}_{GW})$  due to GW emission that need to be added to the right hand sides of the equations. These could be obtained from the numerical calculations given some  $(E, \mathbf{J})$  and some interval of time  $\Delta t$ . In the simplest case,  $\Delta t = P(E)$ , i.e. one orbital period; but, in general, we need to have  $P(E) \ll \Delta t \ll T_{rlx}(E)$ .

This can be achieved by reading the values from the Fokker-Planck calculations to derive the new values  $(E, \mathbf{J})$ , after computing  $(\Delta E_{GW}, \Delta \mathbf{J}_{GW})_{\Delta t}$  over some  $N$  orbital periods.

Let us consider  $N_p^{orb}$  the number of radial periods, i.e. the time to go from  $r_p$  to  $r_a$  and back to  $r_p$ . This has to be distinguished from the other two periods present in generic orbits around a spinning SMBH.

Given  $N_p^{orb}$  (or alternatively  $\Delta t$ ), the relativistic Fokker-Planck integrator computes  $(\Delta E_{GW}^{GW}, \Delta \mathbf{J}_z^{GW}, \Delta C^{GW})$  and/or the new  $(p, e, \iota)$ . Again, besides the radial period,  $T_r$ , we have the polar and azimuthal periods. The first one, the polar  $T_\theta$ , is related with the fact that when we have a spinning black hole the motion, in general, is not confined in a plane, as mentioned previously.

Nevertheless, one can define an instantaneous plane of the orbit, which oscillates in a symmetric way around the equatorial plane. In that case  $T_\theta$  is the period of such oscillations. The third period, the azimuthal one  $T_\phi$ , corresponds to the time that the azimuthal angle  $\phi$  takes to run  $2\pi$ . For generic orbits the three periods are different. For a non-spinning black hole we just have  $T_r$  and  $T_\phi$  which are different because of the relativistic precession. In Newtonian dynamics these two are identical.

The algorithm could then be summarised with the following steps:

1. Obtain the initial steady state distribution of stars around the SMBH, described by  $(\rho(r), f(E))$  via a Newtonian, two-dimensional Fokker-Planck integrator. This allows us to have  $(E, \mathbf{J})$  for each star in the distribution. I.e.  $\{(E_i, \mathbf{J}_i)\}_{i=1, \dots, N_*}$ , where  $N_*$  is the number of stars. Assume  $J_z \parallel \mathbf{a}_\bullet$ . The orbital inclinations are already encoded in the angular momentum vector.
2. Establish a correspondence between  $(E, \mathbf{J})_N$  and  $(E, J_z, C)_E$  (where the subscripts  $N$  and  $E$  stand for Newtonian and Einsteinian respectively). We note that  $N_p^{orb}$  is

not the same for all stars. A solution to this is to make  $\Delta t$  equal to a fixed fraction of the (local) relaxation time. For a cusp with  $f(E) \propto E^p$ ,  $T_{\text{rlx}} \propto E^{-p}$  [139], where we expect  $p$  to range between  $\sim 0$  and  $\sim 1/2$ . The Newtonian orbital periods are  $P(E) \propto E^{-3/2}$ , so that the steps will change significantly between different particles and also during the inspiral.

3. Given the relativistic parameters, and given  $N_p^{\text{orb}}$ , we need to compute the changes due to gravitational wave emission on them,  $(\Delta E^{\text{GW}}, \Delta J_z^{\text{GW}}, \Delta C^{\text{GW}})$ . The relativistic Fokker-Planck scheme then delivers the new  $(E, J_z, C)_E$ .
4. Using the new  $(\Delta E^{\text{GW}}, \Delta J_z^{\text{GW}}, \Delta C^{\text{GW}})$  map back to obtain the new  $(E, \mathbf{J})_N$ . In this way, we compute  $\{(\Delta E_i^{\text{GW}}, \Delta \mathbf{J}_i^{\text{GW}})\}_{i=1, \dots, N_s}$ .
5. Use the results of Point (4) in the equations for  $(\delta E_P(E, J), \delta J_P(E, J))$ .
6. Iterate from point (2). Here we should pass the information of when one of the EMRIs has plunged. This is decided by the relativistic integrator. Obviously, we can derive the corresponding orbital parameters, so as to have a statistical distribution.

## Citations

## References

- [1] S.J. Aarseth, From NBODY1 to NBODY6: The Growth of an Industry. The Publications of the Astronomical Society of the Pacific **111**, 1333–1346 (1999)
- [2] S.J. Aarseth, *Gravitational N-Body Simulations* (ISBN 0521432723. Cambridge, UK: Cambridge University Press, November 2003., ???, 2003)
- [3] S.J. Aarseth, K. Zare, A regularization of the three-body problem. Celestial Mechanics **10**, 185–205 (1974). doi:10.1007/BF01227619
- [4] T. Alexander, C. Hopman, Strong mass segregation around a massive black hole. ApJ **697**, 1861–1869 (2009). doi:10.1088/0004-637X/697/2/1861
- [5] T. Alexander, M. Livio, Tidal Scattering of Stars on Supermassive Black Holes in Galactic Centers. ApJ Lett. **560**, 143–146 (2001)
- [6] P. Amaro-Seoane, Detecting intermediate-mass ratio inspirals from the ground and space. Phys. Rev. D. **98**(6), 063018 (2018a). doi:10.1103/PhysRevD.98.063018
- [7] P. Amaro-Seoane, Relativistic dynamics and extreme mass ratio inspirals. Living Reviews in Relativity **21**, 4 (2018b). doi:10.1007/s41114-018-0013-8
- [8] P. Amaro-Seoane, Relativistic dynamics and extreme mass ratio inspirals. Living Reviews in Relativity **21**, 4 (2018c). doi:10.1007/s41114-018-0013-8
- [9] P. Amaro-Seoane, M. Preto, The impact of realistic models of mass segregation on the event rate of extreme-mass ratio inspirals and cusp re-growth.



- Classical and Quantum Gravity **28**(9), 094017 (2011). doi:10.1088/0264-9381/28/9/094017
- [10] P. Amaro-Seoane, R. Spurzem, The loss-cone problem in dense nuclei. MNRAS **327**, 995–1003 (2001)
  - [11] P. Amaro-Seoane, M. Freitag, R. Spurzem, Accretion of stars on to a massive black hole: A realistic diffusion model and numerical studies. MNRAS (2004)
  - [12] P. Amaro-Seoane, M. Preto, C. Sopuerta, Notes on a relativistic Fokker-Planck integrator for EMRIs. Classical and Quantum Gravity (2010)
  - [13] P. Amaro-Seoane, C.F. Sopuerta, M.D. Freitag, The role of the supermassive black hole spin in the estimation of the EMRI event rate. MNRAS **429**, 3155–3165 (2013). doi:10.1093/mnras/sts572
  - [14] P. Amaro-Seoane, J.R. Gair, M. Freitag, M.C. Miller, I. Mandel, C.J. Cutler, S. Babak, Intermediate and extreme mass-ratio inspirals. Astrophysics, science applications and detection using LISA. Classical and Quantum Gravity **24**, 113 (2007). doi:10.1088/0264-9381/24/17/R01
  - [15] P. Amaro-Seoane, J. Barranco, A. Bernal, L. Rezzolla, Constraining scalar fields with stellar kinematics and collisional dark matter. Journal of Cosmology and Astroparticle Physics **11**, 2 (2010). doi:10.1088/1475-7516/2010/11/002
  - [16] P. Amaro-Seoane, J.R. Gair, A. Pound, S.A. Hughes, C.F. Sopuerta, Research Update on Extreme-Mass-Ratio Inspirals. Journal of Physics Conference Series **610**(1), 012002 (2015). doi:10.1088/1742-6596/610/1/012002
  - [17] P. Amaro-Seoane, H. Audley, S. Babak, J. Baker, E. Barausse, P. Bender, E. Berti, P. Binetruy, M. Born, D. Bortoluzzi, J. Camp, C. Caprini, V. Cardoso, M. Colpi, J. Conklin, N. Cornish, C. Cutler, K. Danzmann, R. Dolesi, L. Ferraioli, V. Ferroni, E. Fitzsimons, J. Gair, L. Gesa Bote, D. Giardini, F. Gibert, C. Grimaldi, H. Halloin, G. Heinzl, T. Hertog, M. Hewitson, K. Holley-Bockelmann, D. Hollington, M. Hueller, H. Inchauspe, P. Jetzer, N. Karnesis, C. Killow, A. Klein, B. Klipstein, N. Korsakova, S.L. Larson, J. Livas, I. Lloro, N. Man, D. Mance, J. Martino, I. Mateos, K. McKenzie, S.T. McWilliams, C. Miller, G. Mueller, G. Nardini, G. Nelemans, M. Nofrarias, A. Petiteau, P. Pivato, E. Plagnol, E. Porter, J. Reiche, D. Robertson, N. Robertson, E. Rossi, G. Russano, B. Schutz, A. Sesana, D. Shoemaker, J. Slutsky, C.F. Sopuerta, T. Sumner, N. Tamanini, I. Thorpe, M. Troebs, M. Vallisneri, A. Vecchio, D. Vetrugno, S. Vitale, M. Volonteri, G. Wanner, H. Ward, P. Wass, W. Weber, J. Ziemer, P. Zweifel, Laser Interferometer Space Antenna. ArXiv e-prints (2017)
  - [18] P. Amaro-Seoane, Relativistic dynamics and extreme mass ratio inspirals. Living Reviews in Relativity **21**(1), 4 (2018). doi:10.1007/s41114-018-0013-8
  - [19] P. Amaro-Seoane, Extremely large mass-ratio inspirals. Phys.Rev.D. **99**(12), 123025 (2019). doi:10.1103/PhysRevD.99.123025

- [20] M. Arca-Sedda, P. Amaro-Seoane, X. Chen, Detecting intermediate-mass black holes in Milky Way globular clusters and the Local Volume with LISA and other gravitational wave detectors. arXiv e-prints, 2007–13746 (2020)
- [21] M. Arca Sedda, A. Askar, M. Giersz, MOCCA-SURVEY Database I. Intermediate mass black holes in Milky Way globular clusters and their connection to supermassive black holes. arXiv e-prints, 1905–00902 (2019)
- [22] H. Asada, T. Futamase, Chapter 2. Post-Newtonian Approximation —Its Foundation and Applications—. *Progress of Theoretical Physics Supplement* **128**, 123–181 (1997). doi:10.1143/PTPS.128.123
- [23] S. Babak, H. Fang, J.R. Gair, K. Glampedakis, S.A. Hughes, “Kludge” gravitational waveforms for a test-body orbiting a Kerr black hole. *Ph.Rv.D* **75**(2), 024005 (2007). doi:10.1103/PhysRevD.75.024005
- [24] S. Babak, J. Gair, A. Sesana, E. Barausse, C.F. Sopuerta, C.P.L. Berry, E. Berti, P. Amaro-Seoane, A. Petiteau, A. Klein, Science with the space-based interferometer LISA. V. Extreme mass-ratio inspirals. *Phys. Rev. D* **95**(10), 103012 (2017). doi:10.1103/PhysRevD.95.103012
- [25] J.N. Bahcall, R.A. Wolf, Star distribution around a massive black hole in a globular cluster. *ApJ* **209**, 214–232 (1976)
- [26] J.N. Bahcall, R.A. Wolf, The star distribution around a massive black hole in a globular cluster. II unequal star masses. *ApJ* **216**, 883–907 (1977)
- [27] J.G. Baker, J. Centrella, D.-I. Choi, M. Koppitz, J.R. van Meter, M.C. Miller, Getting a Kick Out of Numerical Relativity. *ApJ Lett.* **653**, 93–96 (2006). doi:10.1086/510448
- [28] B. Bar-Or, T. Alexander, The statistical mechanics of relativistic orbits around a massive black hole. *Classical and Quantum Gravity* **31**(24), 244003 (2014). doi:10.1088/0264-9381/31/24/244003
- [29] B. Bar-Or, J.-B. Fouvry, Scalar Resonant Relaxation of Stars around a Massive Black Hole. *Astrophys. J. Lett.* **860**(2), 23 (2018). doi:10.3847/2041-8213/aac88e
- [30] L. Barack, C. Cutler, LISA capture sources: Approximate waveforms, signal-to-noise ratios, and parameter estimation accuracy. *Phys. Rev. D* **69**(8), 082005 (2004). doi:10.1103/PhysRevD.69.082005
- [31] L. Barack, A. Pound, Self-force and radiation reaction in general relativity. *Reports on Progress in Physics* **82**(1), 016904 (2019a). doi:10.1088/1361-6633/aae552
- [32] L. Barack, A. Pound, Self-force and radiation reaction in general relativity. *Reports on Progress in Physics* **82**, 016904 (2019b). doi:10.1088/1361-6633/aae552
- [33] E. Barausse, E. Berti, T. Hertog, S.A. Hughes, P. Jetzer, P. Pani, T.P. Sotiriou, N. Tamanini, H. Witek, K. Yagi, N. Yunes, T. Abdelsalhin, A. Achucarro, K. van Aelst, N. Afshordi, S. Akcay, L. Annulli, K.G. Arun, I. Ayuso, V. Baibhav, T. Baker, H. Bantilan, T. Barreiro, C. Barrera-Hinojosa, N. Bartolo, D. Baumann, E. Belgacem, E. Bellini, N. Bellomo, I. Ben-Dayan, I. Bena, R. Benkel, E. Bergshoeffs, L. Bernard, S. Bernuzzi, D. Bertacca, M. Besancon, F. Beutler, F. Beyer, S. Bhagwat, J. Bicak, S. Biondini, S. Bize,

D. Blas, C. Boehmer, K. Boller, B. Bonga, C. Bonvin, P. Bosso, G. Bozzola, P. Brax, M. Breitbach, R. Brito, M. Bruni, B. Brügmann, H. Bulten, A. Buonanno, L.M. Burko, C. Burrage, F. Cabral, G. Calcagni, C. Caprini, A. Cárdenas-Avendaño, M. Celoria, K. Chatziioannou, D. Chernoff, K. Clough, A. Coates, D. Comelli, G. Compère, D. Croon, D. Cruces, G. Cusin, C. Dalang, U. Danielsson, S. Das, S. Datta, J. de Boer, V. De Luca, C. De Rham, V. Desjacques, K. Destounis, F. Di Filippo, A. Dima, E. Dimastrogiovanni, S. Dolan, D. Doneva, F. Duque, R. Durrer, W. East, R. Easther, M. Elley, J.R. Ellis, R. Emparan, J.M. Ezquiaga, M. Fairbairn, S. Fairhurst, H.F. Farmer, M.R. Fasiello, V. Ferrari, P.G. Ferreira, G. Ficarra, P. Figueras, S. Fisenko, S. Foffa, N. Franchini, G. Franciolini, K. Fransen, J. Frauendiener, N. Frusciante, R. Fujita, J. Gair, A. Ganz, P. Garcia, J. Garcia-Bellido, J. Garriga, R. Geiger, C. Geng, L.Á. Gergely, C. Germani, D. Gerosa, S.B. Giddings, E. Gourgoulhon, P. Grand clement, L. Graziani, L. Gualtieri, D. Haggard, S. Haino, R. Halburd, W.-B. Han, A.J. Hawken, A. Hees, I.S. Heng, J. Hennig, C. Herdeiro, S. Hervik, J.v. Holten, C.J.D. Hoyle, Y. Hu, M. Hull, T. Ikeda, M. Isi, A. Jenkins, F. Julié, E. Kajfasz, C. Kalaghatgi, N. Kaloper, M. Kamionkowski, V. Karas, S. Kastha, Z. Keresztes, L. Kidder, T. Kimpson, A. Klein, S. Klioner, K. Kokkotas, H. Kolesova, S. Kolkowitz, J. Kopp, K. Koyama, N.V. Krishnendu, J.A.V. Kroon, M. Kunz, O. Lahav, A. Landragin, R.N. Lang, C. Le Poncin-Lafitte, J. Lemos, B. Li, S. Liberati, M. Liguori, F. Lin, G. Liu, F.S.N. Lobo, R. Loll, L. Lombriser, G. Lovelace, R.P. Macedo, E. Madge, E. Maggio, M. Maggiore, S. Marassi, P. Marcoccia, C. Markakis, W. Martens, K. Martinovic, C.J.A.P. Martins, A. Maselli, S. Mastrogiovanni, S. Matarrese, A. Matas, N.E. Mavromatos, A. Mazumdar, P.D. Meerburg, E. Megias, J. Miller, J.P. Mimoso, L. Mitnacht, M.M. Montero, B. Moore, P. Martin-Moruno, I. Musco, H. Nakano, S. Nampalliar, G. Nardini, A. Nielsen, J. Novák, N.J. Nunes, M. Okounkova, R. Oliveri, F. Oppizzi, G. Orlando, N. Oshita, G. Pappas, V. Paschalidis, H. Peiris, M. Peloso, S. Perkins, V. Pettorino, I. Pikovski, L. Pilo, J. Podolsky, A. Pontzen, S. Prabhat, G. Pratten, T. Prokopec, M. Prouza, H. Qi, A. Raccanelli, A. Rajantie, L. Randall, G. Raposo, V. Raymond, S. Renaux-Petel, A. Ricciardone, A. Riotto, T. Robson, D. Roest, R. Rollo, S. Rosofsky, J.J. Ruan, D. Rubiera-García, M. Ruiz, M. Rusu, F. Sabatie, N. Sago, M. Sakellariadou, I.D. Saltas, L. Sberna, B. Sathyaprakash, M. Scheel, P. Schmidt, B. Schutz, P. Schwaller, L. Shao, S.L. Shapiro, D. Shoemaker, A.d. Silva, C. Simpson, C.F. Sopuerta, A. Spallicci, B.A. Stefanek, L. Stein, N. Stergioulas, M. Stott, P. Sutton, R. Svarc, H. Tagoshi, T. Tahamtan, H. Takeda, T. Tanaka, G. Tantilian, G. Tassinato, O. Tattersall, S. Teukolsky, A.L. Tiec, G. Theureau, M. Trodden, A. Tolley, A. Toubiana, D. Traykova, A. Tsokaros, C. Unal, C.S. Unnikrishnan, E.C. Vagenas, P. Valageas, M. Vallisneri, J. Van den Brand, C. Van den Broeck, M. van de Meent, P. Vanhove, V. Varma, J. Veitch, B. Vercnocke, L. Verde, D. Vernieri, F. Vernizzi, R. Vicente, F. Vidotto, M. Visser, Z. Vlah, S. Vretinaris, S. Völkel, Q. Wang, Y.-T. Wang, M.C. Werner, J. Westernacher, R.v.d. Weygaert, D. Wiltshire, T. Wiseman, P. Wolf, K. Wu, K. Yamada, H.

- Yang, L. Yi, X. Yue, D. Yvon, M. Zilhão, A. Zimmerman, M. Zumalacarregui, Prospects for fundamental physics with LISA. *General Relativity and Gravitation* **52**(8), 81 (2020). doi:10.1007/s10714-020-02691-1
- [34] H. Baumgardt, P. Amaro-Seoane, R. Schödel, The distribution of stars around the Milky Way's central black hole. III. Comparison with simulations. *Astron. Astrophys.* **609**, 28 (2018). doi:10.1051/0004-6361/201730462
- [35] C.P.L. Berry, J.R. Gair, Observing the Galaxy's massive black hole with gravitational wave bursts. *Mon. Not. R. Astron. Soc.* **429**(1), 589–612 (2013). doi:10.1093/mnras/sts360
- [36] C. Berry, S. Hughes, C. Sopuerta, A. Chua, A. Heffernan, K. Holley-Bockelmann, D. Mihaylov, C. Miller, A. Sesana, The unique potential of extreme mass-ratio inspirals for gravitational-wave astronomy. *Bull. Am. Astron. Soc.* **51**(3), 42 (2019)
- [37] E. Berti, K. Yagi, H. Yang, N. Yunes, Extreme Gravity Tests with Gravitational Waves from Compact Binary Coalescences: (II) Ringdown. *Gen. Rel. Grav.* **50**(5), 49 (2018). doi:10.1007/s10714-018-2372-6
- [38] P. Bianchini, G. van de Ven, M.A. Norris, E. Schinnerer, A.L. Varri, A novel look at energy equipartition in globular clusters. *MNRAS* **458**, 3644–3654 (2016). doi:10.1093/mnras/stw552
- [39] J. Binney, S. Tremaine, *Galactic Dynamics: Second Edition* (Princeton University Press, ???, 2008)
- [40] L. Blanchet, Gravitational Radiation from Post-Newtonian Sources and Inspiralling Compact Binaries. *Living Rev. Rel.* **17**, 2 (2014). doi:10.12942/lrr-2014-2
- [41] A. Bohé, L. Shao, A. Taracchini, A. Buonanno, S. Babak, I.W. Harry, I. Hinder, S. Ossokine, M. Pürrer, V. Raymond, T. Chu, H. Fong, P. Kumar, H.P. Pfeiffer, M. Boyle, D.A. Hemberger, L.E. Kidder, G. Lovelace, M.A. Scheel, B. Szilágyi, Improved effective-one-body model of spinning, nonprecessing binary black holes for the era of gravitational-wave astrophysics with advanced detectors. *Ph. Rv. D* **95**(4), 044028 (2017). doi:10.1103/PhysRevD.95.044028
- [42] R.H. Boyer, R.W. Lindquist, Maximal Analytic Extension of the Kerr Metric. *Journal of Mathematical Physics* **8**(2), 265–281 (1967). doi:10.1063/1.1705193
- [43] W.R. Brown, M.J. Geller, S.J. Kenyon, B.C. Bromley, The Anisotropic Spatial Distribution of Hypervelocity Stars. *ApJ Lett.* **690**, 69–71 (2009). doi:10.1088/0004-637X/690/1/L69
- [44] A. Buonanno, T. Damour, Effective one-body approach to general relativistic two-body dynamics. *Ph. Rv. D* **59**(8), 084006 (1999). doi:10.1103/PhysRevD.59.084006
- [45] M. Campanelli, C.O. Lousto, P. Marronetti, Y. Zlochower, Accurate Evolutions of Orbiting Black-Hole Binaries without Excision. *Physical Review Letters* **96**(11), 111101 (2006). doi:10.1103/PhysRevLett.96.111101

- [46] B. Carr, F. Kühnel, Primordial Black Holes as Dark Matter: Recent Developments. *Annual Review of Nuclear and Particle Science* **70**(1), (2020). doi:10.1146/annurev-nucl-050520-125911
- [47] B. Carr, K. Kohri, Y. Sendouda, J. Yokoyama, Constraints on Primordial Black Holes. *arXiv e-prints*, 2002–12778 (2020)
- [48] G. Chabrier, I. Baraffe, Theory of low-mass stars and substellar objects. *ARA&A* **38**, 337–377 (2000)
- [49] G. Chabrier, I. Baraffe, J. Leconte, J. Gallardo, T. Barman, The mass-radius relationship from solar-type stars to terrestrial planets: a review, in *15th Cambridge Workshop on Cool Stars, Stellar Systems, and the Sun*, ed. by E. Stempels American Institute of Physics Conference Series, vol. 1094, 2009, pp. 102–111. doi:10.1063/1.3099078
- [50] S. Chandrasekhar, Principles of stellar dynamics. *Physical Sciences Data* (1942)
- [51] C. Charbonnel, W. Däppen, D. Schaerer, P.A. Bernasconi, A. Maeder, G. Meynet, N. Mowlavi, Grids of stellar models. VIII. from 0.4 to 1.0  $\{M_{\text{sun}}\}$  at  $z=0.020$  and  $z=0.001$ , with the mhd equation of state. *A&AS* **135**, 405–413 (1999)
- [52] X. Chen, P. Amaro-Seoane, Revealing the Formation of Stellar-mass Black Hole Binaries: The Need for Deci-Hertz Gravitational-wave Observatories. *ApJ Lett.* **842**, 2 (2017). doi:10.3847/2041-8213/aa74ce
- [53] D.F. Chernoff, M.D. Weinberg, Evolution of globular clusters in the Galaxy. *ApJ* **351**, 121–156 (1990). doi:10.1086/168451
- [54] A.J.K. Chua, J.R. Gair, Improved analytic extreme-mass-ratio inspiral model for scoping out eLISA data analysis. *Classical and Quantum Gravity* **32**(23), 232002 (2015). doi:10.1088/0264-9381/32/23/232002
- [55] A.J.K. Chua, C.J. Moore, J.R. Gair, Augmented kludge waveforms for detecting extreme-mass-ratio inspirals. *Phys. Rev. D* **96**(4), 044005 (2017). doi:10.1103/PhysRevD.96.044005
- [56] A.J.K. Chua, M.L. Katz, N. Warburton, S.A. Hughes, Rapid generation of fully relativistic extreme-mass-ratio-inspiral waveform templates for LISA data analysis. *arXiv e-prints*, 2008–06071 (2020)
- [57] H. Cohn, Late core collapse in star clusters and the gravothermal instability. *ApJ* **242**, 765–771 (1980)
- [58] C.J. Conselice, A. Wilkinson, K. Duncan, A. Mortlock, The Evolution of Galaxy Number Density at  $z \lesssim 8$  and Its Implications. *ApJ* **830**(2), 83 (2016). doi:10.3847/0004-637X/830/2/83
- [59] C. Cutler, J. Harms, Big Bang Observer and the neutron-star-binary subtraction problem. *Ph. Rev. D* **73**(4), 042001 (2006). doi:10.1103/PhysRevD.73.042001
- [60] C. Cutler, D. Kennefick, E. Poisson, Gravitational radiation reaction for bound motion around a Schwarzschild black hole. *Ph. Rev. D* **50**, 3816–3835 (1994). doi:10.1103/PhysRevD.50.3816

- [61] C. Cutler, M. Vallisneri, LISA detections of massive black hole inspirals: Parameter extraction errors due to inaccurate template waveforms. *Ph. Rv. D.* **76**(10), 104018 (2007). doi:10.1103/PhysRevD.76.104018
- [62] S. Datta, A. Gupta, S. Kastha, K.G. Arun, B.S. Sathyaprakash, Tests of general relativity using multiband observations of intermediate mass binary black hole mergers. *arXiv e-prints*, 2006–12137 (2020)
- [63] W. Dehnen, A Family of Potential-Density Pairs for Spherical Galaxies and Bulges. *MNRAS* **265**, 250 (1993)
- [64] E.N. Dorband, M. Hemsendorf, D. Merritt, Systolic and hyper-systolic algorithms for the gravitational N-body problem, with an application to Brownian motion. *Journal of Computational Physics* **185**, 484–511 (2003)
- [65] J. Ehlers, A. Rosenblum, J.N. Goldberg, P. Havas, Comments on gravitational radiation damping and energy loss in binary systems. *ApJ Lett.* **208**, 77–81 (1976). doi:10.1086/182236
- [66] E. Eilon, G. Kupi, T. Alexander, The Efficiency of Resonant Relaxation Around a Massive Black Hole. *Astrophys. J.* **698**(1), 641–647 (2009). doi:10.1088/0004-637X/698/1/641
- [67] F. Eisenhauer, G. Perrin, W. Brandner, C. Straubmeier, A. Richichi, S. Gillessen, J.P. Berger, S. Hippler, A. Eckart, M. Schöller, S. Rabien, F. Cas-saing, R. Lenzen, M. Thiel, Y. Clénet, J.R. Ramos, S. Kellner, P. Fédou, H. Baumeister, R. Hofmann, E. Gendron, A. Boehm, H. Bartko, X. Haubois, R. Klein, K. Dodds-Eden, K. Houairi, F. Hormuth, A. Gräter, L. Jocou, V. Naranjo, R. Genzel, P. Kervella, T. Henning, N. Hamaus, S. Lacour, U. Neumann, M. Haug, F. Malbet, W. Laun, J. Kolmeder, T. Paumard, R.-R. Rohloff, O. Pfuhl, K. Perraut, J. Ziegleder, D. Rouan, G. Rousset, GRAV-ITY: getting to the event horizon of Sgr A\*, in *Society of Photo-Optical Instrumentation Engineers (SPIE) Conference Series*. Society of Photo-Optical Instrumentation Engineers (SPIE) Conference Series, vol. 7013, 2008. doi:10.1117/12.788407
- [68] Event Horizon Telescope Collaboration, K. Akiyama, A. Alberdi, W. Alef, K. Asada, R. Azulay, A.-K. Baczko, D. Ball, M. Baloković, J. Barrett, D. Bintley, L. Blackburn, W. Boland, K.L. Bouman, G.C. Bower, M. Bremer, C.D. Brinkerink, R. Brissenden, S. Britzen, A.E. Broderick, D. Brogiere, T. Bronzwaer, D.-Y. Byun, J.E. Carlstrom, A. Chael, C.-k. Chan, S. Chatterjee, K. Chatterjee, M.-T. Chen, Y. Chen, I. Cho, P. Christian, J.E. Conway, J.M. Cordes, G.B. Crew, Y. Cui, J. Davelaar, M. De Laurentis, R. Deane, J. Dempsey, G. Desvignes, J. Dexter, S.S. Doeleman, R.P. Eatough, H. Falcke, V.L. Fish, E. Fomalont, R. Fraga-Encinas, W.T. Freeman, P. Friberg, C.M. Fromm, J.L. Gómez, P. Galison, C.F. Gammie, R. García, O. Gentaz, B. Georgiev, C. Goddi, R. Gold, M. Gu, M. Gurwell, K. Hada, M.H. Hecht, R. Hesper, L.C. Ho, P. Ho, M. Honma, C.-W.L. Huang, L. Huang, D.H. Hughes, S. Ikeda, M. Inoue, S. Issaoun, D.J. James, B.T. Jannuzi, M. Janssen, B. Jeter, W. Jiang, M.D. Johnson, S. Jorstad, T. Jung, M. Karami, R. Karuppusamy, T. Kawashima, G.K. Keating, M. Kettenis, J.-Y. Kim, J. Kim, J. Kim, M. Kino, J.Y. Koay, P.M. Koch, S. Koyama, M. Kramer, C. Kramer, T.P. Krich-

baum, C.-Y. Kuo, T.R. Lauer, S.-S. Lee, Y.-R. Li, Z. Li, M. Lindqvist, K. Liu, E. Liuzzo, W.-P. Lo, A.P. Lobanov, L. Loinard, C. Lonsdale, R.-S. Lu, N.R. MacDonald, J. Mao, S. Markoff, D.P. Marrone, A.P. Marscher, I. Martí-Vidal, S. Matsushita, L.D. Matthews, L. Medeiros, K.M. Menten, Y. Mizuno, I. Mizuno, J.M. Moran, K. Moriyama, M. Moscibrodzka, C. Müller, H. Nagai, N.M. Nagar, M. Nakamura, R. Narayan, G. Narayanan, I. Natarajan, R. Neri, C. Ni, A. Noutsos, H. Okino, H. Olivares, G.N. Ortiz-León, T. Oyama, F. Özel, D.C.M. Palumbo, N. Patel, U.-L. Pen, D.W. Pesce, V. Piétu, R. Plambeck, A. PopStefanija, O. Porth, B. Prather, J.A. Preciado-López, D. Psaltis, H.-Y. Pu, V. Ramakrishnan, R. Rao, M.G. Rawlings, A.W. Raymond, L. Rizzolla, B. Ripperda, F. Roelofs, A. Rogers, E. Ros, M. Rose, A. Roshanineshat, H. Rottmann, A.L. Roy, C. Ruszczyk, B.R. Ryan, K.L.J. Rygl, S. Sánchez, D. Sánchez-Arguelles, M. Sasada, T. Savolainen, F.P. Schloerb, K.-F. Schuster, L. Shao, Z. Shen, D. Small, B.W. Sohn, J. SooHoo, F. Tazaki, P. Tiede, R.P.J. Tilanus, M. Titus, K. Toma, P. Torne, T. Trent, S. Trippe, S. Tsuda, I. van Bemmell, H.J. van Langevelde, D.R. van Rossum, J. Wagner, J. Wardle, J. Weintraub, N. Wex, R. Wharton, M. Wielgus, G.N. Wong, Q. Wu, K. Young, A. Young, Z. Younsi, F. Yuan, Y.-F. Yuan, J.A. Zensus, G. Zhao, S.-S. Zhao, Z. Zhu, J.-C. Algaba, A. Allardi, R. Amestica, J. Anczarski, U. Bach, F.K. Baganoff, C. Beaudoin, B.A. Benson, R. Berthold, J.M. Blanchard, R. Blundell, S. Bustamente, R. Cappallo, E. Castillo-Domínguez, C.-C. Chang, S.-H. Chang, S.-C. Chang, C.-C. Chen, R. Chilson, T.C. Chuter, R. Córdova Rosado, I.M. Coulson, T.M. Crawford, J. Crowley, J. David, M. Derome, M. Dexter, S. Dornbusch, K.A. Dudevoir, S.A. Dzib, A. Eckart, C. Eckert, N.R. Erickson, W.B. Everett, A. Faber, J.R. Farah, V. Fath, T.W. Folkers, D.C. Forbes, R. Freund, A.I. Gómez-Ruiz, D.M. Gale, F. Gao, G. Geertsema, D.A. Graham, C.H. Greer, R. Grosslein, F. Gueth, D. Haggard, N.W. Halverson, C.-C. Han, K.-C. Han, J. Hao, Y. Hasegawa, J.W. Henning, A. Hernández-Gómez, R. Herrero-Illana, S. Heyminck, A. Hirota, J. Hoge, Y.-D. Huang, C.M.V. Impellizzeri, H. Jiang, A. Kamble, R. Keisler, K. Kimura, Y. Kono, D. Kubo, J. Kuroda, R. Lacasse, R.A. Laing, E.M. Leitch, C.-T. Li, L.C.-C. Lin, C.-T. Liu, K.-Y. Liu, L.-M. Lu, R.G. Marson, P.L. Martin-Cocher, K.D. Massingill, C. Matulonis, M.P. McColl, S.R. McWhirter, H. Messias, Z. Meyer-Zhao, D. Michalik, A. Montaña, W. Montgomerie, M. Mora-Klein, D. Muders, A. Nadolski, S. Navarro, J. Neilsen, C.H. Nguyen, H. Nishioka, T. Norton, M.A. Nowak, G. Nystrom, H. Ogawa, P. Oshiro, T. Oyama, H. Parsons, S.N. Paine, J. Peñalver, N.M. Phillips, M. Poirier, N. Pradel, R.A. Primiani, P.A. Raffin, A.S. Rahlin, G. Reiland, C. Risacher, I. Ruiz, A.F. Sáez-Madaín, R. Sassella, P. Schellart, P. Shaw, K.M. Silva, H. Shiokawa, D.R. Smith, W. Snow, K. Souccar, D. Sousa, T.K. Sridharan, R. Srinivasan, W. Stahm, A.A. Stark, K. Story, S.T. Timmer, L. Vertatschitsch, C. Walther, T.-S. Wei, N. Whitehorn, A.R. Whitney, D.P. Woody, J.G.A. Wouterloot, M. Wright, P. Yamaguchi, C.-Y. Yu, M. Zaballos, S. Zhang, L. Ziurys, First M87 Event Horizon Telescope Results. I. The Shadow of the Supermassive Black Hole. *Astrophys. J. Lett.* **875**(1), 1 (2019). doi:10.3847/2041-8213/ab0ec7

- [69] L.S. Finn, Detection, measurement, and gravitational radiation. *prd* **46**, 5236–5249 (1992). doi:10.1103/PhysRevD.46.5236
- [70] L.S. Finn, K.S. Thorne, Gravitational waves from a compact star in a circular, inspiral orbit, in the equatorial plane of a massive, spinning black hole, as observed by LISA. *Phys. Rev. D* **62**(12), 124021 (2000). doi:10.1103/PhysRevD.62.124021
- [71] J. Frank, M.J. Rees, Effects of massive central black holes on dense stellar systems. *MNRAS* **176**, 633–647 (1976). doi:10.1093/mnras/176.3.633
- [72] M. Freitag, P. Amaro-Seoane, V. Kalogera, Stellar Remnants in Galactic Nuclei: Mass Segregation. *ApJ* **649**, 91–117 (2006). doi:10.1086/506193
- [73] J.R. Gair, K. Glampedakis, Improved approximate inspirals of test bodies into Kerr black holes. *Ph. Rev. D* **73**(6), 064037 (2006). doi:10.1103/PhysRevD.73.064037
- [74] E. Gallego-Cano, R. Schödel, H. Dong, F. Nogueras-Lara, A.T. Gallego-Calvente, P. Amaro-Seoane, H. Baumgardt, The distribution of stars around the Milky Way’s central black hole. I. Deep star counts. *Astron. Astrophys.* **609**, 26 (2018). doi:10.1051/0004-6361/201730451
- [75] K. Gebhardt, R.M. Rich, L.C. Ho, A  $20000M_{\odot}$  Black Hole in the Stellar Cluster G1. *ApJ Lett.* **578**, 41–45 (2002)
- [76] R. Genzel, F. Eisenhauer, S. Gillessen, The Galactic Center massive black hole and nuclear star cluster. *Reviews of Modern Physics* **82**(4), 3121–3195 (2010). doi:10.1103/RevModPhys.82.3121
- [77] J. Gerssen, R.P. van der Marel, K. Gebhardt, P. Guhathakurta, R.C. Peterson, C. Pryor, Hubble Space Telescope Evidence for an Intermediate-Mass Black Hole in the Globular Cluster M15. II. Kinematic Analysis and Dynamical Modeling. *AJ* **124**, 3270–3288 (2002)
- [78] M. Gieles, The early evolution of the star cluster mass function. *MNRAS* **394**(4), 2113–2126 (2009). doi:10.1111/j.1365-2966.2009.14473.x
- [79] M. Giersz, Monte carlo simulations of star clusters - i. first results. *MNRAS* **298**, 1239–1248 (1998)
- [80] M. Giersz, D.C. Heggie, Statistics of n-body simulations - part one - equal masses before core collapse. *MNRAS* **268**, 257 (1994)
- [81] M. Giersz, N. Leigh, A. Hypki, N. Lützgendorf, A. Askar, MOCCA code for star cluster simulations - IV. A new scenario for intermediate mass black hole formation in globular clusters. *MNRAS* **454**(3), 3150–3165 (2015). doi:10.1093/mnras/stv2162
- [82] S. Gillessen, G. Perrin, W. Brandner, C. Straubmeier, F. Eisenhauer, S. Rabien, A. Eckart, P. Lena, R. Genzel, T. Paumard, S. Hippler, GRAVITY: the adaptive-optics-assisted two-object beam combiner instrument for the VLTI, in *Society of Photo-Optical Instrumentation Engineers (SPIE) Conference Series*. Society of Photo-Optical Instrumentation Engineers (SPIE) Conference Series, vol. 6268, 2006. doi:10.1117/12.671431
- [83] K. Glampedakis, S.A. Hughes, D. Kennefick, Approximating the inspiral of test bodies into Kerr black holes. *Phys. Rev. D* **66**(6), 064005 (2002a). doi:10.1103/PhysRevD.66.064005



- [84] K. Glampedakis, S.A. Hughes, D. Kennefick, Approximating the inspiral of test bodies into Kerr black holes. *Phys. Rev. D* **66**(6), 064005 (2002b)
- [85] K. Glampedakis, D. Kennefick, Zoom and whirl: Eccentric equatorial orbits around spinning black holes and their evolution under gravitational radiation reaction. *Phys. Rev. D* **66**(4), 044002 (2002). doi:10.1103/PhysRevD.66.044002
- [86] J.A. González, U. Sperhake, B. Brügmann, M. Hannam, S. Husa, Maximum Kick from Nonspinning Black-Hole Binary Inspiral. *Physical Review Letters* **98**(9), 091101 (2007). doi:10.1103/PhysRevLett.98.091101
- [87] Gravity Collaboration, R. Abuter, A. Amorim, M. Bauböck, J.P. Berger, H. Bonnet, W. Brandner, V. Cardoso, Y. Clénet, P.T. de Zeeuw, J. Dexter, A. Eckart, F. Eisenhauer, N.M. Förster Schreiber, P. Garcia, F. Gao, E. Gendron, R. Genzel, S. Gillessen, M. Habibi, X. Haubois, T. Henning, S. Hippler, M. Horrobin, A. Jiménez-Rosales, L. Jochum, L. Jocu, A. Kaufer, P. Kervella, S. Lacour, V. Lapeyrère, J.-B. Le Bouquin, P. Léna, M. Nowak, T. Ott, T. Paumard, K. Perraut, G. Perrin, O. Pfuhl, G. Rodríguez-Coira, J. Shanguan, S. Scheithauer, J. Stadler, O. Straub, C. Straubmeier, E. Sturm, L.J. Tacconi, F. Vincent, S. von Fellenberg, I. Waisberg, F. Widmann, E. Wiegand, E. Wozniak, J. Woillez, S. Yazici, G. Zins, Detection of the Schwarzschild precession in the orbit of the star S2 near the Galactic centre massive black hole. *Astron. Astrophys.* **636**, 5 (2020). doi:10.1051/0004-6361/202037813
- [88] J. Guillochon, E. Ramirez-Ruiz, Hydrodynamical Simulations to Determine the Feeding Rate of Black Holes by the Tidal Disruption of Stars: The Importance of the Impact Parameter and Stellar Structure. *ApJ* **767**, 25 (2013). doi:10.1088/0004-637X/767/1/25
- [89] K. Gültekin, M.C. Miller, D.P. Hamilton, Growth of Intermediate-Mass Black Holes in Globular Clusters. *ApJ* **616**, 221–230 (2004). doi:10.1086/424809
- [90] M.G. Haehnelt, Low-Frequency Gravitational Waves from Supermassive Black-Holes. *MNRAS* **269**, 199 (1994). doi:10.1093/mnras/269.1.199
- [91] O.A. Hannuksela, K.W.K. Wong, R. Brito, E. Berti, T.G.F. Li, Probing the existence of ultralight bosons with a single gravitational-wave measurement. *Nature Astron.* **3**(5), 447–451 (2019). doi:10.1038/s41550-019-0712-4
- [92] R.O. Hansen, Post-Newtonian Gravitational Radiation from Point Masses in a Hyperbolic Kepler Orbit. *Phys. Rev. D* **5**, 1021–1023 (1972). doi:10.1103/PhysRevD.5.1021
- [93] C.-J. Haster, F. Antonini, V. Kalogera, I. Mandel, N-Body Dynamics of Intermediate Mass-ratio Inspirals in Star Clusters. *ApJ* **832**, 192 (2016). doi:10.3847/0004-637X/832/2/192
- [94] C.W. Helstrom, *Statistical Theory of Signal Detection* 1968
- [95] M. Hénon, Collisional dynamics of spherical stellar systems, in *Dynamical structure and evolution of stellar systems, Lectures of the 3rd Advanced Course of the Swiss Society for Astronomy and Astrophysics (SSAA)*, ed. by L. Martinet, M. Mayor, 1973, pp. 183–260

- [96] M. Hénon, Two Recent Developments Concerning the Monte Carlo Method, in *IAU Symp. 69: Dynamics of Stellar Systems*, ed. by A. Hayli, 1975, p. 133
- [97] S. Hild, M. Abernathy, F. Acernese, P. Amaro-Seoane, et al, Sensitivity studies for third-generation gravitational wave observatories. *Classical and Quantum Gravity* **28**(9), 094013 (2011). doi:10.1088/0264-9381/28/9/094013
- [98] J.G. Hills, Hyper-velocity and tidal stars from binaries disrupted by a massive galactic black hole. *Nat* **331**, 687–689 (1988)
- [99] D. Hils, P.L. Bender, Gradual approach to coalescence for compact stars orbiting massive black holes. *ApJ Lett.* **445**, 7–10 (1995). doi:10.1086/187876
- [100] J. Hong, H.M. Lee, Black hole binaries in galactic nuclei and gravitational wave sources. *MNRAS* **448**, 754–770 (2015). doi:10.1093/mnras/stv035
- [101] C. Hopman, T. Alexander, Resonant Relaxation near a Massive Black Hole: The Stellar Distribution and Gravitational Wave Sources. *Astrophys. J.* **645**(2), 1152–1163 (2006). doi:10.1086/504400
- [102] C. Hopman, M. Freitag, S.L. Larson, Gravitational wave bursts from the Galactic massive black hole. *Mon. Not. R. Astron. Soc.* **378**(1), 129–136 (2007). doi:10.1111/j.1365-2966.2007.11758.x
- [103] S.A. Hughes, Evolution of circular, nonequatorial orbits of Kerr black holes due to gravitational-wave emission. II. Inspiral trajectories and gravitational waveforms. *Ph. Rev. D* **64**(6), 064004 (2001). doi:10.1103/PhysRevD.64.064004
- [104] J. Kepler, *Harmonices mundi libri v.* Publisher Linz (1619)
- [105] B. Kocsis, M.E. Gáspár, S. Márka, Detection Rate Estimates of Gravity Waves Emitted during Parabolic Encounters of Stellar Black Holes in Globular Clusters. *ApJ* **648**, 411–429 (2006). doi:10.1086/505641
- [106] S. Konstantinidis, P. Amaro-Seoane, K.D. Kokkotas, Investigating the retention of intermediate-mass black holes in star clusters using N-body simulations. *A&A* **557**, 135 (2013). doi:10.1051/0004-6361/201219620
- [107] J. Kormendy, L.C. Ho, Coevolution (Or Not) of Supermassive Black Holes and Host Galaxies. *ARA&A* **51**, 511–653 (2013). doi:10.1146/annurev-astro-082708-101811
- [108] J. Kormendy, The Stellar-Dynamical Search for Supermassive Black Holes in Galactic Nuclei, in *Coevolution of Black Holes and Galaxies*, ed. by L.C. Ho, 2004, p. 1
- [109] J. Kormendy, L.C. Ho, Coevolution (Or Not) of Supermassive Black Holes and Host Galaxies. *Annu. Rev. Astron. Astrophys.* **51**(1), 511–653 (2013). doi:10.1146/annurev-astro-082708-101811
- [110] A. Królak, K.D. Kokkotas, G. Schäfer, Estimation of the post-Newtonian parameters in the gravitational-wave emission of a coalescing binary. *Phys. Rev. D* **52**, 2089–2111 (1995). doi:10.1103/PhysRevD.52.2089
- [111] P. Kroupa, C. Weidner, J. Pflamm-Altenburg, I. Thies, J. Dabringhausen, M. Marks, T. Maschberger, The Stellar and Sub-Stellar Initial Mass Function of Simple and Composite Populations, ed. by T.D. Oswalt, G. Gilmore 2013, p. 115. doi:10.1007/978-94-007-5612-0\_4

- [112] P. Kroupa, On the variation of the initial mass function. *Mon. Not. R. Astron. Soc.* **322**(2), 231–246 (2001). doi:10.1046/j.1365-8711.2001.04022.x
- [113] G. Kupa, P. Amaro-Seoane, R. Spurzem, Dynamics of compact object clusters: a post-Newtonian study. *MNRAS*, **77** (2006). doi:10.1111/j.1745-3933.2006.00205.x
- [114] R.B. Larson, A method for computing the evolution of star clusters. *MNRAS* **147**, 323 (1970)
- [115] W.H. Lee, E. Ramirez-Ruiz, G. van de Ven, Short Gamma-ray Bursts from Dynamically Assembled Compact Binaries in Globular Clusters: Pathways, Rates, Hydrodynamics, and Cosmological Setting. *ApJ* **720**, 953–975 (2010). doi:10.1088/0004-637X/720/1/953
- [116] N.W.C. Leigh, N. Lützgendorf, A.M. Geller, T.J. Maccarone, C. Heinke, A. Sesana, On the coexistence of stellar-mass and intermediate-mass black holes in globular clusters. *MNRAS* **444**, 29–42 (2014). doi:10.1093/mnras/stu1437
- [117] A.P. Lightman, S.L. Shapiro, The distribution and consumption rate of stars around a massive, collapsed object. *ApJ* **211**, 244–262 (1977)
- [118] LIGO Scientific Collaboration, Virgo Collaboration, GW190521: A Binary Black Hole Merger with a Total Mass of  $150 M_{\odot}$ . *Ph. Rv. L* **125**(10), 101102 (2020a). doi:10.1103/PhysRevLett.125.101102
- [119] LIGO Scientific Collaboration, Virgo Collaboration, GWTC-2: Compact Binary Coalescences Observed by LIGO and Virgo During the First Half of the Third Observing Run. *arXiv e-prints*, 2010–14527 (2020b)
- [120] LIGO Scientific Collaboration, Virgo Collaboration, Properties and Astrophysical Implications of the  $150 M_{\odot}$  Binary Black Hole Merger GW190521. *ApJ Lett.* **900**(1), 13 (2020c). doi:10.3847/2041-8213/aba493
- [121] D.N.C. Lin, S. Tremaine, A reinvestigation of the standard model for the dynamics of a massive black hole in a globular cluster. *ApJ* **242**, 789–798 (1980). doi:10.1086/158513
- [122] L. Lindblom, B.J. Owen, D.A. Brown, Model waveform accuracy standards for gravitational wave data analysis. *Phys. Rev. D* **78**(12), 124020 (2008). doi:10.1103/PhysRevD.78.124020
- [123] C.O. Lousto, Y. Zlochower, Orbital Evolution of Extreme-Mass-Ratio Black-Hole Binaries with Numerical Relativity. *Phys. Rev. Lett.* **106**, 041101 (2011). doi:10.1103/PhysRevLett.106.041101
- [124] N. Lützgendorf, M. Kissler-Patig, N. Neumayer, H. Baumgardt, E. Noyola, P.T. de Zeeuw, K. Gebhardt, B. Jalali, A. Feldmeier, M -  $\sigma$  relation for intermediate-mass black holes in globular clusters. *A&A* **555**, 26 (2013). doi:10.1051/0004-6361/201321183
- [125] D. Lynden-Bell, A.J. Kalnajs, On the generating mechanism of spiral structure. *MNRAS* **157**, 1 (1972). doi:10.1093/mnras/157.1.1
- [126] M. MacLeod, M. Trenti, E. Ramirez-Ruiz, The Close Stellar Companions to Intermediate-mass Black Holes. *ApJ* **819**, 70 (2016). doi:10.3847/0004-637X/819/1/70

- [127] M. Maggiore, *Gravitational Waves: Volume 2: Astrophysics and Cosmology*. Gravitational Waves (Oxford University Press, ???, 2018). ISBN 9780198570899. <https://books.google.de/books?id=3ZNODwAAQBAJ>
- [128] J. Magorrian, S. Tremaine, Rates of tidal disruption of stars by massive central black holes. *MNRAS* **309**, 447–460 (1999)
- [129] K. Maguire, M. Eracleous, P.G. Jonker, M. MacLeod, S. Rosswog, Tidal Disruptions of White Dwarfs: Theoretical Models and Observational Prospects. *Space Sci. Rev.* **216**(3), 39 (2020). doi:10.1007/s11214-020-00661-2
- [130] I. Mandel, D.A. Brown, J.R. Gair, M.C. Miller, Rates and Characteristics of Intermediate Mass Ratio Inspirals Detectable by Advanced LIGO. *ApJ* **681**, 1431–1447 (2008). doi:10.1086/588246
- [131] K. Menou, Z. Haiman, B. Kocsis, Cosmological physics with black holes (and possibly white dwarfs). *New Astron. Rev.* **51**(10-12), 884–890 (2008). doi:10.1016/j.newar.2008.03.020
- [132] G. Meynet, A. Maeder, G. Schaller, D. Schaerer, C. Charbonnel, Grids of massive stars with high mass loss rates. v. from 12 to 120  $m_{\odot}$  at  $z=0.001$ , 0.004, 0.008, 0.020 and 0.040. *A&AS* **103**, 97–105 (1994)
- [133] M. Mezcua, Observational evidence for intermediate-mass black holes. *International Journal of Modern Physics D* **26**, 1730021 (2017). doi:10.1142/S021827181730021X
- [134] M.C. Miller, M. Freitag, D.P. Hamilton, V.M. Lauburg, Binary Encounters with Supermassive Black Holes: Zero-Eccentricity LISA Events. *ApJ Lett.* **631**, 117–120 (2005). doi:10.1086/497335
- [135] C.W. Misner, K.S. Thorne, J.A. Wheeler, *Gravitation* 1973
- [136] A.H. Mroue, et al., Catalog of 174 Binary Black Hole Simulations for Gravitational Wave Astronomy. *Phys. Rev. Lett.* **111**(24), 241104 (2013). doi:10.1103/PhysRevLett.111.241104
- [137] R.M. O’Leary, B. Kocsis, A. Loeb, Gravitational waves from scattering of stellar-mass black holes in galactic nuclei. *MNRAS* **395**, 2127–2146 (2009). doi:10.1111/j.1365-2966.2009.14653.x
- [138] T. Panamarev, A. Just, R. Spurzem, P. Berczik, L. Wang, M. Arca Sedda, Direct N-body simulation of the Galactic centre. *Mon. Not. R. Astron. Soc.* **484**(3), 3279–3290 (2019). doi:10.1093/mnras/stz208
- [139] P.J.E. Peebles, Star Distribution Near a Collapsed Object. *ApJ* **178**, 371–376 (1972). doi:10.1086/151797
- [140] F. Peißker, A. Eckart, M. Zajaček, B. Ali, M. Parsa, S62 and S4711: Indications of a Population of Faint Fast-moving Stars inside the S2 Orbit—S4711 on a 7.6 yr Orbit around Sgr A\*. *Astrophys. J.* **899**(1), 50 (2020). doi:10.3847/1538-4357/ab9c1c
- [141] P.C. Peters, Gravitational Radiation and the Motion of Two Point Masses. *Physical Review* **136**, 1224–1232 (1964)
- [142] P.C. Peters, J. Mathews, Gravitational Radiation from Point Masses in a Keplerian Orbit. *Physical Review* **131**, 435–440 (1963)

- [143] V. Pierro, I.M. Pinto, A.D. Spallicci, E. Laserra, F. Recano, Fast and accurate computational tools for gravitational waveforms from binary stars with any orbital eccentricity. *MNRAS* **325**, 358–372 (2001)
- [144] E. Poisson, A. Pound, I. Vega, The Motion of point particles in curved space-time. *Living Rev. Rel.* **14**, 7 (2011a). doi:10.12942/lrr-2011-7
- [145] E. Poisson, A. Pound, I. Vega, The Motion of point particles in curved space-time. *Living Rev. Rel.* **14**, 7 (2011b). doi:10.12942/lrr-2011-7
- [146] S.F. Portegies Zwart, P. Hut, J. Makino, S.L.W. McMillan, On the dissolution of evolving star clusters. *A&A* **337**, 363–371 (1998)
- [147] W.H. Press, Gravitational radiation from sources which extend into their own wave zone. *Ph.Rv.D* **15**(4), 965–968 (1977). doi:10.1103/PhysRevD.15.965
- [148] M. Preto, P. Amaro-Seoane, On Strong Mass Segregation Around a Massive Black Hole: Implications for Lower-Frequency Gravitational-Wave Astrophysics. *ApJ Lett.* **708**, 42–46 (2010). doi:10.1088/2041-8205/708/1/L42
- [149] G.D. Quinlan, S.L. Shapiro, Dynamical evolution of dense clusters of compact stars. *ApJ* **343**, 725–749 (1989). doi:10.1086/167745
- [150] K.P. Rauch, S. Tremaine, Resonant relaxation in stellar systems. *New Astronomy* **1**, 149–170 (1996a)
- [151] K.P. Rauch, S. Tremaine, Resonant relaxation in stellar systems. *New A.* **1**(2), 149–170 (1996b). doi:10.1016/S1384-1076(96)00012-7
- [152] M.J. Rees, Tidal disruption of stars by black holes of 10 to the 6th-10 to the 8th solar masses in nearby galaxies. *Nat* **333**, 523–528 (1988). doi:10.1038/333523a0
- [153] E.M. Rossi, N.C. Stone, J.A.P. Law-Smith, M. MacLeod, G. Lodato, J.L. Dai, I. Mandel, The Process of Stellar Tidal Disruption by Supermassive Black Holes. The first pericenter passage. *arXiv e-prints*, 2005–12528 (2020)
- [154] W.C. Saslaw, *Gravitational physics of stellar and galactic systems* (Cambridge, Cambridge University Press, ???, 1985)
- [155] B. Sathyaprakash, M. Abernathy, F. Acernese, P. Ajith, B. Allen, P. Amaro-Seoane, N. Andersson, S. Aoudia, K. Arun, P. Astone, et al., Scientific objectives of Einstein Telescope. *Classical and Quantum Gravity* **29**(12), 124013 (2012). doi:10.1088/0264-9381/29/12/124013
- [156] G. Schaller, D. Schaerer, G. Meynet, A. Maeder, New grids of stellar models from 0.8 to 120 solar masses at  $z = 0.020$  and  $z = 0.001$ . *A&AS* **96**, 269–331 (1992)
- [157] W. Schmidt, Celestial mechanics in Kerr spacetime. *Classical and Quantum Gravity* **19**, 2743–2764 (2002). doi:10.1088/0264-9381/19/10/314
- [158] R. Schödel, E. Gallego-Cano, H. Dong, F. Nogueras-Lara, A.T. Gallego-Calvente, P. Amaro-Seoane, H. Baumgardt, The distribution of stars around the Milky Way’s central black hole. II. Diffuse light from subgiants and dwarfs. *Astron. Astrophys.* **609**, 27 (2018). doi:10.1051/0004-6361/201730452
- [159] B.F. Schutz, REVIEW ARTICLE: Gravitational wave sources and their detectability. *Classical and Quantum Gravity* **6**(12), 1761–1780 (1989). doi:10.1088/0264-9381/6/12/006

- [160] A. Sesana, A. Vecchio, M. Eracleous, S. Sigurdsson, Observing white dwarfs orbiting massive black holes in the gravitational wave and electromagnetic window. *Mon. Not. R. Astron. Soc.* **391**(2), 718–726 (2008). doi:10.1111/j.1365-2966.2008.13904.x
- [161] A. Sesana, E. Barausse, M. Dotti, E.M. Rossi, Linking the Spin Evolution of Massive Black Holes to Galaxy Kinematics. *ApJ* **794**(2), 104 (2014). doi:10.1088/0004-637X/794/2/104
- [162] S. Sigurdsson, M.J. Rees, Capture of stellar mass compact objects by massive black holes in galactic cusps. *Mon. Not. R. Astron. Soc.* **284**(2), 318–326 (1997). doi:10.1093/mnras/284.2.318
- [163] C.F. Sopuerta, N. Yunes, New Kludge scheme for the construction of approximate waveforms for extreme-mass-ratio inspirals. *Phys. Rev. D* **84**(12), 124060 (2011). doi:10.1103/PhysRevD.84.124060
- [164] L. Spitzer, *Dynamical evolution of globular clusters* (Princeton, NJ, Princeton University Press, 1987, 191 p., ???, 1987)
- [165] L.J. Spitzer, M.H. Hart, Random gravitational encounters and the evolution of spherical systems. i. method. *ApJ* **164**, 399 (1971)
- [166] R. Spurzem, Direct  $n$ -body simulations. *Journal of Computational and Applied Mathematics* **109**, 407–432 (1999)
- [167] R. Spurzem, S.J. Aarseth, Direct collisional simulation of 100000 particles past core collapse. *MNRAS* **282**, 19 (1996)
- [168] S. Sridhar, J.R. Touma, Stellar dynamics around a massive black hole - II. Resonant relaxation. *Mon. Not. R. Astron. Soc.* **458**(4), 4143–4161 (2016). doi:10.1093/mnras/stw543
- [169] N.C. Stone, E. Vasiliev, M. Kesden, E.M. Rossi, H.B. Perets, P. Amaro-Seoane, Rates of Stellar Tidal Disruption. *Space Science Reviews* **216**(3), 35 (2020). doi:10.1007/s11214-020-00651-4
- [170] D. Syer, A. Ulmer, Tidal disruption rates of stars in observed galaxies. *MNRAS* **306**, 35–42 (1999)
- [171] K. Takahashi, S.F. Portegies Zwart, The disruption of globular star clusters in the galaxy: A comparative analysis between fokker-planck and  $n$ -body models. *ApJ Lett.* **503**, 49 (1998)
- [172] S.A. Teukolsky, The Kerr metric. *Classical and Quantum Gravity* **32**(12), 124006 (2015). doi:10.1088/0264-9381/32/12/124006
- [173] K.S. Thorne, Gravitational radiation., ed. by S.W. Hawking, W. Israel 1987, pp. 330–458
- [174] A. Torres-Orjuela, X. Chen, P. Amaro-Seoane, Phase shift of gravitational waves induced by aberration. *Ph. Rv. D* **101**(8), 083028 (2020). doi:10.1103/PhysRevD.101.083028
- [175] A. Torres-Orjuela, X. Chen, Z. Cao, P. Amaro-Seoane, P. Peng, Detecting the beaming effect of gravitational waves. *Ph. Rv. D* **100**(6), 063012 (2019). doi:10.1103/PhysRevD.100.063012
- [176] S. Tremaine, D.O. Richstone, Y. Byun, A. Dressler, S.M. Faber, C. Grillmair, J. Kormendy, T.R. Lauer, A family of models for spherical stellar systems. *AJ* **107**, 634–644 (1994)

- [177] M. Visser, The Kerr spacetime: A brief introduction. arXiv e-prints, 0706–0622 (2007)
- [178] J. Wang, D. Merritt, Revised Rates of Stellar Disruption in Galactic Nuclei. *ApJ* **600**, 149–161 (2004)
- [179] C. Wegg, O. Gerhard, M. Portail, The Initial Mass Function of the Inner Galaxy Measured from OGLE-III Microlensing Timescales. *ApJ Lett.* **843**, 5 (2017). doi:10.3847/2041-8213/aa794e
- [180] L. Wen, On the Eccentricity Distribution of Coalescing Black Hole Binaries Driven by the Kozai Mechanism in Globular Clusters. *ApJ* **598**, 419–430 (2003). doi:10.1086/378794
- [181] C.M. Will, Inaugural Article: On the unreasonable effectiveness of the post-Newtonian approximation in gravitational physics. *Proceedings of the National Academy of Science* **108**(15), 5938–5945 (2011). doi:10.1073/pnas.1103127108
- [182] C.M. Will, Incorporating post-Newtonian effects in N-body dynamics. *Ph. Rv. D* **89**(4), 044043 (2014). doi:10.1103/PhysRevD.89.044043
- [183] L. Zwick, P.R. Capelo, E. Bortolas, L. Mayer, P. Amaro-Seoane, Improved gravitational radiation time-scales: significance for LISA and LIGO-Virgo sources. arXiv e-prints, 1911–06024 (2019)